

2024-05-01

## Computational Study Of Fluorescent Molecular Probes For The Early Detection Of Alzheimer's Disease

Gabriela Elizabeth Molina Aguirre  
*University of Texas at El Paso*

Follow this and additional works at: [https://scholarworks.utep.edu/open\\_etd](https://scholarworks.utep.edu/open_etd)

 Part of the [Computational Chemistry Commons](#), and the [Physical Chemistry Commons](#)

---

### Recommended Citation

Molina Aguirre, Gabriela Elizabeth, "Computational Study Of Fluorescent Molecular Probes For The Early Detection Of Alzheimer's Disease" (2024). *Open Access Theses & Dissertations*. 4123.  
[https://scholarworks.utep.edu/open\\_etd/4123](https://scholarworks.utep.edu/open_etd/4123)

This is brought to you for free and open access by ScholarWorks@UTEP. It has been accepted for inclusion in Open Access Theses & Dissertations by an authorized administrator of ScholarWorks@UTEP. For more information, please contact [lweber@utep.edu](mailto:lweber@utep.edu).

COMPUTATIONAL STUDY OF FLUORESCENT MOLECULAR PROBES FOR THE  
EARLY DETECTION OF ALZHEIMER'S DISEASE

GABRIELA ELIZABETH MOLINA AGUIRRE

Doctoral Program in Chemistry

APPROVED:

---

Lela Vuković, Ph.D., Chair

---

Dino Villagrán, Ph.D.

---

Carlos Cabrera Martínez, Ph.D.

---

Jonathon Mohl, Ph.D.

---

Janez Košmrlj, Ph.D.

---

Balazs Pinter, Ph.D.

---

Stephen L. Crites, Jr., Ph.D.  
Dean of the Graduate School

Copyright 2024  
Gabriela Elizabeth Molina Aguirre

## **Dedication**

This work is dedicated first to my Father, God; without all his blessings and the courage he gave me, I wouldn't be where I am now.

To my son, Axel Matías, who inspires me to be better every day and to whom my heart, pure love, and entire life belong. I will always be there for you, my sweetheart, my little one, anytime you need me.

To my husband, Chris, my center, and the love of my life, thanks for constantly pushing me to run that extra mile, encouraging me to believe in myself, and loving me unconditionally. I will keep choosing you daily as my partner in this crazy adventure called life. Thanks for always taking out the best of me. I love you madly.

To my dear parents, Milton and July, for always believing in me. Thanks for all your support and love and always helping us despite the distance. Thank you for including us in your prayers every day. It has not been easy, but you always find a way to cheer me up and make me feel stronger. I love you so much!

To my dear brother, Eddy, this is to show you that even if you feel incapable of doing something, you certainly are! You can always do more than you think and better than you expect. Keep this belief close to your heart; it will help you in difficult moments. I love you so much. Don't forget that happiness is our primary purpose in life.

To my parents-in-law, Luis and Martha, for giving me the love of my life and the best husband ever. You raised him always to do his best, and I couldn't be happier to have him on my side.

Thanks for all your prayers as well.

Thanks to my brothers-in-law Jeka and Coqui and our siblings Alejo and Nico for all the happiness you share each time we talk. We love you all.

COMPUTATIONAL STUDY OF FLUORESCENT MOLECULAR PROBES FOR THE  
EARLY DETECTION OF ALZHEIMER'S DISEASE

by

GABRIELA ELIZABETH MOLINA AGUIRRE, MS.

DISSERTATION

Presented to the Faculty of the Graduate School of

The University of Texas at El Paso

in Partial Fulfillment

of the Requirements

for the Degree of

DOCTOR OF PHILOSOPHY

Department of Chemistry and Biochemistry

THE UNIVERSITY OF TEXAS AT EL PASO

May 2024

## **Acknowledgments**

I thank God for blessing me and giving me strength during difficult times.

I am very grateful to Dr. Balazs Pinter for allowing me to participate in this project and for his mentorship. Despite the distance, his encouragement has always helped me. Thanks to his family, Gabi, Maya, and Lily, for their support during tough times.

I am equally grateful to Prof. Janez Košmrlj for involving us in this project, which has been my daily motivation, and for his unwavering support.

I am very thankful to Prof. Lela Vukovic for accepting me into her group and guiding me during the final stages of my Ph.D. studies. Her support and motivation have been crucial to me.

I want to thank my committee members, Prof. Dino Villagran, Prof. Carlos Cabrera, and Prof. Jonathon Mohl, for their time, support, and guidance, which were crucial during my studies.

I am immensely thankful to Prof. Keith Pannell for his continuous support during our collaborations and while getting my internship. I would also like to thank Prof. Mahesh Narayan for always making me feel at home and for his advice and support.

I am very thankful to the Chemistry and Biochemistry Department and the graduate advisor team, Prof. Wen-Yee Lee, Prof. Skye Fortier, Ms. Veronica Fortier, and Ms. Maria Rodriguez, for their genuine interest in my family and me and their invaluable support during my graduate studies.

I also thank my lab colleagues and friends Peter, Sayantani, Anju, Payam, and Daniel for their valuable feedback and support. Special thanks to Diego, Angie, and now Jacob, our chosen family in El Paso, for making this journey more friendly with their love and support.

Lastly, I express my deepest gratitude to my Ecuador family and my beloved husband, Chris, and our son, Axel Matías. This journey would not have been possible without their understanding, unwavering support, and encouragement. I love them more than words can express.

## Abstract

Alzheimer's disease is a debilitating brain disorder that affects memory, thinking, and behavior. It is the most prevalent form of dementia and the seventh leading cause of death in the United States. As, researchers have identified biomarkers that can indicate the presence of the disease many years before the first symptoms appear, so there is an opportunity for early detection and treatment follow-ups, which could significantly improve the quality of life for those affected by this disease.

This dissertation investigates the relationship between molecular structure and optical properties of donor-bridge-acceptor (DBA) fluorescent molecular probes designed for detecting Amyloid- $\beta$  and p-Tau protein aggregates characteristic biomarkers of Alzheimer's disease from blood samples. Employing computational methods, including density functional theory (DFT) and time-dependent density functional theory (TD-DFT), we studied the behavior of excited states and absorption characteristics of these molecular probes. The first focus of our study was to understand the nature of the excited state of DBA fluorescent molecular probes using TD-DFT with implicit solvation methods. The direct correlation between experimental and calculated absorption energies validated the utility and efficacy of our computational approach in accurately capturing electronic and structural changes, and absorption properties.

The investigation was complemented by the systematic study of 138 fluorescent molecular probes to identify structure-activity relationships for absorption energies. The influence of different structural modifications was considered, including the linker (bridge), electron-withdrawing, and electron-donating group variation. Furthermore, our exploration of machine learning techniques demonstrates promising capabilities in predicting absorption energies for DBA fluorescent probes.

In summary, this dissertation contributes to advancing molecular design strategies for Alzheimer's disease detection by uncovering fundamental principles governing the optical properties of fluorescent probes. The integration of computational methodologies with experimental insights provided valuable guidance for the rational design of these molecular probes. The application of machine learning techniques shows promise in accelerating the screening and optimization of fluorescent probes, advancing efforts toward the early diagnosis and treatment of Alzheimer's disease.



## Table of Contents

Dedication .....	iii
Acknowledgments.....	v
Abstract .....	vi
Table of Contents .....	viii
List of Tables .....	x
List of Figures .....	xi
Chapter 1: Introduction .....	1
1.1 Alzheimer’s Disease (AD).....	1
1.1.1 History of AD .....	1
1.1.2 Clinical Stages .....	2
1.1.3 Common Symptomatology .....	3
1.2 Brain Alterations in AD .....	4
1.3 Current Detection Techniques, Challenges, and New Horizons.....	5
1.3.1 In-vivo techniques.....	6
1.3.1.1 Positron Emission Tomography (PET).....	6
1.3.1.2 Single-Photon Emission Computed Tomography Imaging (SPECT).....	7
1.3.1.3 Structural Magnetic Resonance Imaging (MRI).....	7
1.3.2 Ex-vivo techniques.....	8
1.3.4 Current challenges and new horizons .....	9
1.3 Photochemistry in Organic Compounds .....	10
1.4 Molecular Probes for AD Detection .....	13
1.4.1 Development of molecular probes .....	13
1.4.2 Properties and criteria of molecular probes for AD detection .....	15
1.4.3 Relevant studies – DBA molecular probes .....	16
1.5 Research Objectives and Hypothesis .....	18
1.6 Chapters Description and Study Approach.....	20
Chapter 2: Methodology .....	22
2.1 Schrödinger Equation.....	22

2.2	Density Functional Theory (DFT) .....	25
2.3	Time-Dependent Density Functional Theory (TD-DFT) .....	28
2.4	General Methodology Applied in the Studies and Input Examples.....	29
Chapter 3: Versatile CN-Substituted Benzene, Pyridine, and Pyrimidine-Based Fluorescent Probes for Amyloid- $\beta$ Detection: A Structure-Spectroscopic-Activity Relationship Study .....		
		41
3.1	Introduction.....	41
3.2	Methodology .....	44
3.3	Results and Discussion .....	45
3.4	Conclusions.....	62
Chapter 4: Photophysics of molecular probes for Amyloid- $\beta$ detection: computational insights into roles of probe linker and functional groups .....		
		63
4.1	Introduction.....	63
4.2	Computational Methods.....	66
4.2.1	Quantum Calculations.....	66
4.2.2	Machine Learning Models .....	68
4.3	Results and Discussion .....	69
4.3.1	Studied Structures and Validation of the Computational Protocol.....	69
4.3.2	Nature of the S <sub>1</sub> State .....	77
4.3.3	Effect of donor, acceptor, and linker groups on the absorption energies .....	82
4.3.4	Pyridine, pyrimidine, and pyranone derivatives as acceptors.....	84
4.4	Conclusions.....	92
Chapter 5: Conclusion and Recommendations for future work.....		
		95
5.1	Conclusions.....	95
5.2	Recommendations for Future Work.....	97
References.....		99

## List of Tables

Table 3.1: Structural building blocks of pyridinyl- and pyrimidinyl-bearing push-pull molecules. The resemblance of geometry and size with previously reported biphenyl and tolan FDDNP-analogues FDDBP and FDDTP, respectively, promises favorable spectroscopic and binding properties of the analogues. ....	44
Table 3.2: Functional group-condensed charges in the ground ( $S_0$ ) and excited ( $S_1$ ) states obtained for <b>DDNP</b> , <b>1Ab</b> , <b>2Cd</b> , and <b>2Cg</b> using Mulliken analysis.....	54
Table 3.3: Dipole moments in the ground and excited state (Debye) B3LYP/cc-PVTZ level of theory .....	57
Table 4.1: Calculated and experimental values of absorption energies (eV) shown in the correlations of Figure 4.5. DCM, hexane, MeCN, and MeOH were used as solvents at the M062X/cc-PVTZ level of theory.....	72
Table 4.2: RMSD and MAE for the computational predictions in all solvents (eV).....	75

## List of Figures

Figure 1.1: Jablonski diagram. VR: vertical relaxation, IC: internal conversion, ISC: intersystem crossing, n.r.: non-radiative decay, $k_f$ : fluorescence rate constant, $k_p$ : phosphorescence rate constant, abs: absorption.....	12
Figure 1.2: Structures of several widely used molecular probes for the detection of AD, a) charged molecules, b) neutral molecules, and c) near infrared molecular probes (NIRF) .....	14
Figure 1.3: Schematic illustration of the working principle of DBA molecular probes, designed to emit a fluorescent signal when binding to biomarkers and not emit signals when dissolved in the aqueous solution.....	15
Figure 1.4: In vitro fluorescence microscopy using Alzheimer's disease brain tissue and inspected and synthesized molecular probes <b>1a</b> , <b>1e</b> , <b>1f</b> , and <b>1g</b> . Reprinted (adapted) with permission from J. Med. Chem. 2017, 60, 21, 8741–8757. Copyright 2017 American Chemical Society.....	17
Figure 2.1: Jacob's ladder of functionals employed in DFT .....	26
Figure 3.1: Chemical structures of Thioflavin T ( <b>ThT</b> ), 1,1-dicyano-2-[6-(dimethylamino)naphthalen-2-yl]propene ( <b>DDNP</b> ), its fluorinated derivative <b>FDDNP</b> , biphenyl analogue <b>FDDBP</b> and tolan (diphenylacetylene) analogue <b>FDDTP</b> . .....	43
Figure 3.2: Equilibrium structures of the ground ( $S_0$ ) and excited state ( $S_1$ ) species of the molecular probes <b>DDNP</b> – <b>1Ah</b> considered in this study.....	47
Figure 3.3: Equilibrium structures of the ground ( $S_0$ ) and excited state ( $S_1$ ) species of the molecular probes <b>1Bc</b> – <b>1Ce</b> considered in this study.....	48
Figure 3.4: Equilibrium structures of the ground ( $S_0$ ) and excited state ( $S_1$ ) species of the molecular probes <b>2Ca</b> – <b>2Ch</b> considered in this study.....	49
Figure 3.5: Equilibrium structures of the ground ( $S_0$ ) and excited state ( $S_1$ ) species of <b>DDNP</b> , <b>1Ab</b> , <b>2Cd</b> , and <b>2Cg</b> .....	50
Figure 3.6: Dependency of the relative energy with the dihedral angle of <b>1Ab</b> calculated in the gas phase. ....	51
Figure 3.7: Frontier HOMO and LUMO orbitals for DDNP, 1Ab, 2Cd and 2Cg. The computed weight of the HOMO $\rightarrow$ LUMO transition to the $S_0 \rightarrow S_1$ vertical excitation upon photon absorption is provided. Orbital composition analysis based on the Mulliken partition. D: donor (EDG), B: bridge (HC linker), A: acceptor (EWG) group. ....	52
Figure 3.8: Electron density difference change ( $\Delta\delta$ ) for the $S_0 \rightarrow S_1$ transition of <b>DDNP</b> , <b>1Ab</b> , <b>2Cd</b> , and <b>2Cg</b> .....	53
Figure 3.9: The dependency of the oscillator strength with the dihedral angle for molecular probes <b>1Ab</b> , <b>2Cc</b> , and <b>FDDNP</b> calculated in DCM. ....	55
Figure 3.10: Schematic representation of the environment-dependent fluorescence in the excited state. D: donor (EDG), B: bridge (HC linker), A: acceptor (EWG) group.....	56
Figure 3.11: Change on the dipole moment when going for the ground ( $S_0$ ) to the excited state ( $S_1$ ) .....	56
Figure 3.12: Linear correlation between computed and experimental absorption energies in dichloromethane (DCM) (eV).....	60
Figure 3.13: Linear correlation between computed and experimental absorption energies in methanol (MeOH) (eV).....	61
Figure 3.14: Linear correlation between computed and experimental absorption energies in acetonitrile (MeCN) (eV).....	61

Figure 3.15: Linear correlation between computed and experimental absorption energies in Hexane (eV).....	62
Figure 4.1: a) Schematic representation of DBA fluorophores, b) First generation of molecular probes that detected Amyloid $\beta$ plaques and p-Tau tangles, c) Example of families, additional structural modifications, pyranone derivatives and their functionalization considered in this study .....	65
Figure 4.2: a) Definition of the six principal families ( <b>1-6</b> ) of the studied molecular probes given together with the selection of acceptor (A) and donor (D) sets for systematic computational study, b) additional structural modifications studies, and c) pyranone derivatives and their functionalization studied at the acceptor site .....	70
Figure 4.3: Calculated and X-ray structural information of molecules <b>4iiif</b> and <b>6iia</b> .....	71
Figure 4.4: Structures of the molecular probes considered in Table 4.1 .....	73
Figure 4.5: Correlation between computed and experimental absorption energies in a) dichloromethane (DCM), b) hexane, c) acetonitrile (MeCN), and d) methanol (MeOH) calculated at M062X/cc-PVTZ level of theory, involved molecular probes specified in Table S2. ....	74
Figure 4.6: Calculated and corrected values of absorption energy. Mean absolute error (MAE) and mean squared root deviation (RMSD) are presented in each case.....	75
Figure 4.7: Correlation between corrected computed and experimental absorption energies (nm) in dichloromethane (DCM). Calculated at M062X/cc-PVTZ level of theory .....	76
Figure 4.8: Equilibrium structures of the ground ( $S_0$ ) and excited states ( $S_1$ ) for the parent species of families <b>1-6</b> . ....	78
Figure 4.9: HOMO – LUMO orbitals for the parent molecules of families <b>1-6</b> . The computed weight of the HOMO – LUMO transition to the $S_0 \rightarrow S_1$ vertical excitation is provided. Orbital composition analysis based on Mulliken partition (D: donor, B: bridge, A: acceptor) .....	79
Figure 4.10: Electron density difference distributions ( $\Delta\rho$ ) for the $S_0 \rightarrow S_1$ transition of the parent molecules of families <b>1-6</b> .....	80
Figure 4.11: Heat maps demonstrating the influence of donor, acceptor, and linker groups on absorption energies (reported in eV).....	83
Figure 4.12: Impact of additional structural modifications on absorption energies. ....	85
Figure 4.13: Impact of pyranone derivatives and their functionalization at the acceptor site on absorption energies .....	88
Figure 4.14: a) Correlation between predicted and calculated absorption energies, where the predicted energies were obtained from the SVM model with RBF kernel that had the best value of $r^2$ , b) Box plots showing a distribution of the $r^2$ values for 200 distinct machine learning models trained with RBF and linear SVM kernel models. The median values of the $r^2$ distribution are noted in each case. ....	90
Figure 4.15: Dependency of trained ML models quality on molecular fingerprint type. Box plots showing distributions of the $r^2$ values for the 200 machine learning models, each trained with RBF and linear kernels using five different fingerprints from RDKit. The median values of the $r^2$ distributions are noted in each case. ....	91

## **Chapter 1: Introduction**

This chapter contains an overview of Alzheimer's disease, including its history, clinical stages, specific biomarkers, current detection techniques, challenges, and emerging perspectives. Additionally, the nature and characteristics of the excited state of organic molecular probes are described to explain the mechanism behind their behavior. This information will serve as the basis for introducing the main research topic, justifying the work carried out, and outlining the main objectives of the study.

### **1.1 ALZHEIMER'S DISEASE (AD)**

Alzheimer's disease is a progressive brain disorder that affects memory, thinking, and behavior. It is recognized as the most common type of dementia, accounting for 60–70% of cases<sup>1</sup>, and the seventh leading cause of death in the United States<sup>2</sup>, which is characterized by a decline in cognitive abilities that can interfere with daily life.<sup>2</sup> According to Alzheimer's Disease International (ADI), there are 10 million new cases of dementia each year worldwide. The number of people suffering from this disease will reach 139 million by 2050, and the cost will increase to around \$2.8 trillion by 2030, being one of the most costly illnesses for society<sup>3</sup>. While Alzheimer's disease is commonly associated with the elderly population, affecting around 10% of people over the age of 65 and 50% of those over 85, it is essential to mention that it can also affect younger adults. Indeed, inherited Alzheimer's disease (DIAD) has been reported in young people in their early twenties.<sup>1,4</sup>

#### **1.1.1 History of AD**

In 1906, the German clinical psychiatrist and neuropathologist Dr. Alois Alzheimer was interested in the symptomatology and progression of the illness of Auguste Deter, who suffered a

peculiar disease process of the cerebral cortex. The 50-year-old woman presented progressive memory and language impairment, disorientation, and paranoid symptomatology, including sleep disorders, aggressiveness, memory loss, confusion, and drastic changes in her mood, which increased in intensity and progression. After the autopsy, morphological and histological studies revealed some alterations, later known as neuritic plaques and neurofibrillary tangles. Alzheimer identified four other cases of this illness between 1909 and 1911 that, after a reexamination in 1998, showed to be the same process but in a different stage.<sup>5</sup> After some years, this disease was named Alzheimer's disease (AD) in honor of his efforts and pioneering role played. Remarkably, many of the clinical observations and pathological findings that Alzheimer described more than a century ago continue to remain central to our understanding of the disease today.<sup>6</sup>

### **1.1.2 Clinical Stages**

It is commonly recognized that AD progresses through three stages: mild (early), moderate, and severe<sup>1,4,7</sup>. Each stage is described below.

The mild stage affects recent episodic memories, but memories from the distant past are usually less affected or not affected at all. There is a slow decline in the capacity to identify visual and spatial relationships among objects, better known as visuospatial skills, and the disruption of the ability to manage thoughts, emotions, and actions begins in the predementia stages.<sup>1</sup> Patients in this stage can live autonomously, work, and be active in society. Still, they need more time to finish daily tasks, especially when handling finances, which could be challenging.<sup>4,7</sup> However, relatives or close people may notice increasing problems with speech, memory, misplacing or losing objects, planning, and organizing.<sup>8</sup> In this stage, symptoms like anxiety, irritability, and depression can be present. Neurological examination is generally normal during this phase.<sup>1</sup>

The moderate stage is known to be the most extended phase; sometimes, it can last for years. During this stage, patients have difficulty with episodic memory, which involves personal experiences occurring in daily life, such as time, place, and detailed information of an event<sup>9</sup>, but may still retain critical details about their life. Patients could face changes in sleep patterns, may not recall their address or phone number, and often need clarification about the date and their surroundings. At this stage, all cognitive functions are affected, and patients will begin to have problems recognizing loved ones, learning new things, and usually require more care.<sup>1,4,7</sup> Caregivers usually help them with personal daily activities such as dressing, bathing, and meal preparation.<sup>1,4</sup> Other people can notice symptoms like mood and behavioral changes, particularly in challenging situations.<sup>10</sup>

In the late stage of Alzheimer's disease, also known as the severe stage, all the symptoms mentioned above worsen considerably. Patients in this stage often require extensive assistance with their care during their daily activities. They cannot manage their movement, walking, sitting, and talking.<sup>1,7</sup> This phase of the disease is accompanied by multiple complications such as immobility, malnutrition, and thrombosis.<sup>1</sup> Additionally, it is common for patients in this stage to develop lung infections, named aspiration pneumonia, caused by the food entering the trachea instead of the esophagus because of their difficulty eating.<sup>4</sup> All the complications mentioned above can be life-threatening, making this period even more challenging for both the patients and their loved ones.<sup>1</sup>

### **1.1.3 Common Symptomatology**

Unfortunately, Alzheimer's disease presents late symptomatology after the brain has already been significantly damaged. The damage caused is irreversible, making early detection and intervention crucial for the improvement of the lives of these patients.<sup>6</sup>



The initial indicators of Alzheimer's can differ from one person to another. Commonly, memory problems<sup>11</sup> are the first indicators of cognitive decline related to AD. Some people who experience memory loss may have mild cognitive impairment (MCI), which is associated with the mild stage of AD. These patients may experience more memory loss than is typical for their age, but their symptoms do not significantly interfere with their everyday lives.<sup>7</sup>

A decline in cognition, including word-finding, vision/spatial relationship, and decreased reasoning, could indicate the early stages of the disease, and some studies also link movement difficulties and issues with the sense of smell with it. Although older people with MCI are at a greater risk of developing AD, not all of them do.<sup>7</sup>

## **1.2 BRAIN ALTERATIONS IN AD**

Neurons are connected nerve cells in the brain responsible for transmitting information throughout the body through chemical or electrical signals. Adult people have billions of neurons, and trillions of synapses are contained in the dendrites where the neurons communicate with each other. Synapses are vital in memory, sensations, thoughts, movements, and skills. AD is associated with several brain changes, including the accumulation of Amyloid  $\beta$  ( $A\beta$ ) fragments into aggregates outside the neurons and the spread of an abnormal form of tau called hyperphosphorylated tau protein (p-tau) that forms tangles (NFT) inside neurons.<sup>12</sup> These changes are characteristic of AD and commonly followed by neurodegeneration.  $A\beta$  aggregates may interfere in the communication between neurons at synapses, while p-Tau tangles can impede the transportation of essential nutrients needed for proper neural functioning. Interestingly,  $A\beta$  accumulation is hypothesized to begin before p-Tau, and an increase in NFTs could lead to an increase in  $A\beta$  aggregates.<sup>4</sup>

AD is also linked with inflammation and atrophy, related to decreased brain volume. Microglia, the immune system cells in the brain, attempt to clear toxic beta-amyloid and tau proteins, along with debris from dead and dying cells. However, chronic inflammation may occur when microglia fail to keep up with the excessive workload. Conversely, atrophy occurs due to cell loss, which further compromises normal brain function. Consequently, the ability of the brain to metabolize glucose, its primary fuel, decreases, leading to further dysfunction.<sup>4,12</sup>

### **1.3 CURRENT DETECTION TECHNIQUES, CHALLENGES, AND NEW HORIZONS**

Detecting Alzheimer's disease is crucial for improving the quality of life of people who face it and their families. This section will examine the current detection techniques for Alzheimer's disease, challenges, and new frontiers being explored to improve early diagnosis of this disease.

The most reliable way to diagnose AD is through a pathological evaluation of post-mortem autopsies where it is analyzed the presence and distribution of Ab and NFT in the brain.<sup>6</sup> In a clinical setting, several tools and techniques aid in diagnosing AD. The diagnosis of AD includes information about the patient's medical history, neuropsychological evaluations that include memory, problem-solving, and depression tests, as well as the exclusion of other possible diseases using laboratory work and supplementary tests. In-vivo and ex-vivo techniques are also used to complement the diagnosis, helping to identify patterns in the brain. Results are analyzed together, and it takes a long time to emit a diagnosis, so exams may need to be carried out over time to evaluate changes in the brain.<sup>1,6,7</sup>

### 1.3.1 In-vivo techniques

The most common imaging techniques used in-vivo to diagnose Alzheimer's disease include positron emission tomography (PET), single-photon emission computed tomography imaging (SPECT), and structural magnetic resonance imaging (MRI).<sup>12,13</sup>

#### 1.3.1.1 Positron Emission Tomography (PET)

Positron emission tomography (PET) is a nuclear imaging technique that measures brain metabolism using <sup>18</sup>F-fluorodeoxyglucose (FDG-PET).<sup>6,13</sup> Research has shown that hypometabolism, a decrease in the glucose metabolic activity of the brain cells in the posterior cingulate cortex and precuneus, is the earliest detectable sign of the disease and can also be detected at the mild stage.<sup>12,14,15</sup> In AD, the impaired neuronal activity leads to FDG uptake. Changes in FDG uptake could be attributed to pharmacological effects and may also reflect disease progression, especially when measured during follow-up visits for several months.<sup>12</sup>

In recent years, there have been significant developments in the use of *in vivo* PET-based amyloid imaging techniques, which use a radioactive substrate that binds to amyloid plaques in the brain. PET-based amyloid imaging detects one of the hallmark molecular lesions of AD.<sup>6</sup> However, there are practical concerns about its use in the clinical setting since a negative amyloid scan can exclude that a patient's cognitive impairment is due to AD, but a positive result is less informative because it can be related to cognitively normal older adults and people with other non-AD neurological conditions.<sup>16</sup>

PET probes destroy electrons through the emission of positrons, which produce the emission of two  $\gamma$ -photons in opposite directions detected by the PET scanner to provide high-resolution images.

### ***1.3.1.2 Single-Photon Emission Computed Tomography Imaging (SPECT)***

A single-photon emission computed tomography (SPECT) scan is a nuclear medicine technique to evaluate brain perfusion.<sup>17</sup> This technique measures the quantity of blood taken up in some brain regions by directly measuring  $\gamma$ -radiation using radiopharmaceuticals. SPECT is less expensive than PET because it utilizes longer-lived radioisotopes such as  $^{99m}\text{Tc}$ , which has a lifetime of 6 hours, or  $^{123}\text{I}$ , with an average lifetime of 13 hours.<sup>13</sup>

Two of the most used highly lipophilic radiotracers are  $^{99m}\text{Tc}$ -ECD (ethylcysteinate-dimer) and  $^{99m}\text{Tc}$ -HMPAO (hexamethyl propylene amine oxime). These tracers have gained popularity due to their logistical advantages and their ability to cross the blood-brain barrier (BBB) easily.<sup>17</sup>

To perform SPECT scans, a radiotracer is injected into the bloodstream of the patient, and the scan is performed sometime later. For example, after injection, tomographic images are acquired after 45-60 minutes for ECD and 60-90 minutes for HMPAO.<sup>17</sup> Besides these advantages, SPECT scans are not perfect as they have lower resolution when compared to PET scans.<sup>13</sup>

### ***1.3.1.3 Structural Magnetic Resonance Imaging (MRI)***

Magnetic resonance imaging (MRI) is a diagnostic tool that provides information on the regional distribution of changes in a macroscopic process.<sup>12</sup> MRI is a form of nuclear magnetic resonance (NMR) that works by exciting hydrogen protons ( $^1\text{H}$ ) found in water in the body with a normal frequency (40 – 130 MHz) and analyzes the relaxation pattern of these atoms when returning to the ground state after excitation. This process is known as free-induction decay (FID). FID is related to the position of water in the body, which will vary depending on the chemical environment, resulting in different relaxation patterns. The FID signal is transformed into a

magnetic resonance image using Fourier transformation, and the intensity depends on the proton density of the tissue being imaged.

MRI contrast also depends on tissue-specific parameters like longitudinal relaxation time ( $T_1$ ) and transverse relaxation time ( $T_2$ ), which measure the time that the magnetic moment of the displaced nuclei takes to return to equilibrium and the decay time for the FID response, respectively.<sup>13</sup> The most frequently used MRI measure is the hippocampus volume, which is evidenced in some regions of the brain that have reduced in size (also known as shrunk or atrophy), which is carried out through visual inspection or manual drawing on MRI slices.<sup>12</sup>

Repeated scans can be used to track those changes in function of time. While the shrinkage could give some insights into Alzheimer's disease or another form of neurodegenerative dementia, it cannot provide a definitive diagnosis on its own.

### **1.3.2 Ex-vivo techniques**

Ex-vivo techniques use fluid biomarkers and include cerebrospinal fluid (CSF), a filtered plasma-derived liquid contained in the ventricles of the brain, spine, and subarachnoid spaces in the cranium.<sup>18</sup> CSF is considered invasive since it is obtained through a lumbar puncture between the third and fourth lumbar vertebrae.<sup>18,19</sup> This technique is used to analyze levels of various proteins, including 42 amino acid-long amyloid-beta peptide ( $A\beta$ -42), tau phosphorylated at threonine (p-tau181), and total tau protein (t-tau).<sup>20</sup>

AD patients show decreased levels of  $A\beta$ -42 peptide due to amyloid deposition in the brain and elevated levels of phosphorylated tau (p-tau). Some studies showed that the baseline  $A\beta$ 1-42/p-tau or t-tau/ $A\beta$ 1-42 ratios is better than the p-tau or t-tau alone and could accurately predict the progression from mild cognitive impairment (MCI) to AD.<sup>6,20</sup>

The CSF analysis has been accepted as a suitable procedure for diagnosing AD by the National Institute of Neurological and Communicative Disorders and Stroke and the Alzheimer's Disease and Related Disorders Association (NINCDS–ADRDA).<sup>1</sup>

#### **1.3.4 Current challenges and new horizons**

The current techniques for AD diagnosis are only available for some populations. MRI and PET scans are expensive and may have limited availability in remote areas. On the other hand, CSF analysis is a more accurate method, but the extraction is invasive to the patient, so it can be both uncomfortable and risky.<sup>3</sup> Scientists have been working on enhancing traditional diagnostic techniques through the exploration of other low-cost, specific, easily accessible, and non-invasive methods for the detection of AD. In this regard, blood tests have been a significant focus of attention.<sup>3</sup>

Plasma biomarkers were proposed for the first time as potential substitutes for CSF biomarkers in the early detection of Alzheimer's disease in 2007.<sup>6</sup> Since then, many studies have been carried out to improve the sensitivity of molecular probes employed to detect these biomarkers. When comparing the costs of the different techniques, performing a tomography, such as an A $\beta$ -PET scan, will be about eight times more expensive than having a CSF analysis. At the same time, blood samples could be as much as sixteen times cheaper than a PET scan.<sup>21</sup>

Furthermore, some studies have revealed that changes associated with AD begin to accumulate between 20 to 30 years before clinical symptoms become evident, which means irreversible damage has been caused in the brain.<sup>22,23</sup> This highlights the importance of early detection since there is currently no cure for AD.

Early detection can change the lives of millions of patients and their families and has several significant benefits. First, it can help better monitor the treatment effectiveness, ensuring

the best care possible for patients who receive it. Additionally, it can help to better identify individuals with the condition necessary for the study so clinical trials can be conducted with a more targeted approach, deriving more relevant results. Furthermore, it could enable the immediate application of treatments and therapies to delay the progression of cognitive decline, ultimately improving the life quality of the patients and their families.<sup>4</sup>

### 1.3 PHOTOCHEMISTRY IN ORGANIC COMPOUNDS

Electromagnetic radiation consists of electromagnetic waves in the form of electric and magnetic fields oscillating perpendicular to each other and also to the direction of propagation. Some examples of such waves include radio waves, microwaves, infrared, visible, better known as light, ultraviolet, X-rays, and gamma rays. When a photon interacts with a molecule, there is a chance, depending on the energy of the photon and the orientation of the molecules, among other factors, that the photon is absorbed by the molecule with which its energy is transferred to (or taken up by) the molecule. During this process, called absorption, the quantum state of the molecule changes. Within the Born-Oppenheimer approximation, the nature of the quantum state that changes can be characterized as electronic (UV-Vis), vibrational (IR), rotational (Microwave), electron spin (Microwave), and nuclear spin (Radio). Absorption of a photon in the UV-Vis region with energy matching the energy difference between two quantum states of the molecule can trigger an electronic transition in the molecule within a time scale of approximately  $10^{-15}$  seconds. In this process, it can be assumed that the nuclei remain fixed, so the major change occurs in the electronic structure which is often described as the promotion of an electron from a high energy occupied molecular orbital to a low energy vacant molecular orbital.

Figure 1.1 summarizes the key stages of the photochemistry of an organic molecule that absorbs a photon in the UV-Vis regime using a Jablonski Diagram.<sup>24</sup> The electronic structure of excited states adopted after absorption of light can be qualitatively described by molecular orbitals (MO). These MOs typically reflect the change in the valence electronic structure of the molecule, while inner-shell electrons are assumed to remain unaltered. The electronic ground state, termed  $S_0$ , is typically singlet since stable organic molecules have an even number of electrons that fill up the lowest energy molecular orbitals with two electrons according to Hund's rule, while high energy antibonding orbitals in the valence shell remain unoccupied.

Upon absorption of a photon, an electron is transferred from one of the valence MOs, often from the highest occupied molecular orbital (HOMO), to either the lowest unoccupied molecular orbital (LUMO) or an unoccupied orbital with higher energy. This excitation leads to two unpaired electrons in different MOs and thus can adopt either a singlet (S) or triplet (T) configuration. For example, after the electronic transition with the lowest energy difference (very often dominated by the HOMO to LUMO transition), the molecule will adopt either the first singlet ( $S_1$ ) or, after the intersystem crossing, the first triplet excited state ( $T_1$ ).

Different deactivation paths can be followed upon absorption of energy.<sup>24</sup> The  $S_1$  state can decay directly to  $S_0$ , in a spin-allowed transition, by the emission of a photon, a process called fluorescence. The excitation does not necessarily take place to the lowest singlet state,  $S_1$ . With higher energy photons, higher-lying singlet states, such as  $S_2$ ,  $S_3$ ,  $S_4$ , ..., commonly denoted as  $S_n$ , can be reached. According to Kasha's rule, regardless of which singlet excited state is initially adopted ( $S_n$ ), the fluorescence observed will correspond to the one from the lowest excited singlet state ( $S_1$ ) in its lowest vibrational energy. Most of the time,  $S_n$  returns to  $S_1$  through a very rapid non-radiative decay called internal conversion (IC). Hence, the possibility of fluorescence from a



$S_n$  is very low; if it happens, the emission will be less efficient and less intense. Non-radiative decay, through which the energy of the photon is transferred to the environment and dissipated via molecular vibration and rotations, could also occur from  $S_n$  to  $S_0$ , resulting in competition with fluorescence. Molecules with a smaller HOMO-LUMO gap tend to have a faster non-radiative decay deactivation process.

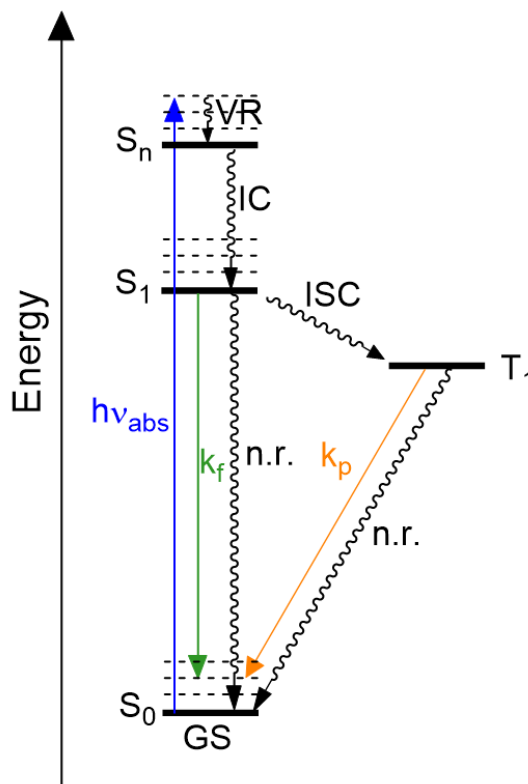


Figure 1.1: Jablonski diagram. VR: vertical relaxation, IC: internal conversion, ISC: intersystem crossing, n.r.: non-radiative decay,  $k_f$ : fluorescence rate constant,  $k_p$ : phosphorescence rate constant, abs: absorption

When non-radiative decay involves a change in multiplicity, i.e., transitions from S to T states or vice versa, the process is called intersystem crossing (ISC), which is forbidden by spin conservation rules and requires spin-orbit coupling to maintain total angular momentum. Two non-radiative decay processes involve IC in organic molecules, one from T to S, which competes with phosphorescence, and the other from S to T, competing with fluorescence and IC from the lowest

singlet excited state. Phosphorescence is a radiative process that involves a change in the spin multiplicity. Due to its spin-forbidden nature, the corresponding excited state has a much longer lifetime, and thus, it can take longer than fluorescence.

## **1.4 MOLECULAR PROBES FOR AD DETECTION**

Molecular probes constitute a promising tool for the early detection of AD through simple blood tests. These small, if carefully designed, could selectively interact with the characteristic biomarkers of AD, A $\beta$  aggregates and NFT, present in the bloodstream years before the appearance of the first symptoms.

### **1.4.1 Development of molecular probes**

Molecular probes for detecting AD have been developed in different stages.<sup>25</sup> The first group of such species contained charged molecular structures (Figure 1.2a), for example, diazo dye Congo Red (CR) and Thioflavin (ThT) which can be mentioned here. CR was introduced more than one century ago as an A $\beta$  probe. Its hydrophilic functional group enhanced water solubility and binding affinity towards A $\beta$  plaque but limited blood-brain barrier (BBB) uptake. To overcome this limitation, the backbone structure of CR was modified, and some moieties were substituted, leading to the creation of new probes, such as ThT, which showed a moderate binding affinity for A $\beta$  aggregates.<sup>25</sup>

To improve the binding affinity and BBB crossing, other neutral molecular probes were synthesized and used, such as the molecule Pittsburgh (PIB), shown in Figure 1.2b. Neutral molecular probes have shown fast clearance kinetics compared to the charged molecular probes.<sup>25</sup>

Some studies have been performed to improve the fluorescence response while minimizing the background signal when binding to A $\beta$ .<sup>25</sup> In this regard, the focus has been on developing near

infrared fluorescent molecular probes (Figure 1.2c). To achieve the improved fluorescence response and minimized background signal, a  $\pi$ -conjugated backbone has been included in the structure of the linker, as shown in Tolan diphenylacetylene (FDDTP), an analog of 1,1-dicyano-2-((6-dimethylamino)naphthalene-2-yl)-propene (DDNP), a well-known molecular probe.

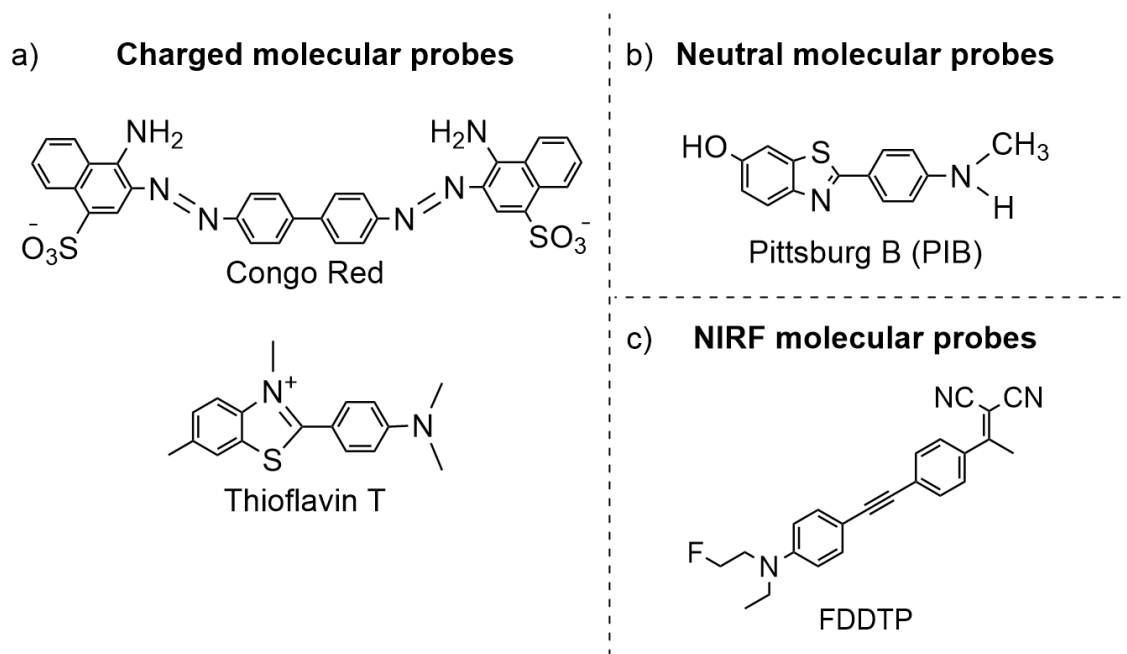


Figure 1.2: Structures of several widely used molecular probes for the detection of AD, a) charged molecules, b) neutral molecules, and c) near infrared molecular probes (NIRF)

Additionally, to enhance photon absorption and facilitate the charge transfer process in the excited state, the molecular probes have been strategically modified with donor (D) and acceptor (A) groups end caps, along with the  $\pi$ -linker. These new molecular probes are better known as donor-bridge-acceptor (DBA) molecular probes and are characterized for having a push-pull electron effect along the axis of the molecular structure.<sup>26</sup>

### 1.4.2 Properties and criteria of molecular probes for AD detection

To effectively detect AD *in vivo* and *in vitro*, using fluorescent microscopy, autoradiography, and PET imaging, molecular probes must meet specific criteria, the main points described below.

Molecular probes must be highly selective and have a high binding affinity towards A $\beta$  aggregates and NFT.<sup>26,27</sup> They should fluoresce only when interacting with the target proteins and not emit any signal in free form or when interacting with other proteins, as shown in Figure 1.3. They should be highly sensitive to the environment to be able to differentiate surroundings and display a bathochromic shift to the NIR.<sup>25</sup>

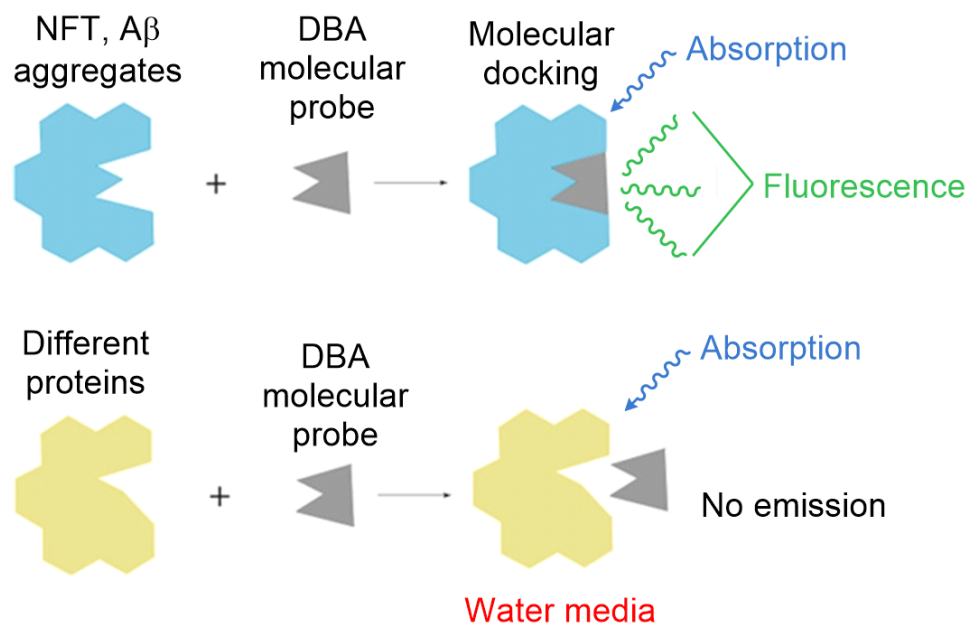


Figure 1.3: Schematic illustration of the working principle of DBA molecular probes, designed to emit a fluorescent signal when binding to biomarkers and not emit signals when dissolved in the aqueous solution.

Molecular probes should preferably have a built-in push-pull mechanism to allow the unconstrained charge transfer inside the molecule, which expectedly leads to advantageous and tunable photophysics. It can be achieved by having an electron-donating group (EDG) and an electron-withdrawing group (EWG) at the opposite ends of the molecule and a  $\pi$ -conjugated structure as the linker, better known as the bridge.<sup>26,28</sup>

Molecular probes will also need a large Stokes Shift to separate excitation light from emitted fluorescence, reducing the background interference and a rod-like geometry to facilitate the docking process (i.e., in the tyrosine channel of p-Tau).<sup>27</sup> Additionally, molecular probes should have a high quantum yield to ensure clear fluorescence signals.<sup>27–29</sup>

Let us suppose that early detection is performed using blood samples in combination with fluorescence microscopy. In that case, the molecular probes need to absorb and emit light in the blood window, which means between 700 to 900 nm, so near infrared (NIR) emission maxima wavelength is a key factor.<sup>26,28</sup> Ideally, the molecular probes need to be stable in blood, and low binding affinity to serum albumin.<sup>28</sup>

#### **1.4.3 Relevant studies – DBA molecular probes**

As explained above, DBA molecular probes should absorb and emit in the NIR region to be used in blood to detect AD. Some studies of new derivatives of DBA molecular probes to detect AD disease have been carried out recently. Our experimental collaborators, the research group led by Dr. Janez Košmrlj at the University of Ljubljana, Slovenia, synthesized several promising molecular probes for early AD detection.<sup>27</sup> Based on 2-(1-(6-((2-18[F]-Fluoroethyl)(methyl)amino)-2-naphthyl)ethylidene)-Malononitrile (FDDNP), they varied the length of the bridge part of these probes by including naphthalene, benzene, and ethylene building blocks to create new derivatives, and capping them with N-ethyl-N-(2-fluoroethyl) as EDG and 2-

dicyanovinyl groups as EWG groups. As shown in Figure 1.4, these studies found that four compounds were bound to the A $\beta$  and NFTs using fluorescent microscopy in pretreated brain slices (*in vitro* analysis). It was also demonstrated that biphenyl (Figure 1.4, **1e**) and diphenylacetylene (Figure 1.4, **1f**) analogs could differentiate A $\beta$  from p-Tau aggregates based on the wavelength maxima emission. Despite the positive results, there is room for improvement in selectivity and sensitivity since biomarkers at early stages are present in low concentrations in blood. To progress in this direction, it is essential to understand the influence of the EDG, EWG, and bridge segments over the absorption and emission energies of the probes. This knowledge will enable a more informed design approach to tune and enhance properties to achieve the desired outcomes.

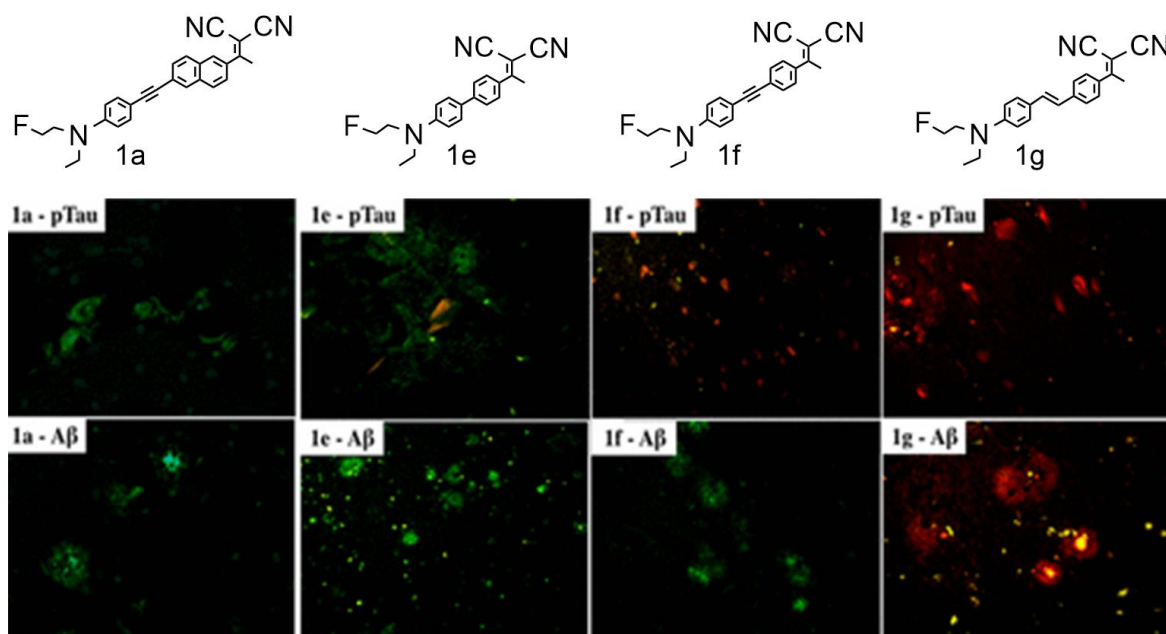


Figure 1.4: In vitro fluorescence microscopy using Alzheimer's disease brain tissue and inspected and synthesized molecular probes **1a**, **1e**, **1f**, and **1g**. Reprinted (adapted) with permission from J. Med. Chem. 2017, 60, 21, 8741–8757. Copyright 2017 American Chemical Society.

## 1.5 RESEARCH OBJECTIVES AND HYPOTHESIS

The main goal of the present study is to gain a deeper understanding of how EDG, EWG, and bridge/linker affect the absorption of energy and photophysics of these species. My dissertation work is performed with computational approaches. Specific aims have been set out to achieve the general goal outlined below.

### **Aim 1: Select the level of theory for geometry optimization of DBA molecular probes in the ground state ( $S_0$ )**

- a) Optimize the molecular probes in the ground state in the gas phase using density functional theory (DFT) to find the appropriate level of theory that reproduces the experimental X-ray diffraction (XRD) values.
- b) Optimize the molecular probes in the ground state in different solvents (dichloromethane, methanol, acetonitrile, and hexane) to see if the media influences the equilibrium structures.

### **Aim 2: Study the nature and the change of geometry of DBA molecular probes in the excited state ( $S_1$ )**

- a) Conduct single-point calculations using TD-DFT in different solvents (dichloromethane, methanol, acetonitrile, and hexane) using the ground state equilibrium geometry at various levels of theory to find the optimal functional and basis set for accurately modeling experimental absorption energies.
- b) Optimize the molecular probes in the excited state in different solvents using time-dependent density functional theory (TD-DFT) to analyze the geometry change in the excited state and reveal the nature of the electronic transition.

- c) Perform potential energy surface (PES) and oscillator strength ( $f_{osc}$ ) scans varying the dihedral angle between the EDG and EWG planes to analyze the Stokes shift and find the probability of absorption/emission, respectively.

**Aim 3: Study the influence of EDG, EWG, and bridge on the absorption energy**

- a) Perform a systematic study to evaluate the effect of EDG, EWG, and bridge on the absorption energy.
- b) Quantify unique structural modifications in the EWG by introducing more electronegative atoms within the ring, investigating pyranone derivatives and their functionalization to determine their effect on the absorption energy.
- c) Evaluate if the generated quantum chemistry data can be used to train machine learning (ML) models to predict the absorption energies of new molecular probes.

We hypothesized that the solvent will influence the geometry optimization of the molecular probes, given the known solvatochromism, and that there will be a geometry change in the excited state. We also hypothesized that EDG, EWG, and bridge will influence the absorption energy values. Moreover, we expected that the systematic study of varying these factors will provide insights and allow us to quantify their effects on the absorption energy. We also anticipated that introducing more electronegative atoms to the EWG and studying pyranone derivatives and their functionalization will affect the absorption energy. Finally, we hypothesized that the quantum chemistry data generated from these studies can be used to train machine learning models for predicting the absorption energies of new molecular probes.



## 1.6 CHAPTERS DESCRIPTION AND STUDY APPROACH

This dissertation is organized into five chapters. Chapter one contains a literature review that includes generalities of Alzheimer's disease, current detection techniques, and new horizons. It also includes a brief overview of the photochemistry of organic compounds, with an introduction to the excited state processes and their properties. Chapter two contains the introduction of the main fundamental concepts behind the computational approaches I utilized in my work, such as density functional theory (DFT) and time-dependent density functional theory (TD-DFT). This chapter also describes the applied methodologies and provides a general explanation of the calculations performed in my studies. Chapters three and four contain the main findings of the research and comprise specific studies submitted to scientific journals and are currently under revision. Chapter five contains the key conclusions of my dissertation studies and future work prospects.

The detailed studies presented in chapters three and four are described below:

### **Chapter 3: Versatile CN-Substituted Benzene, Pyridine, and Pyrimidine-Based Fluorescent Probes for Amyloid- $\beta$ Detection: A Structure-Spectroscopic-Activity Relationship Study**

This chapter presents the computational part of a study performed in collaboration with an experimentalist of the Košmrlj group at the University of Ljubljana. It constitutes studying the excited state of fluorescent probes consisting of phenyl- and phenylacetylene-cores developed from the structural framework of FDDNP, 2-(1-{4'-(ethyl[2-fluoroethyl]amino)-[1,1'-biphenyl]-4-yl}ethylidene)malononitrile (FDDBP), and 2-(1-{4-[(4-{ethyl[2-fluoroethyl]amino}phenyl)ethynyl]phenyl}ethylidene)malononitrile (FDDTP). The study

included three EWGs, three EDGs, and two linkers. Potential energy surface and oscillator strength scans were performed to understand the process better.

#### **Chapter 4: Photophysics of molecular probes for Amyloid- $\beta$ detection: Computational Insights into Roles of Probe Linker and Functional Groups**

This chapter describes a systematic computational study of a combination of six different families of molecular probes defined by their bridge, four EDG groups, and four EWG groups and examines the influence of structure on absorption energies. Twelve additional structural modifications were studied, of which six introduce more electronegative atoms in the EWG ring, and the remaining six include pyrazone derivatives and their functionalized forms. Several preliminary design rules were derived from the study. The study also demonstrates that machine learning models can be trained on the generated quantum datasets, which can predict the absorption energies of new molecular probes.

## Chapter 2: Methodology

This chapter provides a comprehensive overview of the methodology employed in my research. It also includes some fundamental concepts significant in quantum mechanics, including density functional theory (DFT) and time-dependent density functional theory (TD-DFT), essential for better comprehension of the work undertaken.

### 2.1 SCHRÖDINGER EQUATION

In quantum mechanics, the state of a system is represented by a mathematical function known as the wave function ( $\Psi$ ), which comprises all its information. Whenever the system changes over time, the time-dependent Schrödinger equation can be used to find its variations in time by solving equation 1.<sup>30</sup>

$$\hat{H}\Psi(r, t) = E\Psi(r, t) \quad (\text{eq. 1})$$

Where  $\hat{H}$  is the Hamiltonian (energy operator),  $\Psi(r, t)$  is the wave function, which depends on the position coordinates of the particles (electrons and nuclei) in the system and time, and  $E$  is the energy eigenvalue. The Hamiltonian of a quantum system specifies the total energy of the system, meaning the sum of kinetic energy (term 1 in eq. 2, the kinetic energy operator  $\hat{T}$ ) and potential energies (term 2 in eq. 2, the potential energy operator  $\hat{V}$ ) in all the dimensions for a non-perturbed system (cartesian coordinates  $x$ ,  $y$ , and  $z$ ), which means in the absence of external electric and magnetic fields.

$$\hat{H} = \hat{T} + \hat{V} = \frac{\hbar^2}{2m} \nabla^2 + V(i) \quad (\text{eq. 2})$$

where:

$$\hbar = \frac{h}{2\pi} \quad (\text{eq. 3})$$

$$\nabla^2 = \frac{\partial^2}{\partial x^2} + \frac{\partial^2}{\partial y^2} + \frac{\partial^2}{\partial z^2} \quad (\text{eq. 4})$$

$h$  = Planck constant

$m$  = mass of the particle

Solving Equation 2 represents a significant challenge in physics as it involves solving a many-body problem, which becomes more complicated when trying to describe and understand the behavior of many interacting particles. These many body systems, such as molecules, consist of various particles (i.e., atoms), and each particle has its nucleus and electrons with their independent coordinates (dimensions). Since each particle interacts with every other particle, the complexity of these interactions increases, making it very difficult to find an analytical solution. This challenge becomes even more pronounced in larger systems.

To address this challenge, key approximations were introduced early on to solve the Schrödinger equation.<sup>31</sup> The Born-Oppenheimer approximation, for example, significantly simplifies the solution of equation 1 by assuming that atomic nuclei have much slower motions than electrons because of their mass difference. Consequently, the movement of the electrons is considered instantaneous for a specific nuclear configuration. Within this approximation, the nuclei-nuclei interactions would be constant, and they do not need to be considered in the evaluation of the wavefunction, and the kinetic energy of nuclei becomes zero when considering the electronic wavefunction. This allows the separation of the Hamiltonian to two terms (as a sum), one describing the physics of the nuclei and the other the electrons, with which the wavefunction also separates (as a product) to one nuclei and one electron wavefunctions. The latter only depends on electron coordinates, spatial and spin.<sup>32,33</sup>

The more widely used method for solving electronic structures in quantum chemistry is the Hartree-Fock method (HF).<sup>33-35</sup> It approximates the electronic wave function of the entire system

in the form of a determinant (Slater determinant), i.e., as the sum of a series of products of one-electron wavefunctions. This approximation neglects electron-electron correlation effects, mainly considering that the electrons move in a mean-field generated by the other electrons.<sup>34</sup> This approach simplifies the many-body problem into a series of intertwining equations for wave functions of individual electrons, as can be seen in equation 5, which can be solved iteratively to obtain self-consistent solutions for the electronic structure of molecules.<sup>36</sup>

$$\Psi(x_1, x_2, \dots, x_n) = \frac{1}{\sqrt{n!}} \begin{vmatrix} \psi_1(x_1) & \psi_1(x_2) & \dots & \psi_1(x_n) \\ \psi_2(x_1) & \psi_2(x_2) & \dots & \psi_2(x_n) \\ \vdots & \vdots & \ddots & \vdots \\ \psi_n(x_1) & \psi_n(x_2) & \dots & \psi_n(x_n) \end{vmatrix} \quad (\text{eq. 5})$$

This approach is considered rudimentary because it assumes that electrons in a system are, beyond electrostatics and the Pauli principle, independent of each other, which is not true in real systems. Certainly, electron-electron dynamic interactions are significant and play a crucial role. Thus, we need to consider the electron-electron correlation energy terms to account for these interactions. This term for two electrons, which can be called the correlation energy  $E_{corr}$ , represents the difference between the exact energy from the Born-Oppenheimer (BO) approximation and the HF energy, as shown in equation 6.

$$E_{corr} = E_{BO} - E_{HF} \quad (\text{eq. 6})$$

The correlation energy term is small compared to the total energy; nevertheless, it becomes important as the number of electrons in the system increases, and it has an order of magnitude that is relevant in chemistry (1 kJ mol<sup>-1</sup> to a few eV). So, accounting for electron correlations is crucial to model chemical phenomena.

## 2.2 DENSITY FUNCTIONAL THEORY (DFT)

In 1964, Hohenberg and Kohn formulated a theory alternative to the wavefunction formulation, which is the foundation of computational chemistry, called density functional theory (DFT).<sup>37</sup> The fundamental principle of DFT is that electron density ( $\rho$ ), representing the spatial distribution of electrons, can completely determine the ground state electronic energy of a system as established by the Hohenberg-Kohn theorems.<sup>36</sup> These theorems have two key statements; the first is that all the properties of a system can be determined from  $\rho$  since it has a direct relationship with the Hamiltonian ( $\hat{H}$ ). Meanwhile, the second theorem states that the electron density ( $\rho$ ) that produces the lowest energy corresponds to the electron density in the ground state of the system ( $\rho_0$ ).<sup>36</sup>

While the Hohenberg-Kohn theorems established the existence of the density functional in DFT, they do not provide the specific form of the energy functional. To address this problem, especially that the formulae of kinetic energy functional of the density is unknown, Walter Kohn and Lu Jeu Sham introduced the Kohn-Sham equation, which uses an auxiliary wave function and prior energy functional, simplifying the problem considerably. In other words, they replaced the interactive functionals with noninteraction functionals and expressed all errors by a term known as exchange-correlation functional ( $E_{xc}[\rho]$ ). Consequently, the resulting Kohn-Sham equation is based on electron density and the exchange-correlation functional. The main task of the DFT approach is to find an exchange-correlation functional that can accurately describe the real system.<sup>38</sup>

The accuracy of DFT calculations depends heavily on the choice of the exchange-correlation functional, which accounts for the effects of electron exchange and correlation. This functional is essential for describing electron-electron interactions beyond the mean-field

approximation. Unfortunately, the exact form of the exchange-correlation functional is unknown, so various approximations are used in practice, which gives origin to many different DFT functionals that are developed as approximations of the exact exchange-correlation functional.

Figure 2.1 illustrates the Jacob's ladder diagram, which tries to classify and rank the relationship between the approximation methods for the exchange-correlation functionals. The complexity, computational cost, and performance of the functionals increase from bottom to top.

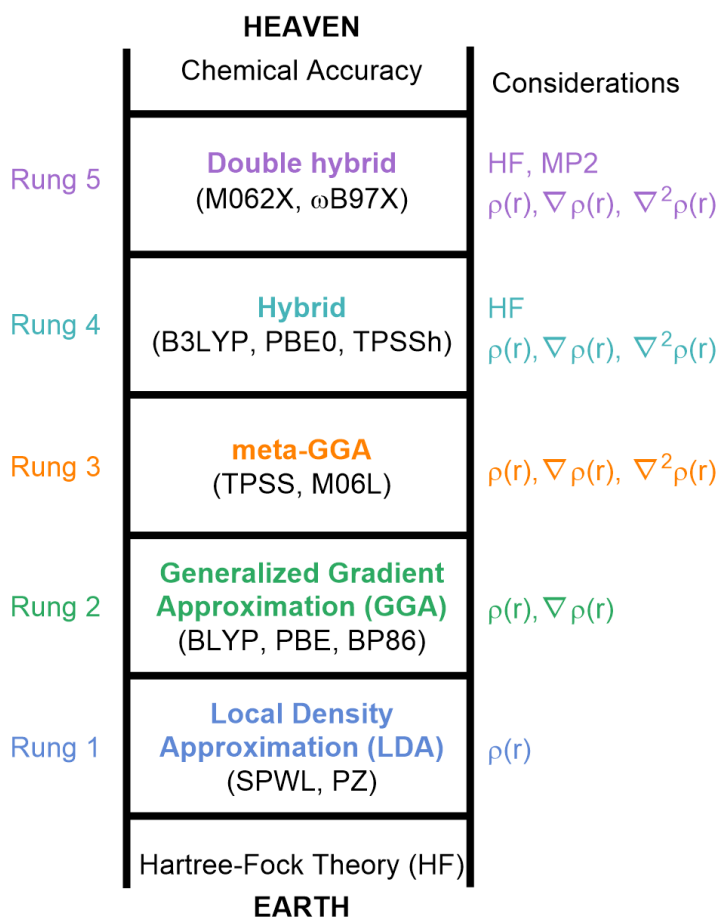


Figure 2.1: Jacob's ladder of functionals employed in DFT

The Local Density Approximation (LDA), rung 1 in Figure 2.1, is a commonly used DFT method to estimate the exchange-correlation energy. It simplifies the calculations by assuming that charge density changes slowly in a non-uniform electronic system and that the exchange-

correlation energy at a specific point in space is determined only by the electron density at that point.<sup>39</sup> This approximation provides reasonable accuracy for many systems and is computationally efficient. However, the LDA may not accurately represent certain non-local effects, especially in systems with strong electron-electron interactions or highly delocalized electrons.<sup>40</sup> Some examples of LDA functionals are SPWL, PZ, GVWN, and GPW92.

The generalized gradient approximation (GGA), rung 2 in Figure 2.1, includes a gradient correction of charge density, considering that it is not uniformly distributed as the ideal free electron gas. In this approximation, the exchange-correlation effect is calculated considering two functional forms, one for the exchange energy and the other for the correlation energy. Some examples of GGA functionals are BLYP, PBE, and PB86. Although these functionals exhibit better performance than the LDA family, they still face difficulties in accurately describing excited states, reaction energetics, and spin state energetics.<sup>41,42</sup>

Meta GGA functionals, rung 3 in Figure 2.1, are more computationally expensive than LDA and GGA since they allow the exchange and correlation functionals to depend on higher-order derivatives of electron density. As an alternative, the functional can depend on the kinetic energy density. They are more accurate than LDA and GGA when calculating vibrational frequencies, weak interactions, hydrogen bonds, and formation enthalpies.<sup>42,43</sup> Some examples of meta-GGA functionals are TPSS and M06L.

Hybrid functionals, rung 4 in Figure 2.1, include hybrid GGA and meta-GGA. These functionals are constructed from linear combinations of the exchange energy in the Hartree-Fock method and the exchange energy in the DFT method. Considering that the Hartree-Fock self-consistent field provides an accurate exchange energy, the exchange-correlation functional obtained using this method is normally more accurate than the one obtained by pure DFT methods.



Remarkably, when using this method, the calculated results are closer to the experimental values since the linear combination coefficients can be adjusted.<sup>38</sup> Some examples of hybrid GGA functionals are B3LYP and PBE0, and hybrid meta-GGA includes TPSSh.<sup>44</sup>

Double hybrid functionals, rung 5 in Figure 2.1, include the complete information of the orbitals, not only the occupied but also the virtual. These functionals have reached the highest accuracy to date. Nevertheless, their application in large systems is complex due to their high computational cost.<sup>45</sup> Here, M062X and  $\omega$ b97-x can be mentioned as examples.<sup>36</sup>

The wavefunction of a system is generally expressed in terms of one-electron orbitals (i.e., the MO approach). Since the exact form of the wave function is unknown, the MOs are represented as linear combinations of known functions (i.e., basis sets). To obtain high-quality wave functions, a sufficiently large basis set is required. Among the most used basis sets in computational chemistry are Gaussian-type orbitals (GTOs), real-space functions, Slater-type orbitals (STOs), and plane-waves (PW).<sup>46</sup>

The STOs are of higher quality and need more computational resources compared to GTOs. However, it is possible to enhance the accuracy of GTOs by increasing the number of Gaussian functions used. Additionally, they are widely used in large-scale computational chemistry calculations since the two-electron-containing Gaussian functions can be analytically solved at a lower cost.<sup>47</sup>

## 2.3 TIME-DEPENDENT DENSITY FUNCTIONAL THEORY (TD-DFT)

Density Functional Theory (DFT) is widely used to analyze the ground-state electronic structure of systems. However, it has limitations when describing electronic excitations. Time-dependent density Functional Theory (TD-DFT) considers the time-dependent nature of

electromagnetic waves, which makes it useful for treating electronically excited states that usually come from the interaction of the molecular electron structure with light. By enabling the investigation of excited states and their properties, TD-DFT is particularly useful in the study of optical and spectroscopic phenomena.<sup>48</sup>

TD-DFT introduces time dependence by considering time-dependent external perturbations, such as electromagnetic fields, which induce electronic excitations. This leads to the time-dependent Kohn-Sham equations, where the electronic density becomes a function of both space and time. It involves propagating the electronic density in time under the influence of external perturbation. This treatment allows the determination of excitation energies and oscillator strengths ( $f_{osc}$ ), which are calculated following the Thomas-Reiche-Kuhn sum rule and represent the transition probabilities.<sup>49,50</sup> The accuracy of TD-DFT depends on the choice of exchange-correlation functional, which must adequately capture both ground and excited-state properties. TD-DFT methods effectively study how molecules behave in time-dependent fields under weak excitations. Nevertheless, when it comes to strong excitations like those induced by laser fields, other approaches like real-time time-dependent density functional theory (RT-TDDFT) are more appropriate.<sup>51</sup>

## 2.4 GENERAL METHODOLOGY APPLIED IN THE STUDIES AND INPUT EXAMPLES

The methodology employed in this dissertation comprises the application of DFT and TD-DFT methods implemented in Gaussian16 revision B.01.<sup>52</sup> Some of the initial geometries of the studied molecules were taken from X-ray experimental structures or built *in silico*. Ground and excited-state gas-phase geometry optimizations were conducted using the B3LYP<sup>53–55</sup> functional and the cc-PVTZ<sup>56</sup> basis set at the ultrafine grid. Vibrational frequency calculations at the same

level of theory were performed to confirm the equilibrium structures, which were then verified as minima on the potential energy surface (PES).

To gain insight into the charge transfer transitions occurring within the system, an analysis of the topology and composition of the frontier HOMO and LUMO orbitals (generated from the computed gas-phase wave functions at the B3LYP/cc-PVTZ level) was conducted using Mulliken partition analysis as implemented in Multiwfn software v.3.8<sup>57</sup>, and the visualizations were carried out with VMD 1.9.3.<sup>58</sup>

TD-DFT excited-state geometry optimizations were carried out on the optimized ground-state geometries of molecular probes at the B3LYP/cc-PVTZ level of theory. Electron density difference maps (EDDMs) for  $S_0 \rightarrow S_1$  transitions were generated at the same level of theory by subtracting the electron density of the  $S_0$  state from that of the  $S_1$  state. TD-DFT single-point calculations were used to refine the vertical absorption energies at the M062X<sup>59</sup> level of theory, and the universal solvation model based on solute electron density (SMD)<sup>60</sup> as implemented in Gaussian16 revision B.01<sup>52</sup> was used to consider solvent effects. The linear regression analyses were performed in Origin 2022b software.

Herein, examples of the input for Gaussian 16 used in each type of calculation are provided using molecule 2-(1-(6-((4-(Ethyl(2-fluoroethyl)amino)phenyl)ethynyl)-naphthalen-2-yl)ethylidene)malononitrile (**6iia**) as an example. These examples can be used to calculate the properties of new molecular probes by changing the XYZ coordinates, charge, and multiplicity.

Input file for the geometry optimization of the ground state ( $S_0$ ) and frequency calculation:

```
%mem=32GB
%nprocshared=4
%chk= 6iia_opt_01.chk
#p B3LYP/cc-PVTZ opt freq=savenm EmpiricalDispersion=GD3
```

6iia\_opt\_01

0 1

C	-2.04412665	-7.07422268	5.36202705
C	-1.69994381	-6.46464377	4.18112303
C	-0.97511772	-5.24123432	4.18464583
C	-0.61151296	-4.65827103	5.42606874
C	-0.98079038	-5.31116157	6.63381638
C	-1.68117164	-6.49202397	6.60075248
H	-0.89223632	-5.04840592	2.01929213
H	-1.97771810	-6.90964658	3.21388746
C	-0.60578064	-4.58802486	2.97671867
C	0.11344031	-3.43485073	5.42869026
H	-0.69424370	-4.85082419	7.59112484
H	-1.96848438	-6.99978994	7.53323405
C	0.45743352	-2.82505592	4.24777266
C	0.09416261	-3.40734417	3.00895544
H	0.39142283	-2.98955497	6.39575063
H	0.38144777	-2.89946920	2.07653257
C	-2.82915329	-8.39911255	5.36191505
C	-3.44147408	-9.43252664	5.36182769
C	-4.22650072	-10.75741651	5.36171569
C	-4.56912533	-11.36527751	6.56984847
C	-4.59509335	-11.34966824	4.15385581
C	-5.27959635	-12.56546609	6.57001767
H	-4.27771781	-10.89850060	7.52192134
C	-5.30663999	-12.54971460	4.15386428

H	-4.32528822	-10.87062294	3.20156918
C	-5.64880499	-13.15773152	5.36166210
H	-5.54914691	-13.04497093	7.52223305
H	-5.59748166	-13.01623621	3.20137128
N	-6.39769224	-14.42266931	5.36217557
C	-7.74562799	-15.00777899	5.40237346
H	-7.75914408	-15.91200393	4.83045163
H	-8.01088543	-15.22310502	6.41636221
C	-5.60751187	-15.45964257	6.04129370
H	-6.05856529	-16.41604741	5.87776817
H	-4.61185365	-15.46317921	5.64943631
C	1.85348983	-1.26558591	5.64181267
H	2.49420143	-0.40918082	5.61084556
H	1.07013281	-1.09948561	6.35150449
H	2.42089732	-2.12523163	5.93156768
C	1.24214979	-1.49998220	4.24792540
C	1.37647353	-0.66625739	3.18800696
C	0.71170613	-1.01971752	1.84459703
C	2.19159989	0.63340414	3.32235320
N	0.21675659	-1.28288466	0.84436727
N	2.79849852	1.60106123	3.42238008
C	-5.56352793	-15.16439701	7.55208669
H	-5.73841368	-16.06826287	8.09737697
H	-4.60234399	-14.77196542	7.81097447
H	-6.31926590	-14.44782464	7.79761502
C	-8.75652514	-14.00943439	4.80823963
H	-9.10376298	-13.35261443	5.57824835

H	-8.28234099	-13.43726420	4.03838857
F	-9.80286679	-14.68485765	4.28720933

Once the ground state geometry ( $S_0$ ) is optimized, the coordinates of the output file, extension .log for Gaussian 16, will serve as the initial structure for running the excited state optimization ( $S_1$ ).

Example input file for the geometry optimization of the excited state ( $S_1$ ) using the same molecule and Gaussian 16 is as follows:

```
%mem=32GB

%nprocshared=8

%chk=6iia_optes_01.chk

#p B3LYP/cc-PVTZ opt TD=(Root=1, Nstates=1) scf(noincfock,novaracc,xqc)

6iia_optes_01

0 1

C    -1.570551000    0.812002000   -0.198298000
H    -1.053758000    1.762046000   -0.184439000
C    -0.837424000   -0.364310000   -0.191092000
C    -1.531268000   -1.610828000   -0.210204000
H    -0.954154000   -2.524477000   -0.201766000
C    -2.894994000   -1.652567000   -0.236015000
H    -3.410515000   -2.604128000   -0.244048000
C    -3.660970000   -0.459046000   -0.240159000
C    -5.067612000   -0.478041000   -0.257108000
```

H	-5.560907000	-1.438144000	-0.292410000
C	-5.810374000	0.689289000	-0.263948000
C	-5.116438000	1.933559000	-0.273953000
H	-5.675348000	2.857848000	-0.281826000
C	-3.752221000	1.980776000	-0.239865000
H	-3.244236000	2.936409000	-0.226318000
C	-2.977136000	0.793444000	-0.223002000
C	-7.276946000	0.676509000	-0.312281000
C	-7.947012000	1.748433000	-1.124887000
H	-7.405291000	1.918537000	-2.054209000
H	-7.944704000	2.690826000	-0.570922000
H	-8.982302000	1.507335000	-1.349927000
C	-8.038445000	-0.237817000	0.358919000
C	-7.516581000	-1.217900000	1.257174000
C	-9.462735000	-0.245072000	0.244589000
C	0.577207000	-0.346449000	-0.165012000
C	1.786350000	-0.336423000	-0.136677000
C	3.200204000	-0.324639000	-0.103141000
C	3.921091000	0.879079000	-0.093413000
H	3.381698000	1.816132000	-0.108022000
C	5.300340000	0.895347000	-0.056248000
H	5.796009000	1.853097000	-0.032994000
C	6.049367000	-0.301205000	-0.031050000

C	5.320351000	-1.509967000	-0.045436000
H	5.833084000	-2.458458000	-0.044699000
C	3.940694000	-1.516055000	-0.077110000
H	3.416625000	-2.461825000	-0.089661000
C	8.185321000	0.938178000	-0.159236000
H	9.147455000	0.701127000	-0.614526000
H	7.680882000	1.617448000	-0.846078000
C	8.431432000	1.642133000	1.169503000
C	8.207626000	-1.519262000	0.104765000
H	7.706890000	-2.214285000	0.778553000
H	9.155134000	-1.272078000	0.585924000
N	7.428878000	-0.288973000	0.013554000
N	-7.133924000	-2.018993000	1.992350000
N	-10.612043000	-0.249505000	0.153148000
C	8.473064000	-2.176552000	-1.250127000
H	7.539767000	-2.438535000	-1.747234000
H	9.065113000	-3.084690000	-1.127131000
H	9.023003000	-1.500086000	-1.905625000
H	7.493484000	1.930961000	1.645762000
H	8.991684000	1.000017000	1.852352000
F	9.180664000	2.794613000	0.940639000



Once we complete the excited state optimization, a frequency calculation should be carried out at the same level of theory to ensure that we are at the minimum potential energy surface (PES).

The example input file for the frequency calculation ( $S_1$ ) of the same molecule is as follows:

```
%mem=32GB
%nprocshared=8
%chk=6iia_freq_01.chk
#p B3LYP/cc-PVTZ freq=savenm TD=(Root=1, Nstates=1) scf(noincfock,novaracc,xqc)

6iia_freq_01

0 1
C   -1.583827000    0.850487000    0.441657000
H   -1.101066000    1.633041000    1.013315000
C   -0.816445000   -0.071622000   -0.260554000
C   -1.460504000   -1.093059000   -1.006827000
H   -0.863990000   -1.811797000   -1.551745000
C   -2.824930000   -1.170201000   -1.032957000
H   -3.308865000   -1.955804000   -1.598277000
C   -3.639989000   -0.241810000   -0.323500000
C   -5.039602000   -0.314245000   -0.346164000
H   -5.481055000   -1.098709000   -0.936871000
C   -5.857071000    0.593652000    0.354117000
C   -5.163768000    1.619696000    1.085210000
H   -5.737302000    2.342924000    1.644657000
C   -3.805941000    1.712123000    1.123600000
H   -3.335516000    2.499997000    1.699653000
```

C	-2.983399000	0.786458000	0.423622000
C	-7.292642000	0.565074000	0.366296000
C	-8.024346000	1.762983000	0.922520000
H	-7.631412000	2.698658000	0.521060000
H	-7.940325000	1.818994000	2.013072000
H	-9.084560000	1.723342000	0.689777000
C	-8.088903000	-0.512181000	-0.092404000
C	-7.623820000	-1.789923000	-0.481659000
C	-9.501762000	-0.407359000	-0.141027000
C	0.603716000	0.001368000	-0.233253000
C	1.817807000	0.054536000	-0.215823000
C	3.218192000	0.109396000	-0.198036000
C	3.970219000	-0.571412000	0.794182000
H	3.438441000	-1.139593000	1.542420000
C	5.335725000	-0.524987000	0.815433000
H	5.859582000	-1.068020000	1.584608000
C	6.060266000	0.211605000	-0.169505000
C	5.304840000	0.898552000	-1.166768000
H	5.804509000	1.482236000	-1.921598000
C	3.939400000	0.846098000	-1.173003000
H	3.383106000	1.376279000	-1.931250000
C	8.210484000	-0.355786000	0.904084000
H	9.137864000	0.206464000	0.994466000
H	7.697946000	-0.280421000	1.858919000
C	8.549400000	-1.817179000	0.603917000
C	8.191215000	0.954838000	-1.198374000
H	7.694542000	0.830720000	-2.156630000

H	9.144979000	0.435481000	-1.274758000
N	7.414617000	0.257586000	-0.159041000
N	-7.287774000	-2.851510000	-0.805875000
N	-10.657509000	-0.329352000	-0.184975000
C	8.422775000	2.430820000	-0.880333000
H	7.483418000	2.978471000	-0.821347000
H	9.031899000	2.878891000	-1.664314000
H	8.948885000	2.554708000	0.065788000
H	7.654615000	-2.440224000	0.575460000
H	9.081684000	-1.915088000	-0.343630000
F	9.370527000	-2.272797000	1.617751000

To calculate the absorption energies, the coordinates of the ground state optimized structure ( $S_0$ ) are used to perform single-point calculations. Herein is an example of input for the single point calculation for the same molecule as above, using dichloromethane as solvent.

```
%mem=16GB
%nprocshared=4
%chk=6iia_sp_01.chk
#p M062X/cc-PVTZ SP SCRF=(SMD,Solvent=Dichloromethane,read) TD=(Root=1,
Nstates=10) scf(noincfock,novaracc,xqc)
```

```
6iia_sp_01
```

```
0 1
```

C	0.766973000	-0.556293000	-0.178125000
C	1.642890000	0.516355000	-0.227325000

C	3.036339000	0.320298000	-0.250069000
C	3.557000000	-1.008563000	-0.226101000
C	2.645407000	-2.094437000	-0.175868000
C	1.298153000	-1.880675000	-0.152611000
H	3.570750000	2.410042000	-0.348187000
H	1.250943000	1.524168000	-0.246441000
C	3.954005000	1.398944000	-0.305498000
C	4.949893000	-1.201507000	-0.257125000
H	3.034778000	-3.104433000	-0.155354000
H	0.610280000	-2.713308000	-0.113726000
C	5.834900000	-0.135762000	-0.275614000
C	5.302423000	1.183821000	-0.311104000
H	5.318664000	-2.217705000	-0.238036000
H	5.970405000	2.028487000	-0.372637000
C	-0.633983000	-0.360137000	-0.152031000
C	-1.833357000	-0.205455000	-0.127914000
C	-3.234818000	-0.018167000	-0.098723000
C	-4.117439000	-1.108040000	-0.055120000
C	-3.800774000	1.265618000	-0.111462000
C	-5.485250000	-0.929505000	-0.022593000
H	-3.715013000	-2.111552000	-0.039280000
C	-5.167558000	1.454100000	-0.084856000
H	-3.149148000	2.127659000	-0.150615000
C	-6.059007000	0.360545000	-0.036721000
H	-6.110408000	-1.807060000	0.027958000
H	-5.542135000	2.464691000	-0.114601000
N	-7.426434000	0.543302000	0.002671000

C	-8.347534000	-0.570759000	-0.133871000
H	-9.267183000	-0.215802000	-0.600106000
H	-7.943722000	-1.335562000	-0.796914000
C	-8.024846000	1.873020000	0.051230000
H	-8.997953000	1.776532000	0.535014000
H	-7.431981000	2.511955000	0.705534000
C	7.760903000	-1.602688000	-1.039317000
H	8.832142000	-1.580373000	-1.218201000
H	7.546529000	-2.503178000	-0.458227000
H	7.238081000	-1.698945000	-1.989629000
C	7.281324000	-0.387878000	-0.295292000
C	8.188003000	0.411457000	0.341654000
C	7.845962000	1.510328000	1.187513000
C	9.591760000	0.156676000	0.257560000
N	7.611934000	2.396296000	1.886624000
N	10.724679000	-0.046615000	0.191124000
C	-8.194498000	2.517610000	-1.324975000
H	-8.652508000	3.503607000	-1.233442000
H	-7.233429000	2.629450000	-1.825570000
H	-8.834207000	1.904949000	-1.961477000
C	-8.688819000	-1.190493000	1.215618000
H	-7.800011000	-1.591466000	1.704721000
H	-9.154089000	-0.455093000	1.875329000
F	-9.591151000	-2.234270000	1.020378000

## Chapter 3: Versatile CN-Substituted Benzene, Pyridine, and Pyrimidine-Based Fluorescent Probes for Amyloid- $\beta$ Detection: A Structure-Spectroscopic-Activity Relationship Study

### 3.1 INTRODUCTION

Understanding the structural and physiological aspects of living cells and tissues requires special tools, including fluorescent molecular probes<sup>61</sup>. Previous studies developed and applied molecular probes for various functions. For example, small molecules such as 2,3-naphthotriazol have been shown as applicable for nitric oxide detection<sup>62</sup>, phenaline-1,3-dione derivatives for cysteine oxidation detection<sup>63</sup>, rhodamine derivatives have been employed in bioimaging and biosensing<sup>64</sup>, and larger molecules like the green fluorescent protein has been used as a biomarker in various research studies.<sup>65–67</sup>

Small fluorescent molecular probes have generated significant interest, as reported in several reviews.<sup>61,68–70</sup> According to the literature<sup>11–13</sup>, small fluorescent molecular probes should have specific properties such as high and specific binding affinity to the target, excellent photostability, no overlapping between the absorption and emission spectra, and optical properties that are sensitive to the surrounding environment in response to their intrinsic excitation<sup>63,71</sup> or aggregation/self-assembly.<sup>72–74</sup>

Most dyes for use in biomedical optical imaging are charged molecules to improve their solubility in aqueous-based biological environments. One of the most famous and common examples is Thioflavin T (ThT) (Figure 3.1), a fluorescent dye considered the gold standard for *in vitro* detection of amyloid  $\beta$  (A $\beta$ ).<sup>75–78</sup> ThT exhibits a higher fluorescence intensity in solutions containing A $\beta$  fibrils due to steric immobilization<sup>79,80</sup>. When binding to A $\beta$ , the free rotation of the acceptor and donor fragments around the bridge is hindered, suppressing quenching and resulting in a high fluorescence quantum yield.<sup>81</sup> Nevertheless, this dye could not be widely implemented

because the charge makes the brain-blood-barrier permeability difficult and produces poor selectivity.<sup>82,83</sup>

To overcome this drawback, uncharged small molecule fluorophores have been studied for *in vivo* neuroimaging. For example, some studies have shown that FDDNP<sup>84</sup> and its analog DDNP<sup>85</sup> (Figure 3.1) can be fluorescent markers through fluorescence microscopy imaging for *ex vivo* detection of A $\beta$  and p-Tau aggregates. FDDNP, being neutral and having hydrophobic properties, is used to detect amyloid  $\beta$  aggregates *in vitro* and *in vivo*. However, it has some drawbacks, such as the lack of selective labeling of A $\beta$  and neurofibrillary tangles.<sup>86</sup> In a recent work<sup>27</sup>, the successful detection of A $\beta$  and p-Tau aggregates in the brain tissue of Alzheimer's disease patients using some FDDNP analogs, such as FDDBP and FDDTP, is described (Figure 3.1). These fluorophores improved the quantum yield and the Stokes shifts in dichloromethane (DCM) solutions when compared to DDNP and FDDNP. FDDBP showed higher affinity to A $\beta$  fibrils. Meanwhile, FDDBP exhibited high sensitivity when binding to p-Tau aggregates. Furthermore, FDDBP and FDDTP could distinguish A $\beta$  from p-Tau aggregates based on the emission of each biomarker (Figure 1.4, **1e** and **1f**)

Furthermore, other factors, such as the influence of heteroaromatic electron acceptor groups<sup>87</sup> and the molecular size of the probes<sup>88</sup>, have been the base for establishing the main structural requirements to have optimal binding and characteristics of new analogs. The molecular probes should be end-capped with a donor and acceptor connected at an appropriate distance by an unsaturated hydro-carbon linker to provide a proper dipole moment that induces a favorable emission maximum to be used in fluorescence microscopy. Also, they should be able to achieve planar conformation at a low energy cost to lead to favorable optical properties and a rod-shaped geometry to facilitate the docking process with the A $\beta$  and Tau aggregates channels. iii) Even

though the mechanism behind the interactions between the molecular probes and the amino acids is not completely known by structures, some molecular docking studies have shown that the introduction of heteroatoms could improve solubility and facilitate the formation of H-bonding.<sup>89,90</sup>

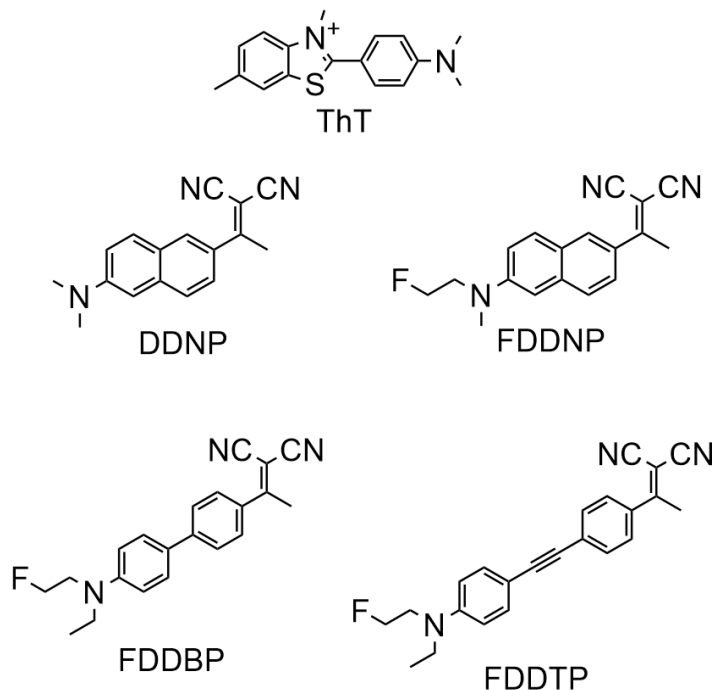


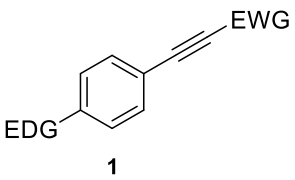
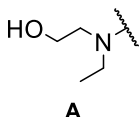
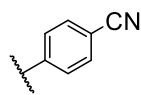
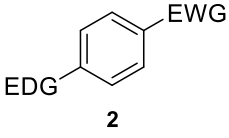
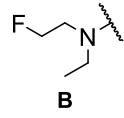
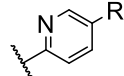

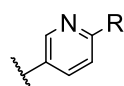
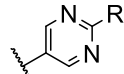
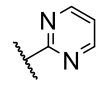
Figure 3.1: Chemical structures of Thioflavin T (**ThT**), 1,1-dicyano-2-[6-(dimethylamino)naphthalen-2-yl]propene (**DDNP**), its fluorinated derivative **FDDNP**, biphenyl analogue **FDDBP** and tolan (diphenylacetylene) analogue **FDDTP**.

This work describes the computational study of a series of new fluorescent probes consisting of phenyl- and phenylacetylene-cores developed from the structural framework of FDDNP, FDDBP, and FDDTP probes<sup>27</sup> (Table 3.1). The EWGs involve CN and unsubstituted benzene, pyridine and pyrimidine and the EDGs comprise N-ethyl-N-(2-hydroxyethyl)amino (**A**), N-ethyl-N-(2-fluoroethyl)amino (**B**), and dimethylamino (**C**) groups (Table 3.1), interconnected by phenylethynyl (**1**) and phenyl (**2**) linker. The main objective of the computational study is to



gain a deeper understanding of the behavior of these fluorophores in the excited state using the structure-spectroscopic relationship (SSR) based on variations in the acceptor and donor moieties.

Table 3.1: Structural building blocks of pyridinyl- and pyrimidinyl-bearing push-pull molecules. The resemblance of geometry and size with previously reported biphenyl and tolan FDDNP-analogues FDDBP and FDDTP, respectively, promises favorable spectroscopic and binding properties of the analogues.

HC framework	EDG	EWG
 <p>1</p>	 <p>A</p>	 <p>a</p>
 <p>2</p>	 <p>B</p>	 <p>b, R=H c, R=CN</p>
	 <p>C</p>	 <p>d, R=H e, R=CN</p>
		 <p>f, R=H g, R=CN</p>
		 <p>h</p>

### 3.2 METHODOLOGY

Density functional theory (DFT) and time-dependent DFT methods, as implemented in Gaussian16 revision B.01.,<sup>91</sup> were used to carry out the calculations at the HPC center of The University of Texas at El Paso (UTEP). Ground and excited-state gas-phase geometry optimizations were performed using the hybrid B3LYP<sup>53–55</sup> functional combined with the correlation-consistent triple- $\zeta$  valence basis set cc-PVTZ.<sup>56</sup> Vibrational frequency calculations at the B3LYP/cc-PVTZ level of theory were used to characterize the equilibrium structures and ensure that they correspond to the potential energy surface (PES) minima.

Subsequent TD-DFT single-point calculations refined vertical absorption energies at the M062X<sup>59</sup>/cc-PVTZ level of theory. Solvent effects were considered utilizing the universal

solvation model based on solute electron density (SMD)<sup>60</sup> employing the default setup implemented in Gaussian16 revision B.01.<sup>52</sup> Molecular orbitals were visualized and plotted using VMD 1.9.3.<sup>58</sup> Linear regression analyses were carried out in Origin 2022b software.

### 3.3 RESULTS AND DISCUSSION

We studied the photophysics of the prepared compounds using TD-DFT in combination with implicit solvation methods, outlined in the experimental section, to reveal the nature of excitation and relaxation processes and to elucidate structure–optical property relationships, shedding light on the fundamental trends in the recorded experimental data summarized in the section Optical properties. To discuss the findings intuitively, the studied molecules were grouped into three families defined by the HC linker. Namely, (i) Family **1** groups molecules in which the donor and acceptor groups are tethered by a phenylacetylene linker (**1**), (ii) in Family **2**, the bridging group is a phenyl linker (**2**), and (iii) **FDDNP** together with **DDNP** constitutes Family **3** with a naphthalene linker.

Let us start the analysis with **FDDNP** and **DDNP**. Our simulations revealed a characteristic photoexcitation process, termed twisted intramolecular charge transfer (TICT), for these two entities. TICT constitutes several key elements, including (i) a planar or quasi-planar ground state, (ii) a twisted excited state, and both (iii) an oxidant (donor) and (iv) a reductant (acceptor) functionality in a molecule, separated by an inert spacer.

As supported by a molecular orbital and a charge analysis (vide infra), the donor group loses an electron (reductant), and the acceptor moiety gains this electron (oxidant) in the photoexcitation of the studied fluorophores defining an intramolecular charge-transfer excitation. The separated formally cationic EDG<sup>+</sup> and anionic EWG<sup>−</sup> poles give rise to a super polar excited state corresponding to the  $S_0 \rightarrow S_1$  transition. This charge separation makes the excited state of

these fluorophores a sensitive probe for the local media, fingerprint electrostatics of protein surfaces, and cavities. This information is coded into the energy of the emitted photon when  $S_1$  decays radiatively to  $S_0$ . The rod-like skeleton of the studied fluorophores is not completely rigid as the rotation of the EWG, EDG, and HC spacer groups is free along the connecting single bonds. These groups are quasi-coplanar in the ground state, as revealed by the computed equilibrium structures (Figures 3.2–3.4) of the studied fluorophores. The names/labels given to molecules are also provided in the same figures.

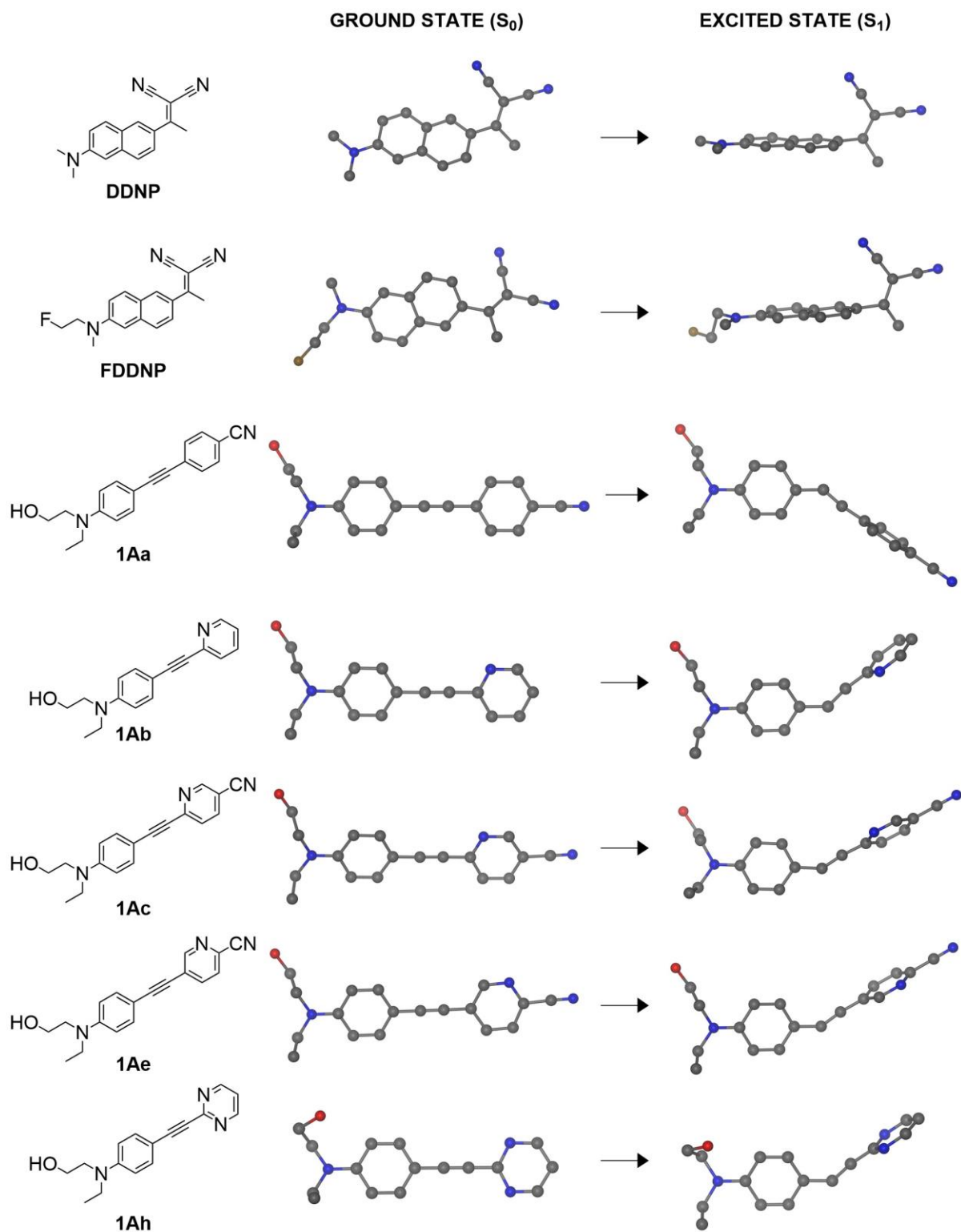


Figure 3.2: Equilibrium structures of the ground ( $S_0$ ) and excited state ( $S_1$ ) species of the molecular probes **DDNP** – **1Ah** considered in this study.

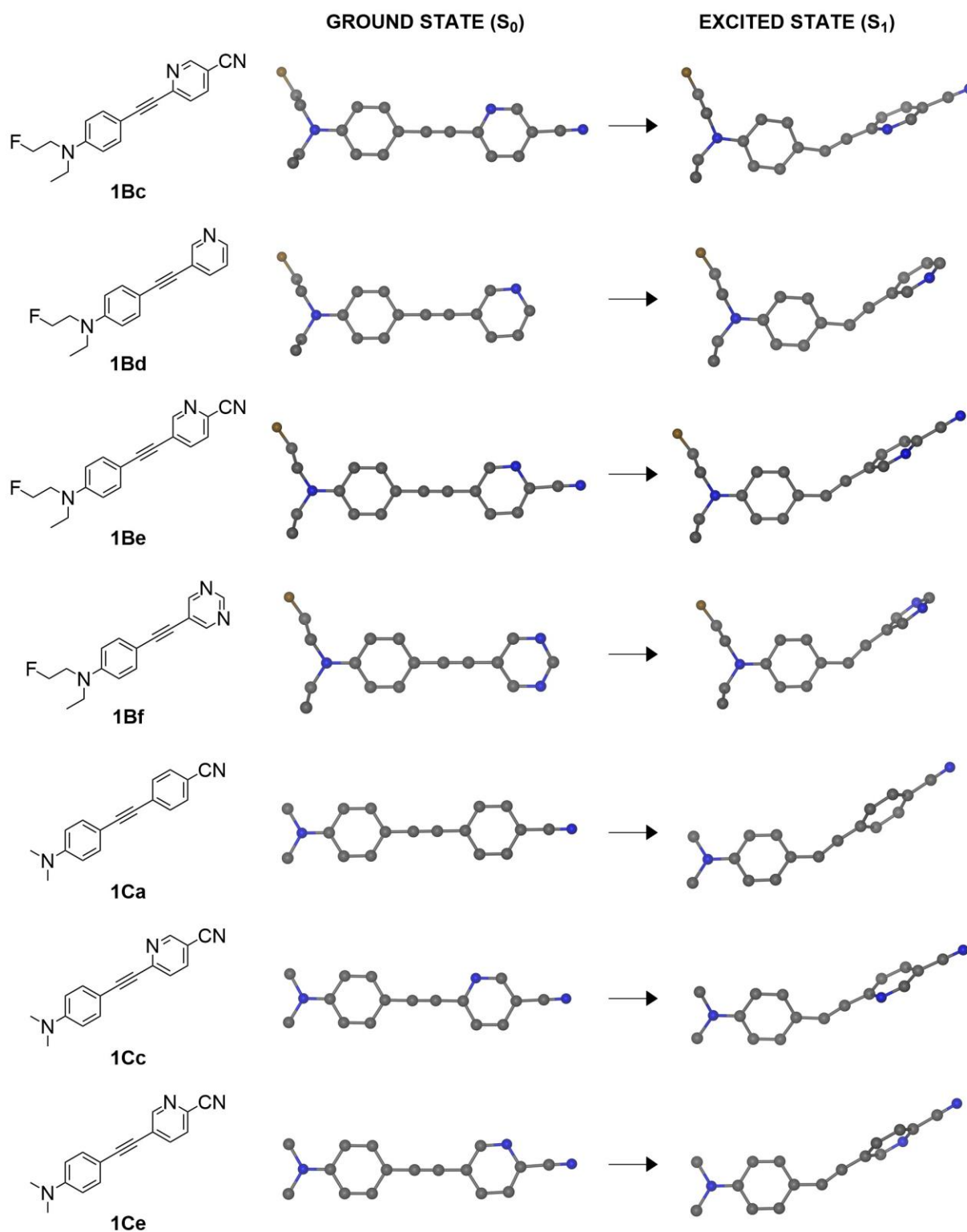


Figure 3.3: Equilibrium structures of the ground ( $S_0$ ) and excited state ( $S_1$ ) species of the molecular probes **1Bc** – **1Ce** considered in this study.

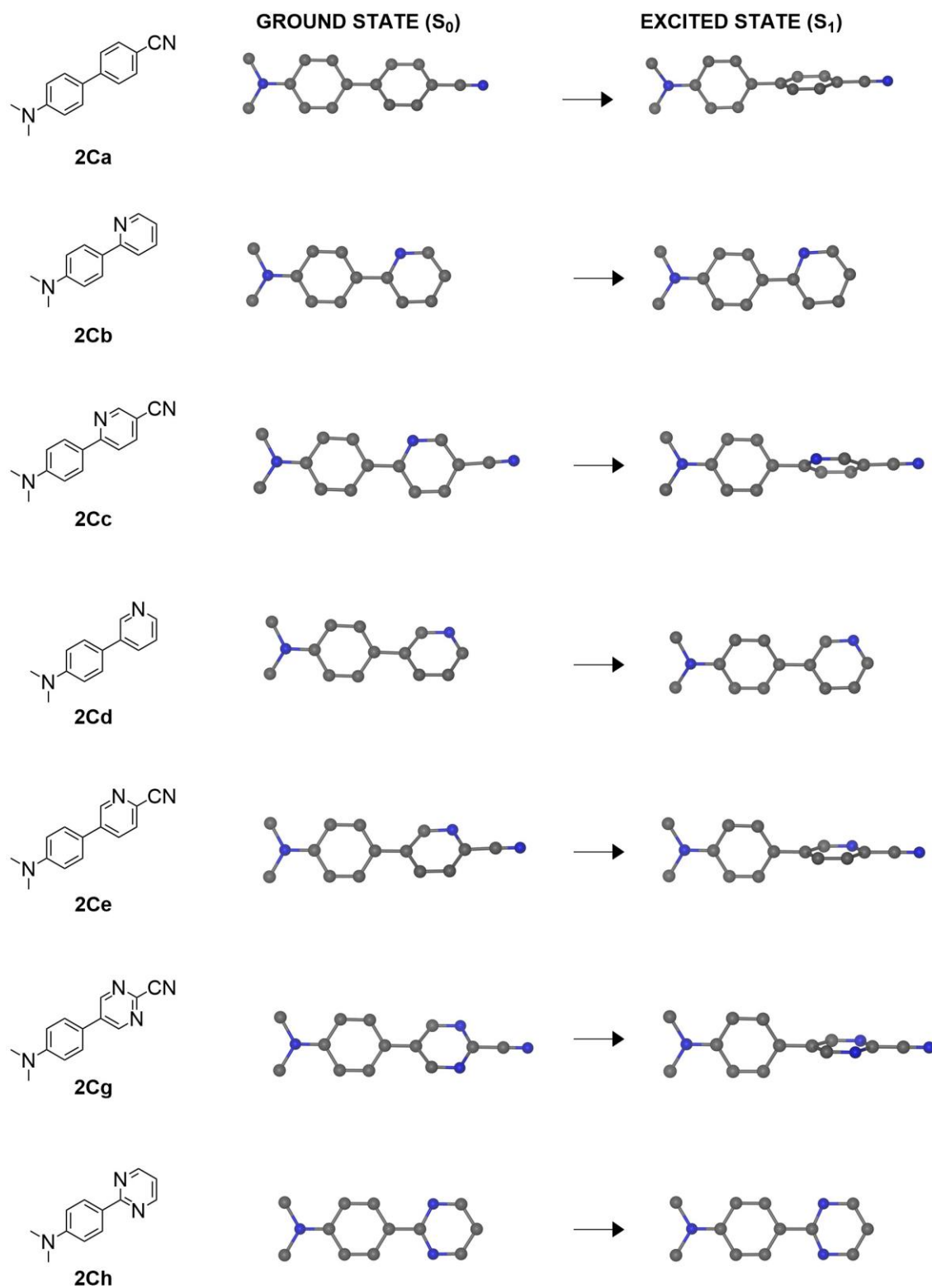


Figure 3.4: Equilibrium structures of the ground ( $S_0$ ) and excited state ( $S_1$ ) species of the molecular probes **2Ca** – **2Ch** considered in this study.

Figure 3.5 showcases this change in the relative orientation of donor and acceptor planes in the ground- and excited state equilibrium structures of **DDNP**, **1Ab**, **2Cd**, and **2Cg**, which are representative species of the corresponding Family 3, Family 1, Family 2, respectively. For example, the dihedral angle between the donor and acceptor groups ( $\alpha$ ) is  $34.9^\circ$  in the  $S_0$  ground state of DDNP, indicating a quasi-planar structure, which, however, twists to  $\alpha = 99.4^\circ$  in the  $S_1$  excited state. This quasi-perpendicular orientation of the planes of the charged groups ( $\text{EWG}^-/\text{EDG}^+$ ) is the key to bringing about a TICT excited state in which the spacer remains co-planar either with  $\text{EWG}^-$  or  $\text{EDG}^+$ .

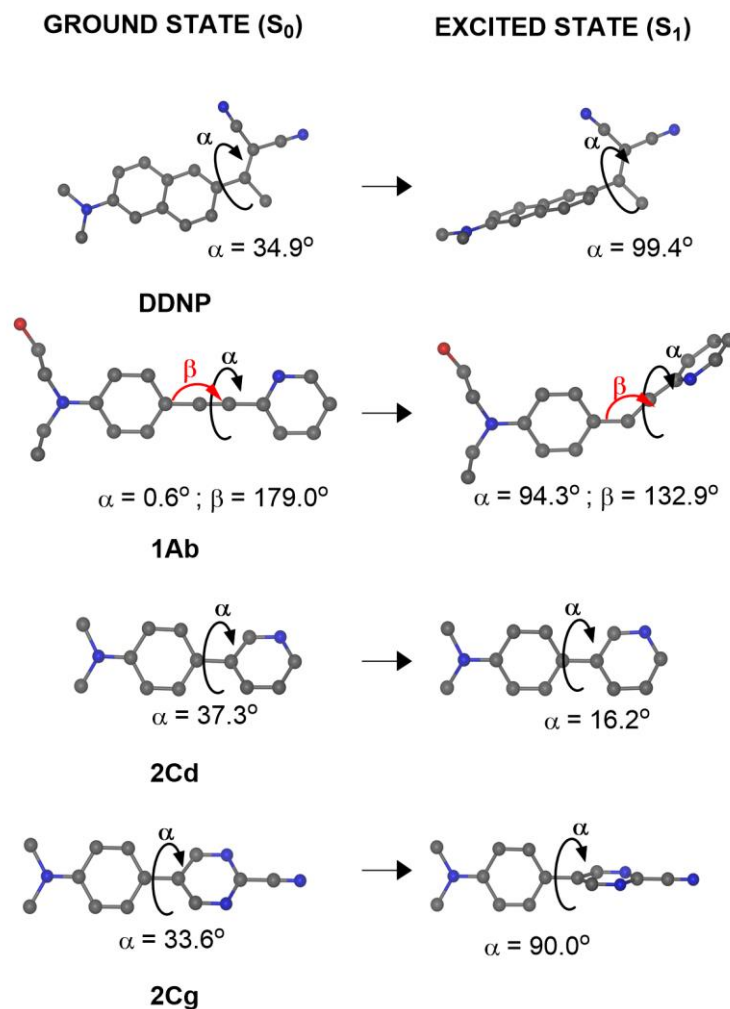


Figure 3.5: Equilibrium structures of the ground ( $S_0$ ) and excited state ( $S_1$ ) species of **DDNP**, **1Ab**, **2Cd**, and **2Cg**.

In addition, our scans of the potential energy surfaces (Figure 3.6) along the dihedral angles corresponding to the rotation of these groups give estimations for the rotational activation barriers in the range of 5–9 kcal mol<sup>-1</sup> in the ground state, implying free rotation at room temperatures.<sup>92</sup>

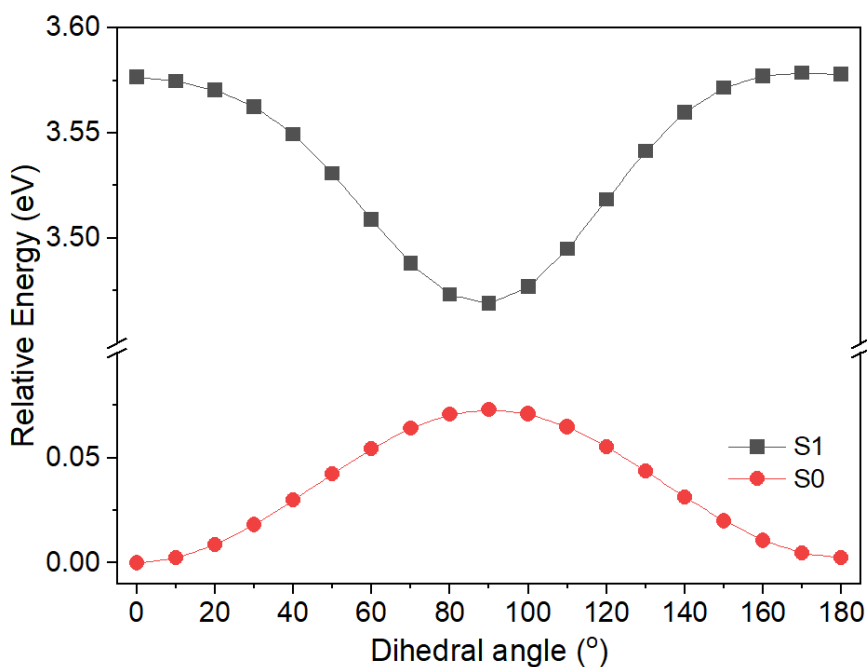


Figure 3.6: Dependency of the relative energy with the dihedral angle of **1Ab** calculated in the gas phase.

The  $S_0 \rightarrow S_1$  excitation of all the studied fluorophores is of HOMO-LUMO character dominantly, describing ca. 70% of the overall electronic structure change due to photon absorption, with minor contributions from several other occupied-virtual orbital pair transitions. As Figure 3.7 shows, while HOMO has a delocalized nature with large wavefunction amplitude at the donor group (31% for **DDNP**), representing the lone pair at the nitrogen of amine and  $\pi$ -orbitals of the aromatic bridge (59% for **DDNP**), it is mainly confined to the latter two groups without much delocalization to the acceptor pole. In contrast, the LUMO is characteristically confined to the acceptor group and is of  $\pi^*$  character (66% for **DDNP**). Thus, the promotion of an electron from



HOMO to LUMO in the  $S_0 \rightarrow S_1$  transition transfers an electron from the donor pole to the acceptor pole of the molecule.

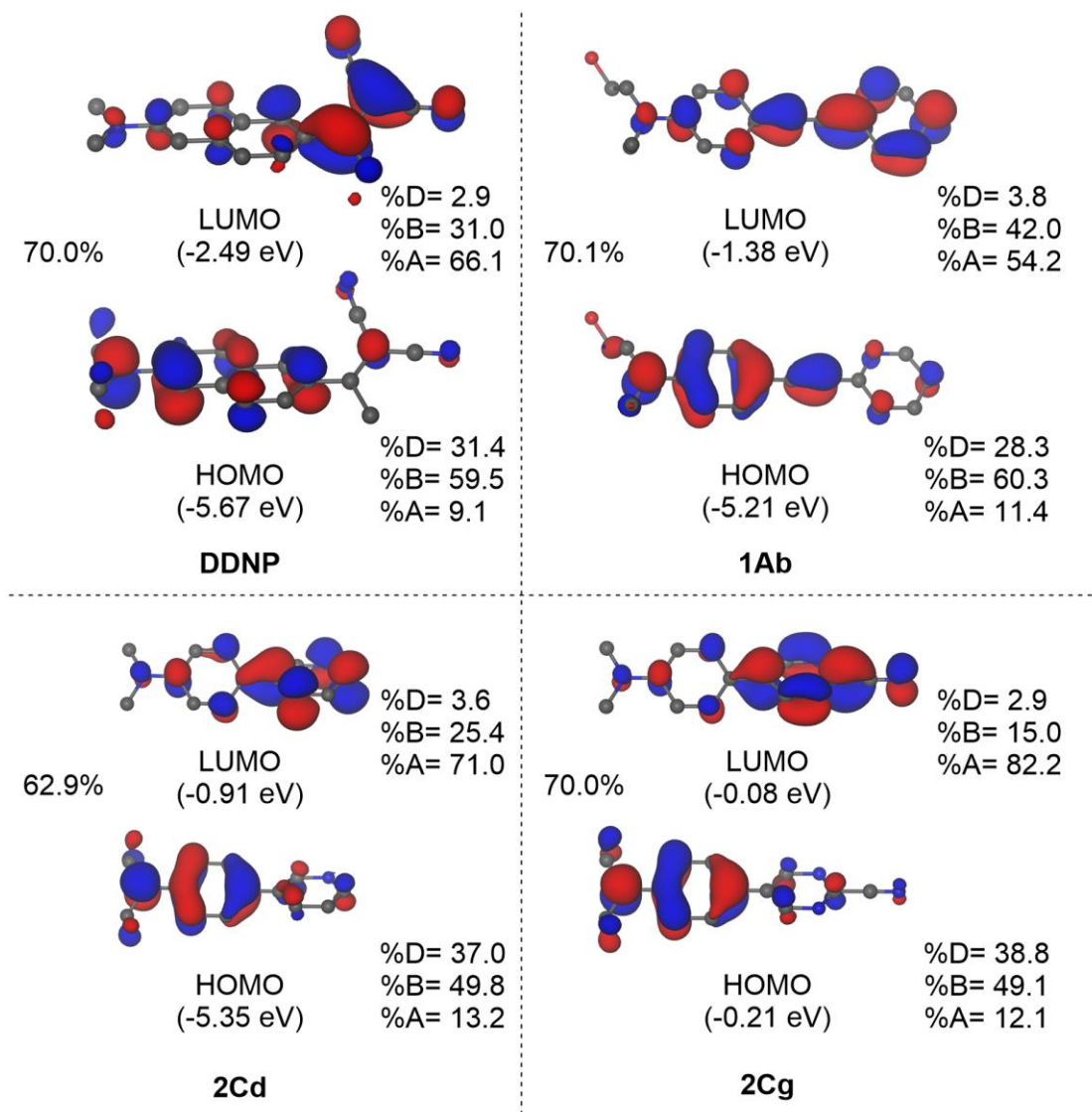


Figure 3.7: Frontier HOMO and LUMO orbitals for DDNP, 1Ab, 2Cd and 2Cg. The computed weight of the HOMO  $\rightarrow$  LUMO transition to the  $S_0 \rightarrow S_1$  vertical excitation upon photon absorption is provided. Orbital composition analysis based on the Mulliken partition. D: donor (EDG), B: bridge (HC linker), A: acceptor (EWG) group.

This charge transfer can also be witnessed in the electron density change in the excitation (Figure 3.8): electron density accumulates at the acceptor group (yellow lobes), whereas it depletes at the donor group (purple lobes), including the bridge, to some extent.

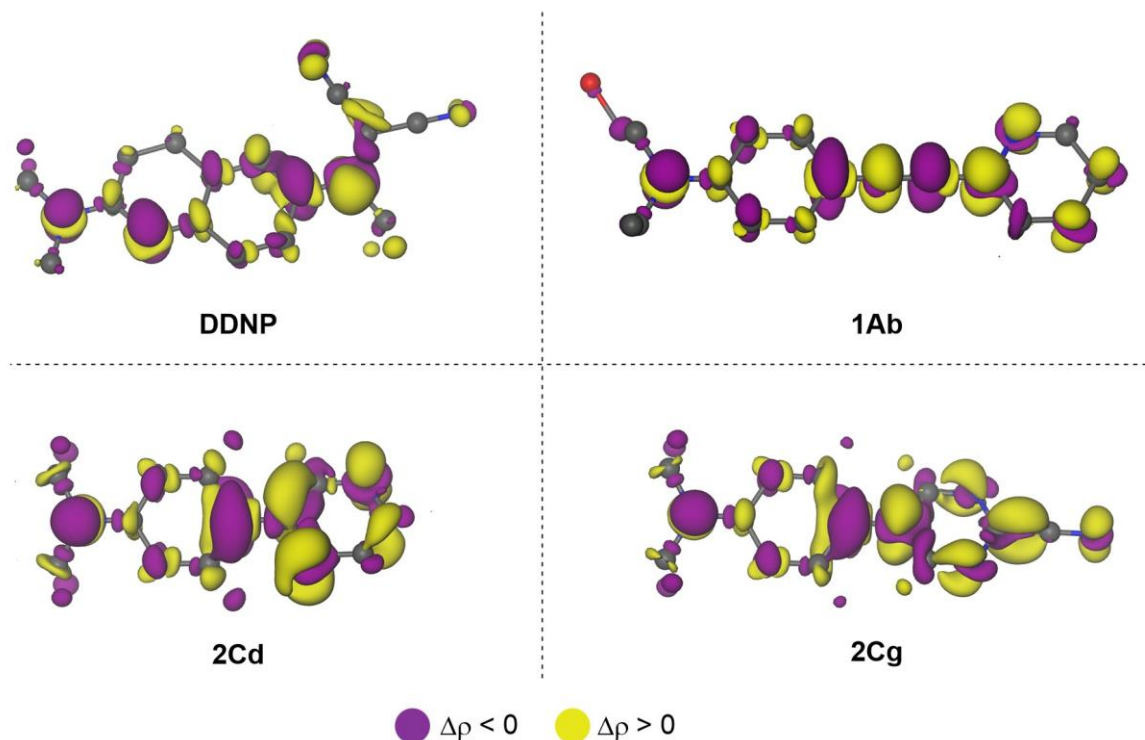


Figure 3.8: Electron density difference change ( $\Delta\delta$ ) for the  $S_0 \rightarrow S_1$  transition of **DDNP**, **1Ab**, **2Cd**, and **2Cg**.

Atomic charges computed in the ground and excited states (Table 3.2) corroborate and estimate this significant electron density shift from donor to acceptor due to the excitation. The slightly polar donor and bridge functionalities ( $q = \sim 0.1$  e) and somewhat negative acceptor poles ( $q = -0.1$  to  $-0.2$  e) substantiate the polar nature of the ground state of these species. The charge separation is significantly more pronounced in the  $S_1$  excited state of these molecules, showcased by charges, e.g.,  $-0.81$  e and  $0.29$  e and  $0.52$  e at the acceptor, donor, and bridge, respectively, in the case of **DDNP**.

Because of the twisting of the molecular structure and the electron transfer from the donor to the acceptor group in the photoexcitation, the polar excited state is termed the twisted intramolecular charge transfer (TICT) state. TICT has a marginal role in the vast library of photochemistry of molecules. Nevertheless, its potential for selective molecular recognition via

fluorescent spectroscopy has been recognized recently. On the other hand, TICT is one of the key elements of dual fluorescence, a unique phenomenon that Grabowski scrutinized in the 70's–90's.<sup>93</sup>

Table 3.2: Functional group-condensed charges in the ground ( $S_0$ ) and excited ( $S_1$ ) states obtained for **DDNP**, **1Ab**, **2Cd**, and **2Cg** using Mulliken analysis.

Ground state ( $S_0$ )					Excited State ( $S_1$ )			
Molecule	DDNP	1Ab	2Cd	2Cg	DDNP	1Ab	2Cd	2Cg
Donor (EDG)	0.10	0.11	0.06	0.10	0.29	0.28	0.26	0.34
Bridge (HC linker)	0.11	0.02	0.02	0.06	0.52	0.13	0.22	0.39
Acceptor (EWG)	−0.21	−0.13	−0.08	−0.16	−0.81	−0.41	−0.47	−0.73

Because of the latter studies, TICTs are relatively well understood. Most importantly, although (i) the radiative decay from the TICT state to the ground state is quantum-mechanically forbidden, low energy asymmetric vibrations in the excited state give rise to weak fluorescence, and (ii) the lack of fluorescence in water is due to H $\cdots$ lone pair (e.g., at the donor) interactions that quench TICT excited state effectively, structure–optical property relationships and a rationale for the environment dependent Stokes shift and solvatochromism were also put forward.

Consistent with the implications of (i), Figure 3.9 shows that the oscillator strength ( $f_{osc}$ ) decreases radically with the increase of the dihedral angle  $\alpha$  and indeed reaches near zero values at 80–90° for **DDNP**, **FDDNP** and most species studied. As mentioned, a low quantum yield of fluorescence is nevertheless observed due to the anharmonicity of the low-energy molecular vibrations. As a handful of studies have shown, stiffer molecular scaffolds and appropriate steric effects that confine the excited state to a more planar geometry are effective measures to increase emission efficiency, i.e., quantum yield.

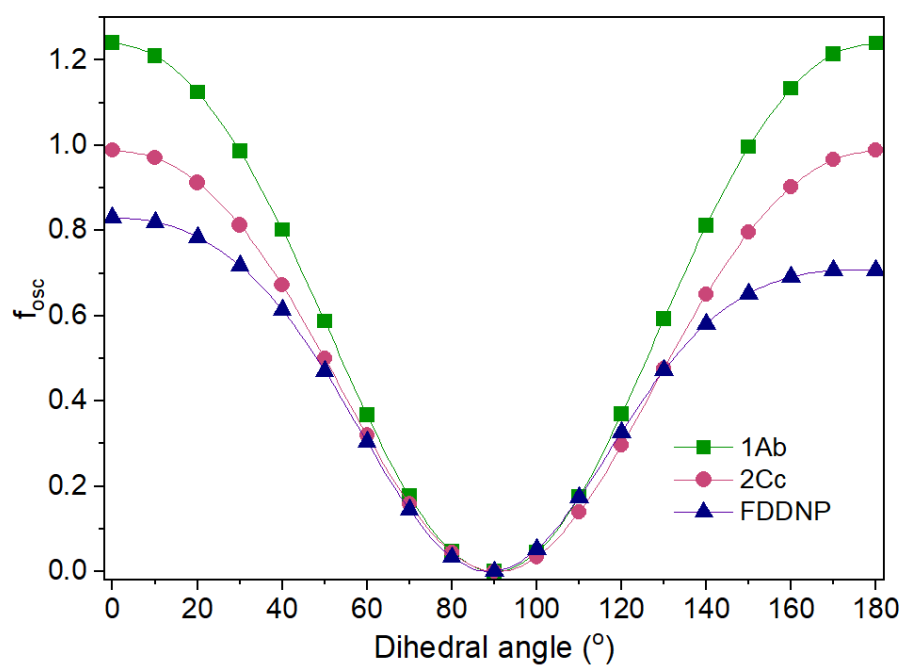


Figure 3.9: The dependency of the oscillator strength with the dihedral angle for molecular probes **1Ab**, **2Cc**, and **FDDNP** calculated in DCM.

Figure 3.10 outlines a schematic rationale for the particularly environment-dependent fluorescence of molecules with TICT or PICT (planar intramolecular charge transfer) excited states. Although the ground state of these molecules is already polar, as demonstrated by the computed charge distributions and dipole moments (Table 3.3), e.g., 10.0 Debye for **2Ce**, the TICT excited state is significantly more polar, 28.9 Debye, given the charged separation discussed above. As can be seen in Figure 3.11, dipole moments in average triplicate their value when being in the excited state ( $S_1$ ) when comparing with it in the ground state ( $S_0$ ).

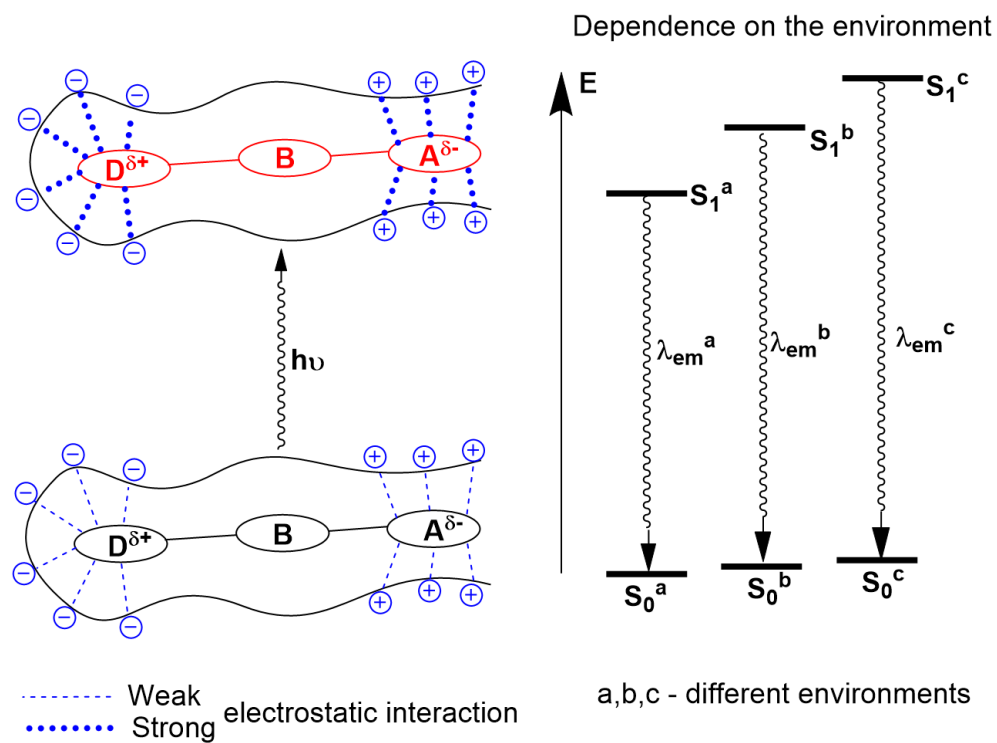


Figure 3.10: Schematic representation of the environment-dependent fluorescence in the excited state. D: donor (EDG), B: bridge (HC linker), A: acceptor (EWG) group.

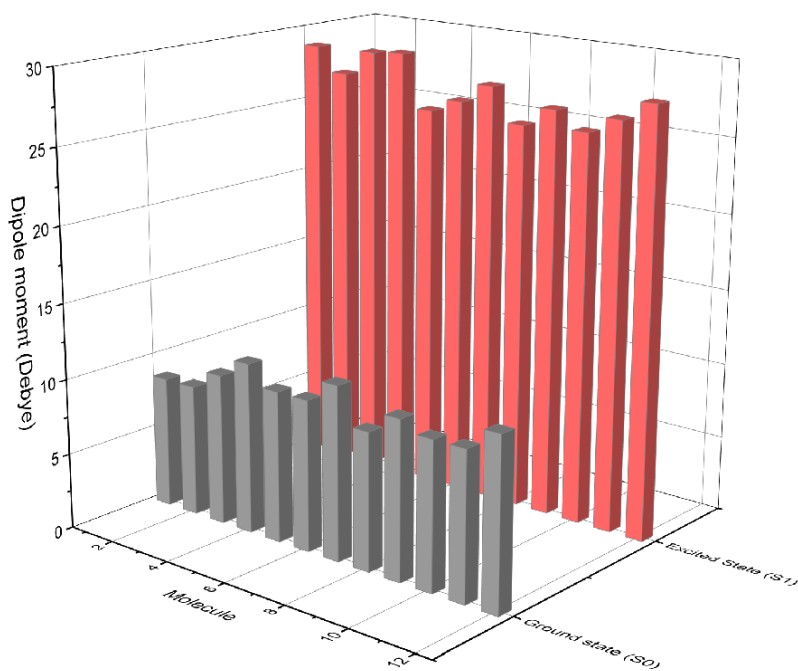


Figure 3.11: Change on the dipole moment when going for the ground ( $S_0$ ) to the excited state ( $S_1$ )

Table 3.3: Dipole moments in the ground and excited state (Debye) B3LYP/cc-PVTZ level of theory

MOLECULE	Ground state	Excited state
<b>DDNP</b>	10.3	26.5
<b>FDDNP</b>	9.0	24.9
<b>1Aa</b>	9.8	25.8
<b>1Ab</b>	3.8	16.6
<b>1Ac</b>	9.8	26.9
<b>1Ae</b>	11.3	28.2
<b>1Ah</b>	4.8	18.7
<b>1Bc</b>	9.1	25.6
<b>1Bd</b>	5.2	16.4
<b>1Be</b>	10.5	26.9
<b>1Bf</b>	5.9	17.9
<b>1Ca</b>	10.0	25.6
<b>1Cc</b>	10.0	26.5
<b>1Ce</b>	11.5	27.8
<b>2Ca</b>	8.7	28.8
<b>2Cb</b>	2.5	14.1
<b>2Cc</b>	8.7	27.2
<b>2Cd</b>	4.5	14.9
<b>2Ce</b>	10.0	28.9
<b>2Cg</b>	11.3	29.1
<b>2Ch</b>	1.81	15.8

Accordingly, in any polar environment, either these molecules develop relatively strong electrostatic interactions, together with other non-covalent interactions, including H-bonding and

$\pi$ - $\pi$  stacking, with the environment, polar solvent molecules, or protein's amino acid residues, already in the resting ground state, which was also revealed by molecular docking. Since absorption is instantaneous and the electronic and structural relaxation is faster than diffusion, the super-polar TICT state finds itself in the same molecular environment as the ground state. Due to the super-polar nature of the TICT state, the probe-environment electrostatic attractions become significantly stronger in the excited state, stabilizing the  $S_1$  state with respect to the  $S_0$  ground state. Different local environments result in different stabilizations of the TICT state (Figure 3.10, right), with the energy of the photon emitted by the probe also turning out to be different and characteristic of the environment that can be used as a diagnostic signal. Together with the twisting of the geometry that also lowers the  $S_0 - S_1$  gap (see Figure 3.5), this stabilization of the TICT state leads to the considerable Stokes shifts observed experimentally.

This basic photophysics is somewhat perturbed by the nature of the bridge group, which can be summarized as follows: (i) In addition to twisting, there is a characteristic bending of phenylacetylene linker 1 in the  $S_1$  excited state of all species of Family 1 (see Figures 3.2–3.4), (ii) In the case of the shorter phenyl bridge 2 (Family 2), no twisting takes place in the  $S_1$  excited state when the acceptor group is weak, which can be seen for **2Cd** in Figure 3. Molecules that remain planar in the  $S_1$  excited state include **2Cb**, **2Cd**, and **2Ch** (Figure 3.4), i.e., 2C analogs without strong  $\pi$ -withdrawing nitrile on the acceptor side.

The charge transfer nature of the  $S_0 \rightarrow S_1$  excitation is unambiguous in all cases, witnessed by the topology of the frontier HOMO-LUMO orbitals and by the characteristics of the electron density difference maps (Figure 3.7 and Figure 3.8). The bending of the excited state of the Family 1 species, as twisting does not allow  $\pi$ -delocalization between acceptor and donor groups, can be intuitively rationalized by a carbanion character at  $C_\alpha$  of the acetylene group leading to  $sp^2$

hybridization and bending at  $C_\alpha$ . Indeed, there is a significant amplitude of LUMO at  $C_\alpha$  in **1Ab**, i.e., a significant charge will be shifted to this carbon during the excitation process, as demonstrated by the  $\Delta\rho$  ( $S_0 \rightarrow S_1$ ) distribution of **1Ab**. Similar bending along the axis of the molecule was also considered as a potential key motif in the dual fluorescence of 4-(N,N-dimethylamino)benzonitrile (DMABN), and the corresponding state was termed rehybridized ICT (RICT state).<sup>41</sup> A recent ab initio study indeed demonstrated RICT in the quenching dynamics even in small molecules like DMABN,<sup>94</sup> whereas it has a significant role in the photophysics of phenylethynyl-benzene type molecules.<sup>42</sup> The origin of the planarity of the  $S_1$  state of some of the Family **2** species is less obvious; the  $S_0 \rightarrow S_1$  transition plausibly has a larger local excitation (LE) character in these cases stemming from the involvement of bridge  $\pi$ -orbitals in both HOMO and LUMO. For example, LUMO has a 25% bridge contribution in **2Cd**, which stays planar in the  $S_1$  state, whereas the LUMO of **2Cg** delocalizes less to the bridge (15%), indicating a more prominent charge transfer character that results in the twisting of the molecule in the  $S_1$  state.

Admittedly, TD-DFT is notoriously weak in reproducing absorption energies for charge transfer excitations, even when using the most advanced approximations for electron exchange and correlation, i.e., advanced functionals. A recent benchmark study by Mester and Kallay<sup>95</sup> reported an average deviation of 0.23 eV between computed and experimental absorption energies for the charge transfer excitation absorption of 326 singlet excitations. The latter ‘best’ result was achieved with the theoretically most suitable range-separated DSD-PBEP86 functional. In line with this finding, our methodology based on the M062X functional and cc-PVTZ basis set combination overestimates absorption energy by 0.28 eV on average with respect to experimental values for the 21 studied fluorophores. The direct correlation ( $r^2 = 0.96$ ) between measured and computed absorption energies in DCM (Figure 3.12) and other solvents (methanol in Figure 3.13,



acetonitrile in Figure 3.14, and hexane in Figure 3.15) nevertheless ensures the qualitative use of density functional theory. This implies that our simulations identify the correct excitation and capture the underlying electronic structure changes to a sufficient extent. We would like to note that the experimentally measured absorption energies were obtained by the Košmrlj group. The following sections discuss the trends in the computed absorption energies and the measured optical properties.

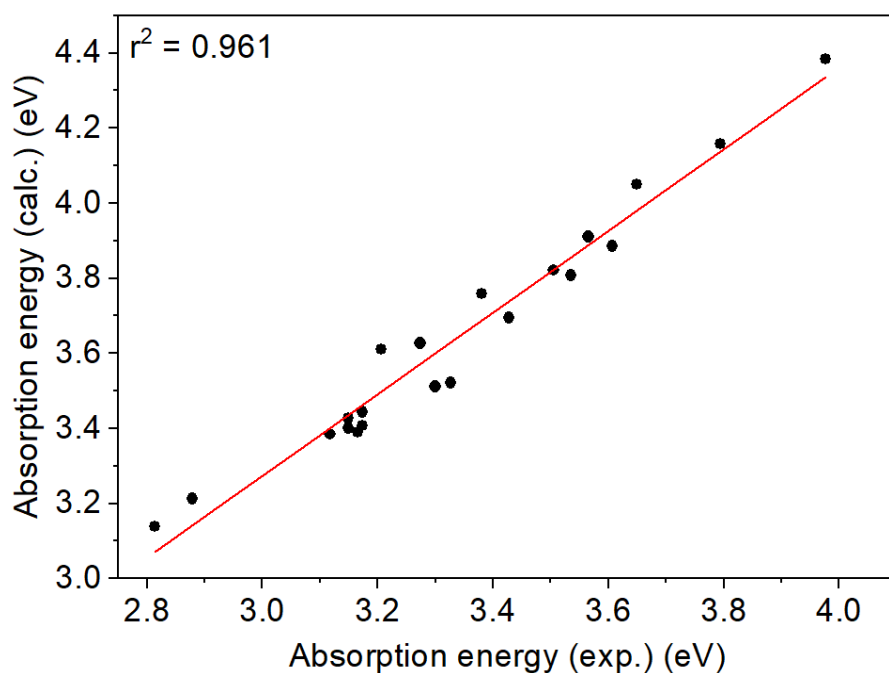


Figure 3.12: Linear correlation between computed and experimental absorption energies in dichloromethane (DCM) (eV)

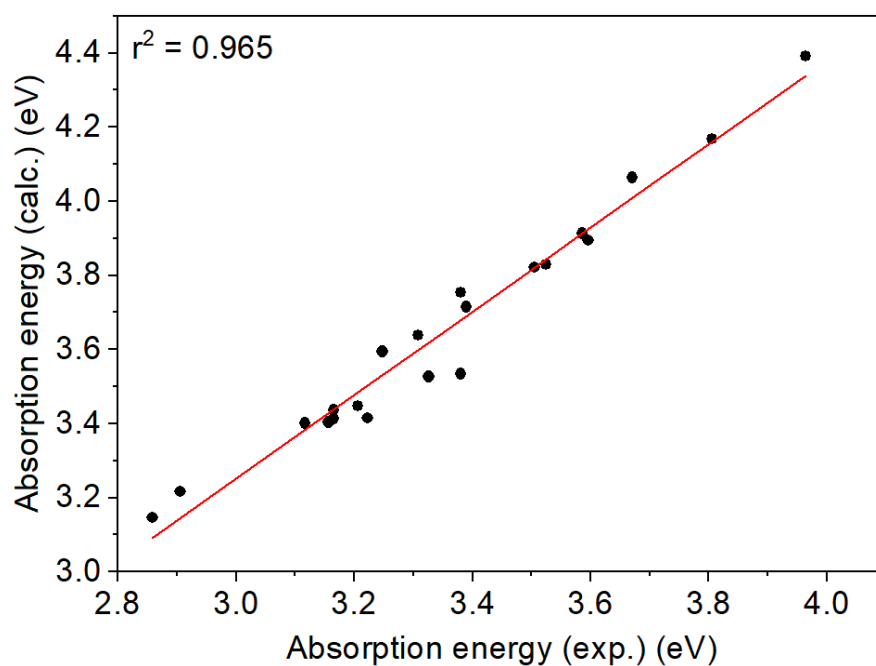


Figure 3.13: Linear correlation between computed and experimental absorption energies in methanol (MeOH) (eV)

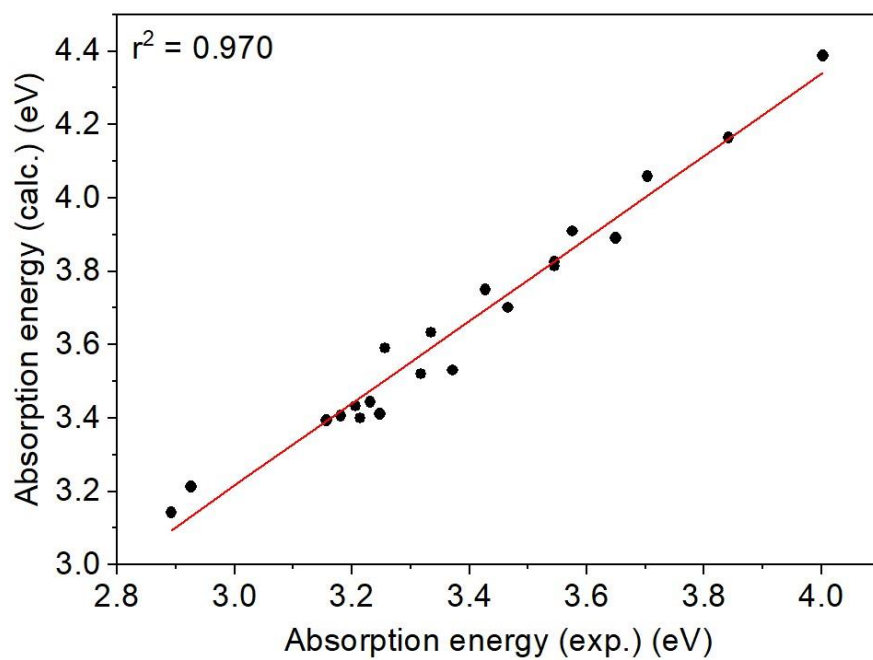


Figure 3.14: Linear correlation between computed and experimental absorption energies in acetonitrile (MeCN) (eV)

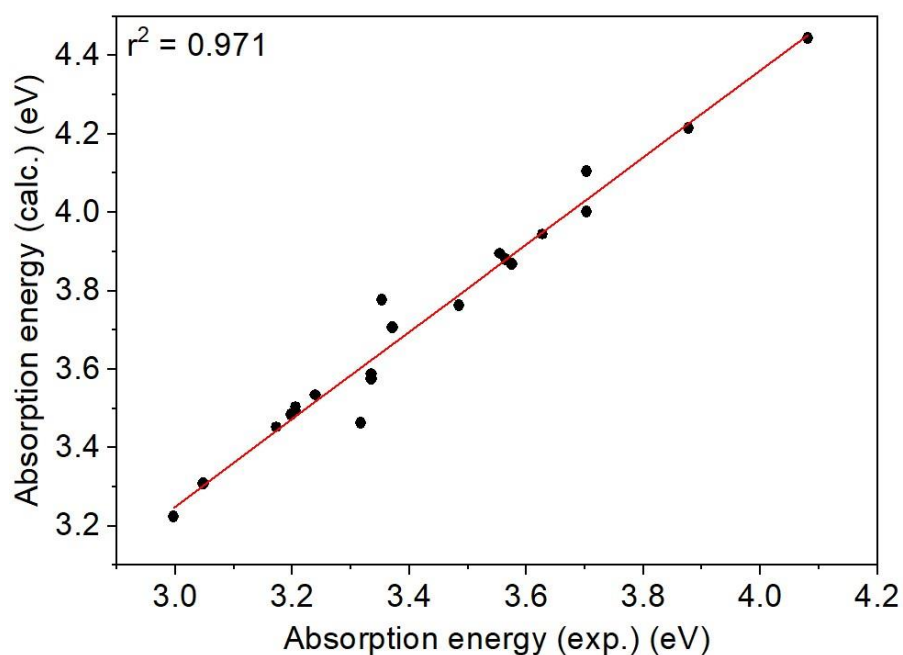


Figure 3.15: Linear correlation between computed and experimental absorption energies in Hexane (eV)

### 3.4 CONCLUSIONS

For a deeper understanding of the relationship between structure and optical properties, the photophysics of the dyes was studied by TD-DFT in combination with implicit solvation methods, which revealed twisted/planar intramolecular charge transfer excitations. The underlying electronic transitions are HOMO-LUMO in nature and the TICT  $S_1$  excited state has superior environment detection properties due to its high polarity. A convincing direct correlation between the measured and calculated absorption energies indicated the realistic capture of the underlying electronic structural changes. Our computational studies, together with the experimental studies of our collaborators (Košmrlj group), have been submitted for publication in a peer-reviewed journal.

## **Chapter 4: Photophysics of molecular probes for Amyloid- $\beta$ detection: computational insights into roles of probe linker and functional groups**

### **4.1 INTRODUCTION**

According to the National Institute on Aging at the National Institutes of Health, Alzheimer's disease (AD) will soon affect over one-third of the population over the age of 65<sup>96</sup>. Innovating an inexpensive, generally available, and less-invasive protocol for the early diagnosis of AD will profoundly impact the future of millions of people worldwide. AD is a neurodegenerative tauopathy and the most common cause of dementia, characterized by two significant pathologic lesions, deposits of amyloid  $\beta$  ( $A\beta$ ) plaques and neurofibrillary tangles, presented as deposits of abnormal brain proteins that cause synaptic loss and neurotoxicity.<sup>97-99</sup>

Studies suggest that Alzheimer's disease begins years before the first symptoms appear.<sup>100</sup> Nevertheless, timely treatment of the disease has not been possible since reliable and affordable diagnostic tools to identify it at an early stage are still under development, and the damage caused by AD on the brain is irreversible.<sup>6</sup> To date, there is still a lack of effective treatments and only limited options to fight against the symptoms that are manifested at late stages.

The pathological changes due to AD show up both in the brain and its peripheries. There is a direct correlation between disease progression and the levels of  $A\beta$  aggregates and various forms of Tau protein in cerebrospinal fluid (CSF) and blood, such as phosphorylated Tau (p-Tau), non-phosphorylated Tau (n-Tau), total Tau (t-Tau) and truncated Tau.<sup>101-104</sup> These proteins and aggregates can serve as biomarkers to monitor the beginning and progression of the disease outside the central nervous system.<sup>105</sup> For example, these biomarkers could be measured in an alternative way other than the existing *in vivo* molecular imaging techniques, such as Positron Emission Tomography (PET), Magnetic Resonance Imaging (MRI), and Single Photon Emission Computed

Tomography (SPECT).<sup>17</sup> Body fluid-based analysis of the biomarkers would decrease the need for specialized and expensive equipment, short-lived unstable (radio)isotopes, and patient-unfriendly procedures, recognized as the limitations of the above *in vivo* techniques.<sup>106</sup>

Targeting A $\beta$  aggregates in the blood is an intricate task due to the low resolution (viz. femtomolar concentrations of A $\beta$  aggregates in the blood) and the high price of antibody-based detection methods currently used to diagnose AD.<sup>107,108</sup> However, small molecules can be designed to recognize and bind to a defined sequence of amino acids or specific environments on surfaces of target proteins and serve as sensors of those protein targets. If appropriately designed, such small molecules could show marker-specific fluorescence when interacting with the target, making the targets visible, thus offering a faster and cheaper representation of biomarker abundance for blood-based diagnosis of AD.

Fluorescent molecular probes are interesting in diagnostic applications due to their high sensitivity to the local environment. For molecular probes with a Donor-Bridge-Acceptor (D-B-A) rod-like structure, this sensitivity can be attributed to the polarity increase in the excited state, as shown in Figure 4.1a, promoting stronger electrostatic interactions with polar solvent molecules or protein residues. Increased interactions will stabilize the excited state, with their effects depending on and being characteristic of the local environment. These specific marker-probe interactions directly influence the energy of the emitted photon that could be used as a diagnosis signal.

Recent studies<sup>27</sup> (Figure 4.1b) have demonstrated the promising capabilities of some derivatives of 2-(1-{6-[(2-Fluoroethyl)(methyl)amino]-2-naphthyl}ethylidene)malononitrile (FDDNP) to detect A $\beta$  plaques and p-Tau tangles using fluorescence microscopy in treated and inspected slices of human brain tissue. Molecular probes based on FDDNP structure, featuring

fixed donor and acceptor groups but with variable linkers, were synthesized and examined for their ability to detect Tau protein deposits *in vitro*<sup>27</sup>.

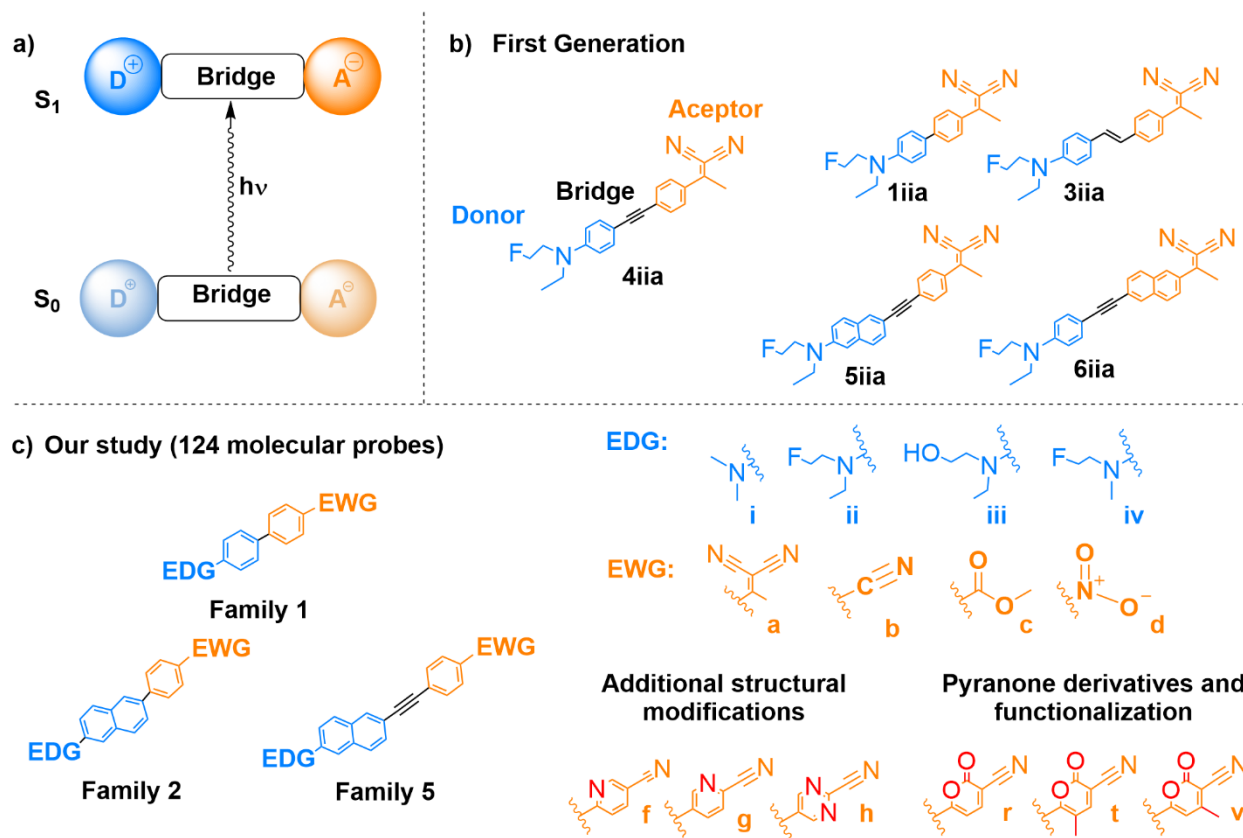


Figure 4.1: a) Schematic representation of DBA fluorophores, b) First generation of molecular probes that detected Amyloid  $\beta$  plaques and p-Tau tangles, c) Example of families, additional structural modifications, pyranone derivatives and their functionalization considered in this study

This study showed that probes with biphenyl and diphenylacetylene fragments can successfully differentiate p-Tau neurofibrillary tangles from amyloid  $\beta$  aggregates. The differentiation is based on the probes' maxima emission wavelengths; however, further refinement is required to improve the selectivity and specificity of these probes. Following this experimental study, more molecular probes with the two previously examined linkers but with different donor and acceptor groups were synthesized and experimentally examined (unpublished work) and

demonstrated the importance of having a clear understanding of the roles played by each molecular fragment on the photophysical properties.

Following the insights offered by the above studies, in this chapter, the molecular and electronic structures in the ground and excited states of an extended set of D-B-A-like molecules formed by six families of molecular probes are characterized (Figure 4.1c). Using DFT and TD-DFT calculations, our work provides a better understanding of the behavior of the new molecular probes after the excitation process is carried out via light absorption. Furthermore, our present work establishes a rational understanding of the intricate relationship between molecular structure and photophysical properties, with a particular focus on absorption energy. Through systematic analysis, design principles for these molecular probes will be elucidated, facilitating a rational approach to optimizing the donor, acceptor, and bridge, accounting for their influence over the absorption energy. Additionally, we used the calculated absorption energies to train machine learning (ML) models on probe structures used as the input, and their absorption energies were set as the predicted output. This research forms the basis for discovering new molecular probes that will allow the detection of AD biomarkers *ex vivo* in bodily fluids, guided by a deeper understanding of their structure-dependent photophysical characteristics.

## **4.2 COMPUTATIONAL METHODS**

### **4.2.1 Quantum Calculations**

In this study, we computationally investigated 138 molecular probes, proposed based on the structures of recently developed rod-shaped donor-bridge-acceptor (D-B-A) fluorescent probe molecules<sup>27</sup>, using quantum chemical calculations employing density functional theory (DFT) and time-dependent DFT methods (TD-DFT) as implemented in Gaussian16 revision B.01<sup>52</sup> software.

Ground state geometry optimizations were performed employing *in silico* models of the compounds derived from the parent x-ray structures and constructed using GaussView 6.1.1<sup>91</sup>. The optimizations were carried out in the gas phase using the hybrid functional B3LYP<sup>53–55</sup> coupled with the correlation-consistent triple- $\zeta$  basis set cc-PVTZ<sup>56</sup> at the ultrafine grid. To confirm the convergence of the optimized structures into minimum points on the potential energy surface (PES), analytical vibrational frequency calculations were computed using the same level of theory (B3LYP/cc-PVTZ). The topology and composition of the frontier HOMO and LUMO orbitals generated from the computed gas-phase wave functions at the B3LYP/cc-PVTZ level were analyzed to understand the nature of the charge transfer transitions within the system. Orbital composition analysis was carried out in the Mulliken partition as implemented in Multiwfn<sup>57</sup> software v.3.8, and molecular orbitals were plotted and visualized using VMD 1.9.3.<sup>58</sup>

TD-DFT excited-state geometry optimizations were performed on the optimized ground-state geometries of molecular probes at the B3LYP/cc-PVTZ level to provide additional insights into the structural changes associated with the electronic transitions, charge-transfer events, and excited-state properties of the system. Electron density difference maps (EDDMs) for the  $S_0 \rightarrow S_1$  transitions of the molecular probes were generated by subtracting the electron density of the  $S_0$  state from that of the  $S_1$  state generated at the B3LYP/cc-PVTZ level of theory. Vertical absorption energies were refined through TD-DFT single-point calculations at the global hybrid functional M062X<sup>59</sup> in combination with the cc-PVTZ basis set. The universal implicit solvation model based on the solute electron density (SMD)<sup>60</sup> with the default setup in Gaussian 16 was employed to study the solvent effects in dichloromethane, hexane, acetonitrile, and methanol on absorption energies.



#### 4.2.2 Machine Learning Models

The calculated absorption energies of the designed molecular probes were used to train machine learning (ML) regression models capable of predicting the absorption energies of new probes. The dataset used for training and testing the ML models contained the calculated absorption energies of 324 molecular probes with different donor, bridge, and acceptor groups. The input for training the ML models was based on the chemical structures of the probes, converted to commonly used molecular fingerprints obtained from the RDKit library.<sup>109</sup> The molecular structures of the probes were first encoded into a simplified molecular-input line-entry system (SMILES)<sup>110</sup> using Avogadro 1.2.0<sup>111</sup> software, which was then converted to six different molecular fingerprints in the RDKit library, namely, RDKit (Daylight) fingerprint, Morgan fingerprint, MACCS keys, Avalon fingerprint, AtomPair, and Topological Torsion fingerprints.<sup>112</sup> The final dataset comprising molecular fingerprints of the probes as input and the quantum chemically calculated absorption energies as the predicted value/output were used to train 200 random regression models per model type. Scikit-learn python library<sup>113</sup> was used to train the ML models using the Support Vector Regression (SVR) algorithm with radial basis function kernel (RBF SVR) and linear kernel (Linear SVR). The dataset was split into training and test datasets at a ratio of 80:20. R-squared ( $r^2$  score) was used as the evaluation metric to evaluate the performance of the trained SVR models, defined as:

$$R^2 = 1 - \frac{SSr}{SSm'}$$

Where SSr is the squared sum error of the regression line and SSm' is the squared sum error of the mean line for the data containing the calculated absorption energies and the predicted absorption energies of molecular probes in the testing part of the dataset. A higher value of the  $r^2$  score that approaches the value of 1 signifies a higher prediction quality of the trained SVR models.

## 4.3 RESULTS AND DISCUSSION

### 4.3.1 Studied Structures and Validation of the Computational Protocol

Figure 4.2 shows the general structure, families, donors, acceptors, and functionalization of investigated molecular probes. All species have an overall linear structure made of a linker/bridge (B) that connects an electron donor (D) functionality and an electron acceptor group (A). This rod-like D-B-A structure is key in determining the electronic structure reorganization process triggered by photoexcitation (*vide infra*).<sup>114</sup> The push-pull electron effect was generated like in FDDNP molecule<sup>88</sup> using a rod-like geometry and an extended  $\pi$ -conjugated framework including naphthalene, benzene, ethyne, and ethene building blocks. To streamline the analysis and discussion of the 138 probes studied, we defined six families of molecular probes depending on the type of linker, which correspond to biphenyl (**1**), 2-phenylnaphthalene (**2**), *trans*-stilbene (**3**), diphenylacetylene (**4**), and 2-(phenylethynyl)naphthalene (**5**, **6**). Besides variable linkers, different electron-donating and electron-withdrawing groups were systematically studied in combination with the different families to understand better the effect of the nature and functionalization of donor and acceptor sites. For example, we varied the acceptor and donor strengths of these groups to reveal their manifestations in photophysics, such as the effect on the absorption of energy. Also, the linkers were functionalized with different donors and acceptors in a way to maintain a rod-shaped geometry while altering the distance between donor and acceptor moieties, always maintaining a direct  $\pi$ -conjugation between these functional groups and also torsional flexibility within the molecular framework.<sup>27,88</sup>

The groups considered for the electron-donating side consist of dimethylamine (**i**), N-ethyl-N-(2-fluoroethyl)amino (**ii**), N-ethyl-N-(2-hydroxyethyl)amino (**iii**), and N-methyl-N-(2-fluoroethyl)amino (**iv**). On the other hand, the initial set of electron-acceptor groups consists of

ethylidenemalononitrile (**a**), nitrile (**b**), methoxycarbonyl (**c**), and nitro (**d**) groups. To explore the effect of various structural modifications at the acceptor site, we prepared a second set of functional groups consisting of a CN-substituted benzene ring (**b**), substituted pyridines (**e**, **f**, **h**, **j**), nitro-substituted benzene ring (**d**), and pyrimidine rings (**g**, **k**). Moreover, the effect of pyranone derivatives and their functionalization at the electron-acceptor group was studied using a third set of functional groups examined, including CN-substituted pyran-2-one and pyran-4-one (**o**, **l**), respectively. The influence of a methyl group in electron acceptor groups at both the vicinal to the bridge (**p**, **m**) and more distant (**q**, **n**) positions was also examined.

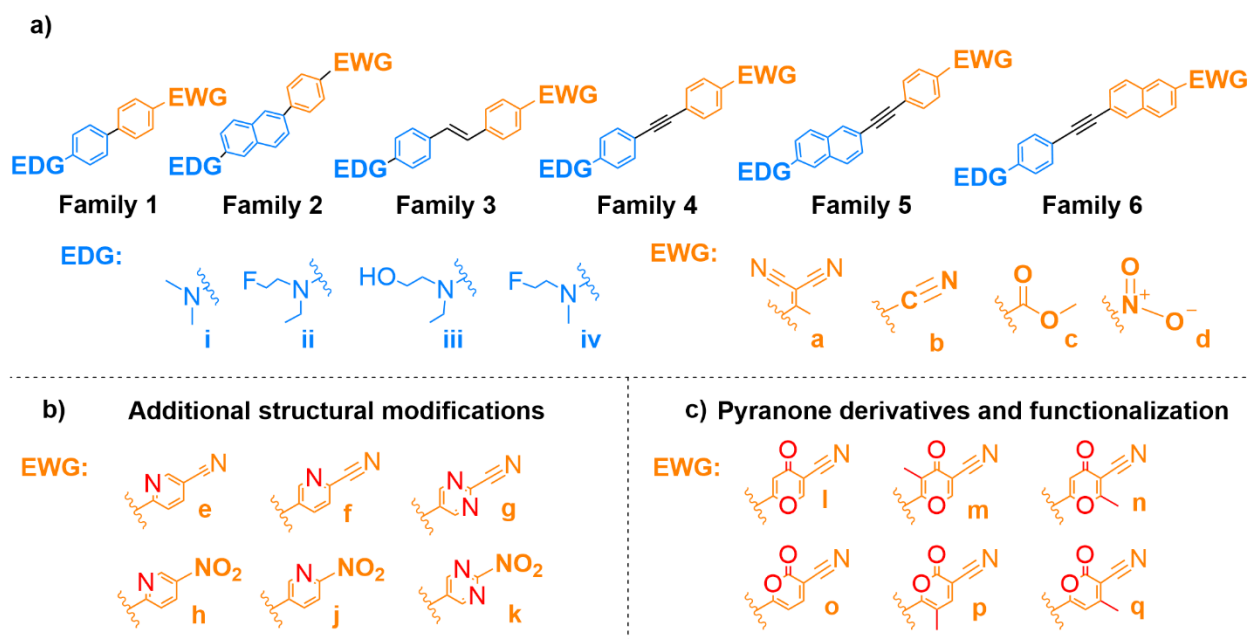


Figure 4.2: a) Definition of the six principal families (**1-6**) of the studied molecular probes given together with the selection of acceptor (A) and donor (D) sets for systematic computational study, b) additional structural modifications studies, and c) pyranone derivatives and their functionalization studied at the acceptor site

To begin with, we first validated a computational protocol using a subset of the investigated molecular probes with the available experimental data. First, we compared the calculated and experimental X-ray structure metrics of molecular probes **4iiif** and **6iia** to assess the accuracy of

our protocol for modeling the equilibrium structures of these species. As shown in Figure 4.3, the empirical X-ray structures were reproduced to a high degree by DFT calculations at the B3LYP/cc-PVTZ level of theory. For example, the central C≡C distances differ from the empirical metrics by about 0.008 Å and 0.014 Å, respectively. Also, C–C, C–N, F–C, and O–C bond lengths are computationally well reproduced with deviations less than 0.02 Å to the X-ray structure.

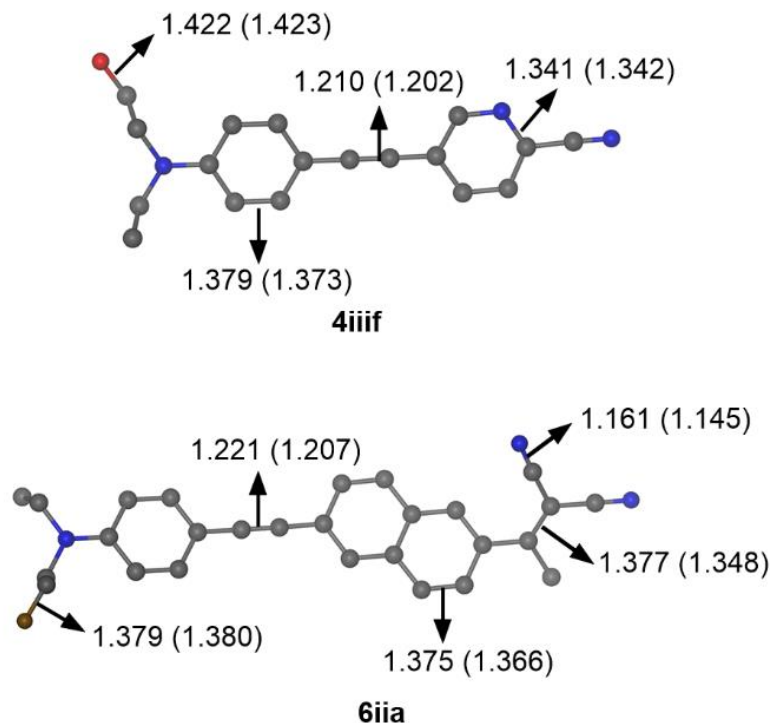


Figure 4.3: Calculated and X-ray structural information of molecules **4iiif** and **6iia**.

With practical *in silico* molecular structures in hand, we aimed to find an advanced (high-rung) DFT functional that can provide realistic excitation energies for these species within the TD-DFT framework. This is not a trivial task as the  $S_0 \rightarrow S_1$  transition involves charge transfer, and TD-DFT is known to struggle with reproducing the energetics of such excitations accurately in general. Our tests on a subset of 28 species, including some of the families in different solvents (See Table 4.1), identified M062X as the most promising functional for computing the excitation energies of the studied 138 molecules.

Table 4.1: Calculated and experimental values of absorption energies (eV) shown in the correlations of Figure 4.5. DCM, hexane, MeCN, and MeOH were used as solvents at the M062X/cc-PVTZ level of theory

Calculated					Experimental			
Molecules	DCM	Hexane	MeOH	MeCN	DCM	Hexane	MeOH	MeCN
<b>1ib</b>	3.910	4.001	3.913	3.909	3.563	3.703	3.583	3.573
<b>1iia</b>	3.258	3.314	3.273	3.271	2.995	3.162	3.039	3.084
<b>3iia</b>	2.896	2.943	2.916	2.913	2.837	2.945	2.890	2.931
<b>4ib</b>	3.522	3.588	3.534	3.530	3.324	3.335	3.378	3.369
<b>4iia</b>	3.127	3.148	3.150	3.147	3.017	3.099	3.123	3.147
<b>6iia</b>	3.156	3.164	3.177	3.175	3.046	3.107	3.155	3.155
<b>ADDITIONAL STRUCTURES</b>								
<b>1ie</b>	3.627	3.706	3.638	3.634	3.271	3.371	3.306	3.333
<b>1if</b>	3.758	3.879	3.754	3.750	3.378	3.565	3.378	3.425
<b>1ig</b>	3.610	3.776	3.595	3.591	3.204	3.353	3.246	3.254
<b>4ie</b>	3.391	3.462	3.404	3.400	3.163	3.317	3.155	3.212
<b>4if</b>	3.407	3.493	3.415	3.411	3.171	3.205	3.220	3.246
<b>4iie</b>	3.428	3.504	3.437	3.433	3.147	3.205	3.163	3.204
<b>4iif</b>	3.444	3.534	3.448	3.444	3.171	3.239	3.204	3.229
<b>4iiib</b>	3.512	3.575	3.527	3.520	3.297	3.335	3.324	3.315
<b>4iiie</b>	3.384	3.452	3.401	3.394	3.115	3.173	3.115	3.155
<b>4iiif</b>	3.401	3.483	3.413	3.406	3.147	3.197	3.163	3.179
<b>5iva</b>	3.163	-	3.188	3.186	3.077	-	3.171	3.171
<b>4ir</b>	4.159	4.215	4.169	4.164	3.792	3.877	3.803	3.839
<b>4is</b>	4.384	4.444	4.391	4.388	3.974	4.081	3.961	4.000
<b>4iu</b>	4.050	4.104	4.063	4.059	3.647	3.703	3.668	3.701
<b>4iis</b>	3.885	3.943	3.895	3.891	3.604	3.627	3.594	3.647
<b>4iit</b>	3.823	3.895	3.830	3.825	3.502	3.555	3.522	3.542

<b>4iiiir</b>	3.808	3.868	3.821	3.814	3.532	3.575	3.502	3.542
<b>4iiiu</b>	3.695	3.762	3.715	3.701	3.425	3.485	3.388	3.463
<b>DDNP</b>	3.139	3.223	3.147	3.143	2.811	2.996	2.857	2.890
<b>FDDNP</b>	3.213	3.308	3.216	3.213	2.877	3.048	2.904	2.924
<b>A1</b>	3.341	3.312	-	3.364	3.254	3.280	-	3.289
<b>A2</b>	3.176	3.155	3.199	3.197	3.237	3.245	3.246	3.229

Molecules **1ib** – **6iaa** in Table 4.1 correspond to the molecular probes studied in this chapter that have experimental data available. For validation purposes, we also included the computed adsorption energies of molecules **1ie** – **A2**, which are not included in the submitted manuscript related to the work presented in this chapter (See structures below, Figure 4.4).

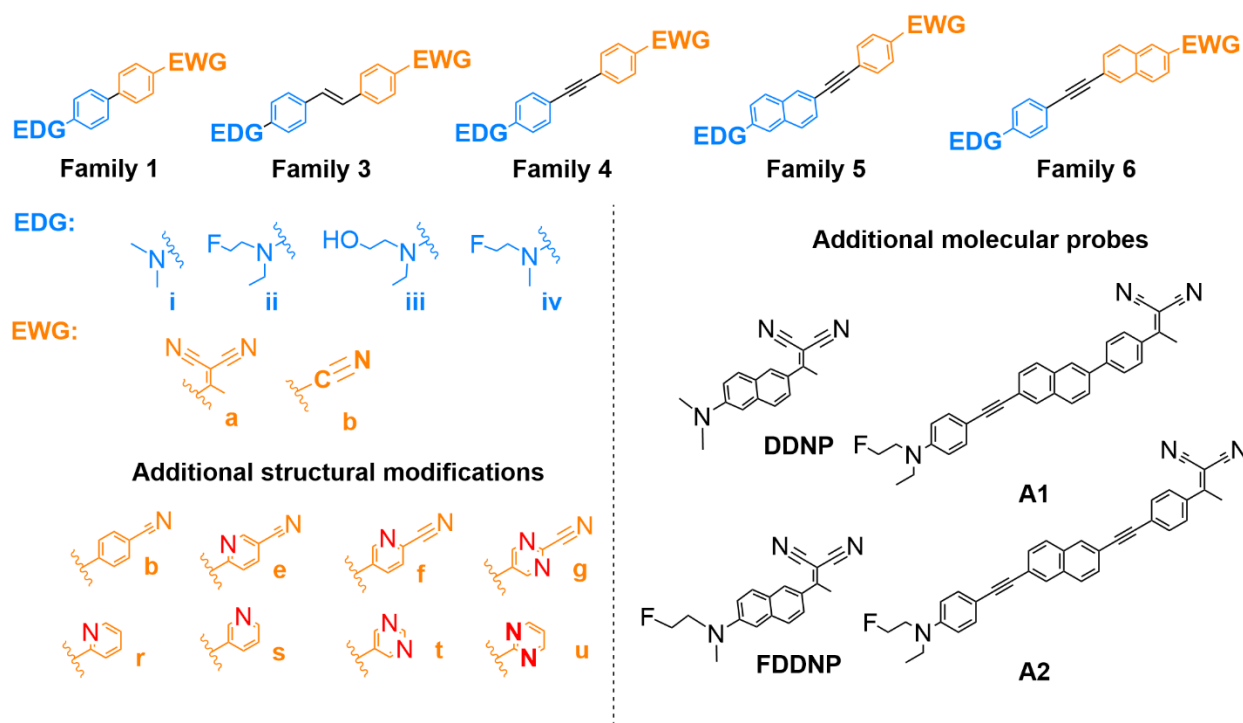


Figure 4.4: Structures of the molecular probes considered in Table 4.1

Figure 4.5 shows the corresponding correlation between experimental absorption energies with those calculated using the M062X functional coupled with the correlation-consistent triple- $\zeta$

basis set cc-PVTZ. The correlations between experimental and computed excitation energies were relatively strong in all studied solvents ( $r^2 = 0.91$  in DCM and hexane, 0.92 in acetonitrile, and 0.90 in methanol).

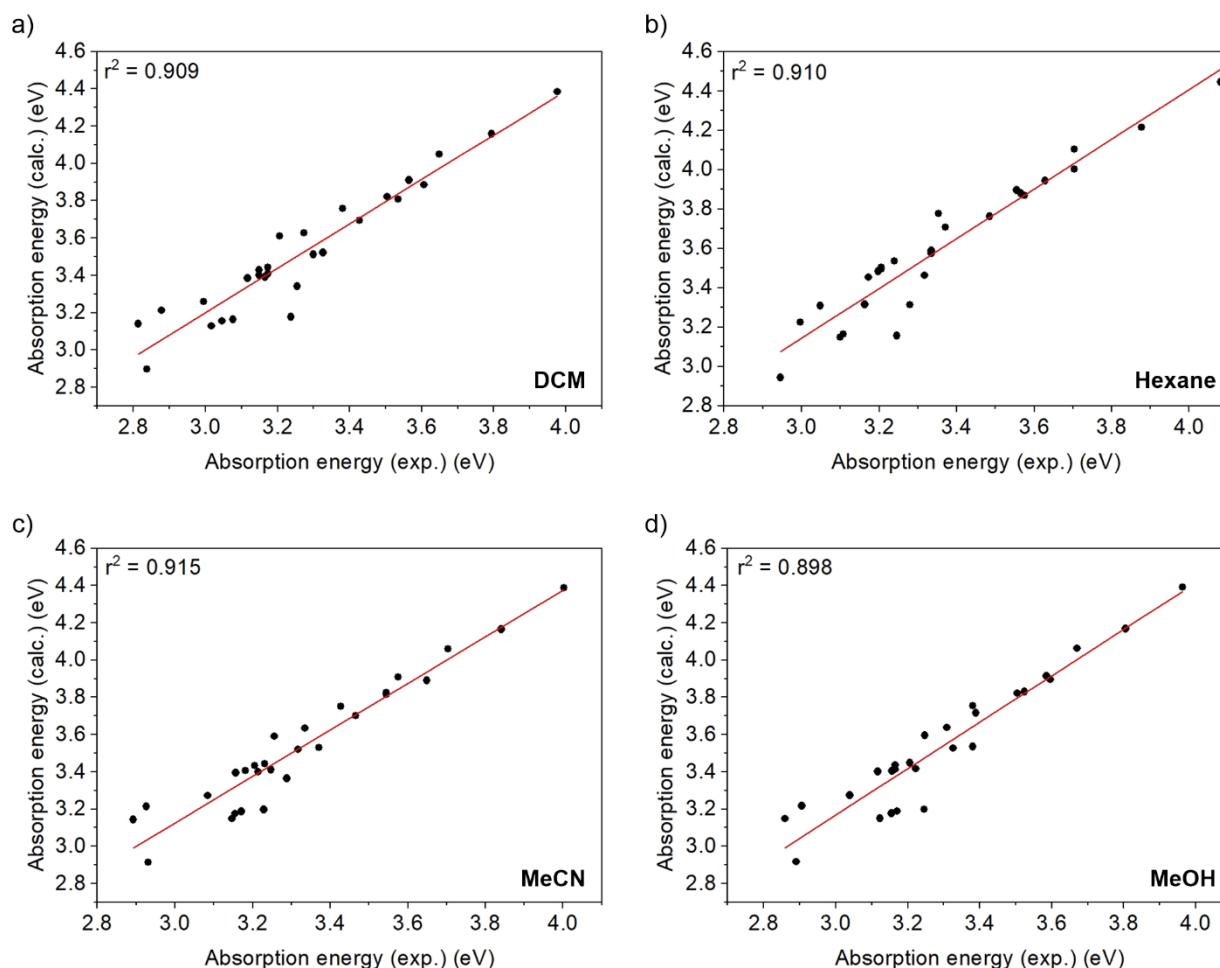


Figure 4.5: Correlation between computed and experimental absorption energies in a) dichloromethane (DCM), b) hexane, c) acetonitrile (MeCN), and d) methanol (MeOH) calculated at M062X/cc-PVTZ level of theory, involved molecular probes specified in Table S2.

Admittedly, however, DFT systematically overestimates the empirical excitation energies, resulting in the mean absolute errors (MAE) and root mean square deviations (RMSD) (see Table 4.2) ranging from 0.21 eV – 0.28 eV and 0.24 eV – 0.28 eV, depending on the solvent, respectively.

Table 4.2: RMSD and MAE for the computational predictions in all solvents (eV)

	DCM	Hexane	Acetonitrile	Methanol
<b>RMSD</b>	0.276	0.267	0.239	0.275
<b>MAE</b>	0.279	0.236	0.212	0.247

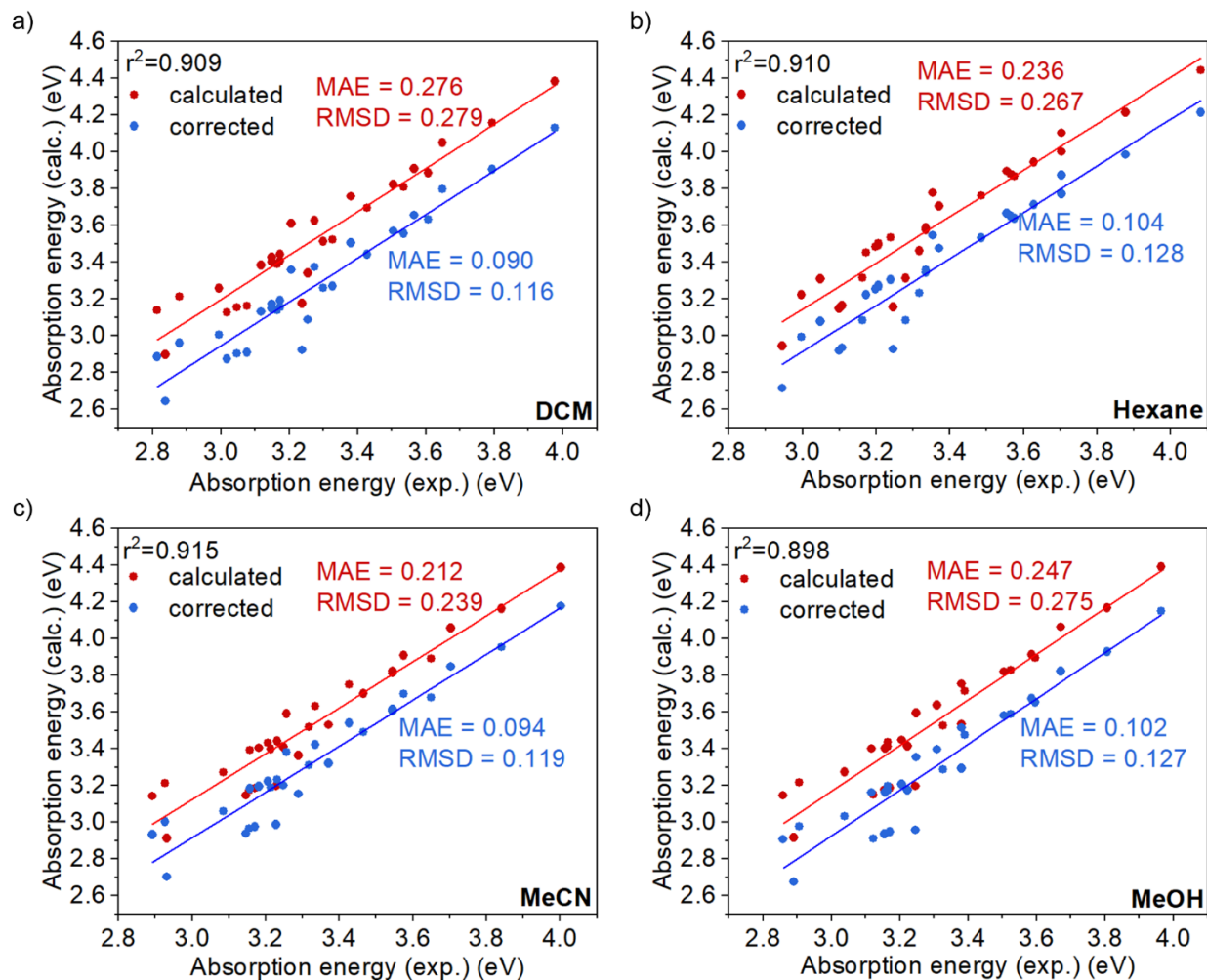


Figure 4.6: Calculated and corrected values of absorption energy. Mean absolute error (MAE) and mean squared root deviation (RMSD) are presented in each case.



The latter deviations are in the order of the expected deviation for TD-DFT methodologies ( $\sim 0.23$  eV) as reported previously by Mester and Kallay<sup>95</sup> at the high-rung DSD-PBEP86 functional, considered one of the most advanced functionals to date. The underlying systematic error can be corrected, resulting in an average decrease of RMSD and MAE to 0.12 eV and 0.10 eV, respectively (See Figures 4.6 and 4.7). Our results confirm the validity of using TD-DFT and the selected level of theory in our study to qualitatively identify the correct excitation and adequately capture the essential alterations in the electronic structure.

The error was corrected by subtracting the mean of the deviations between calculated and experimental values from the absorption energy values in each solvent. Figure 4.7 presents the correlation between computed and experimental absorption energies in nm, using dichloromethane (DCM) as solvent after correcting the systematic error. An excellent correlation factor ( $r^2=0.91$ ) was obtained.

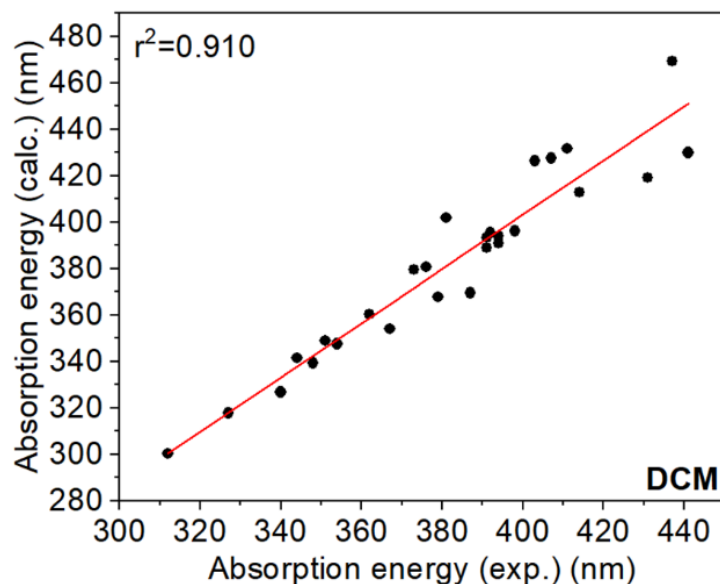


Figure 4.7: Correlation between corrected computed and experimental absorption energies (nm) in dichloromethane (DCM). Calculated at M062X/cc-PVTZ level of theory

### 4.3.2 Nature of the S<sub>1</sub> State

The study of the S<sub>1</sub> excited state provides key insights into the electronic and structural changes triggered by photoexcitation. It is essential for establishing the details of the photophysics of these species and putting forward structure-optical property relationships and design guidelines. As detailed in the following paragraphs, most of the studied fluorescent probe molecules have a twisted intramolecular charge transfer (TICT) first singlet excited state, and accordingly, the S<sub>0</sub> → S<sub>1</sub> can be termed a TICT excitation. In contrast, one of the selected bridge groups leads to the planarization of the S<sub>1</sub> state, resulting in planar intramolecular charge transfers (PICT) that significantly impact the quantum efficiency of fluorescence in certain families of probes.

Let us begin the discussion by analyzing molecular geometries and their changes due to photon absorption. The equilibrium structures of S<sub>0</sub> and S<sub>1</sub> states are given in Figure 4.8 for a set of molecules, each representing one of the studied families. For all probes, we found that the planes of the D-B-A groups are coplanar or quasi coplanar in the ground state, characterized by dihedral angles in the range of 0 to 10° and 10 to 35°, respectively, as showcased by Figure 4.8 for the representative structures. This relative orientation of donor and acceptor planes changes significantly after photon absorption, leading to a quasi-perpendicular arrangement of the cationic (D<sup>+</sup>) and anionic (A<sup>-</sup>) poles. The twisting occurs along the core C–C, C–C=C–C, and C–C≡C–C cores of the bridge groups (see dihedral angles in Figure 4.8). For example, **1iia** and **4iia** go from  $\alpha = 33.0^\circ$  and  $0.5^\circ$  in S<sub>0</sub> to  $\alpha = 90.5^\circ$  and  $90.6^\circ$ , in S<sub>1</sub>, respectively. Interestingly, when the bridge group has a non-linear C–C=C–C core, such as in **3iia**, which is in contrast to families with C–C and C–C≡C–C cores, the twisting distortion remains modest, resulting in a quasi-planar orientation of D<sup>+</sup> and A<sup>-</sup> groups after excitation, e.g., the twisting angle goes from  $\alpha = 5^\circ$  in S<sub>0</sub> to  $\alpha = 26^\circ$  in S<sub>1</sub> in the case of **3iia**.

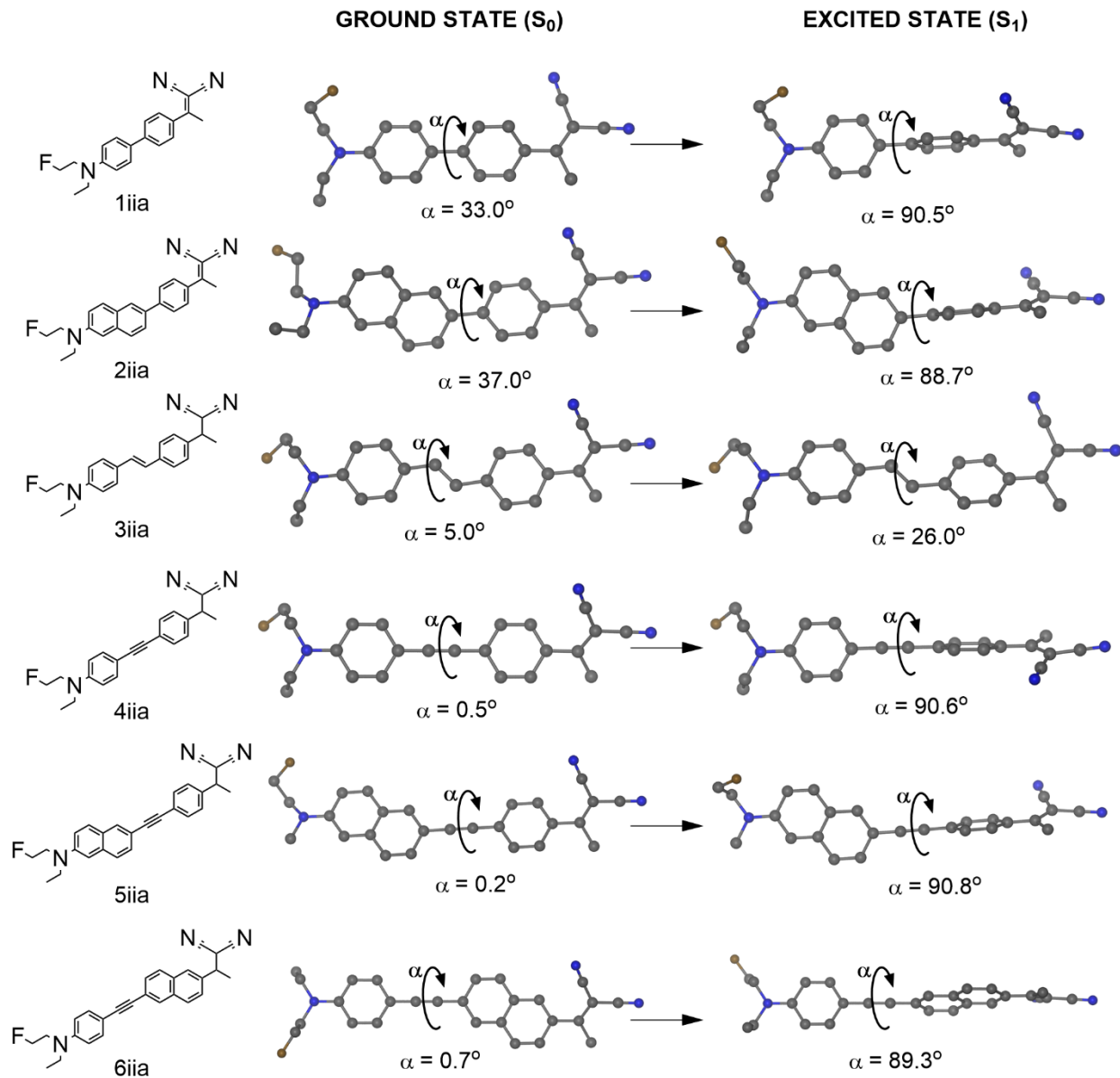


Figure 4.8: Equilibrium structures of the ground ( $S_0$ ) and excited states ( $S_1$ ) for the parent species of families 1-6.

Concerning the electronic structure reorganizations, first, we determined that for compounds **1iia** – **6iia**, the  $S_0 \rightarrow S_1$  excitation is of HOMO-LUMO character dominantly, describing about 65% of the overall electronic structure change due to photon absorption, with minor contributions from several other occupied-virtual orbital pair transitions. Accordingly,

examining the frontier HOMO-LUMO orbitals for the representative molecules of families **1 – 6** in Figure 4.9 provides a realistic first-order approximation for the key electronic structure reorganizations during excitation.

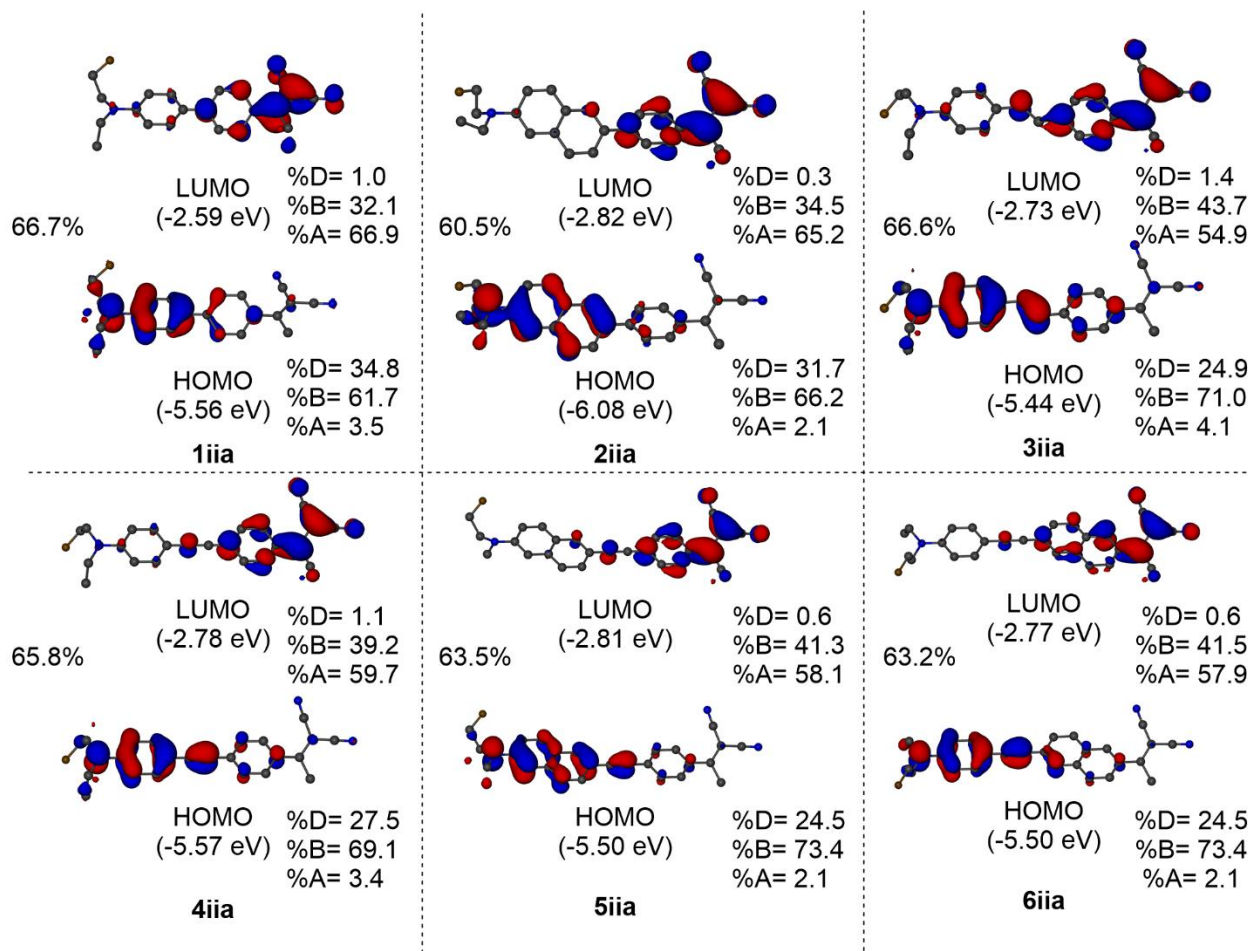


Figure 4.9: HOMO – LUMO orbitals for the parent molecules of families **1-6**. The computed weight of the HOMO – LUMO transition to the  $S_0 \rightarrow S_1$  vertical excitation is provided. Orbital composition analysis based on Mulliken partition (D: donor, B: bridge, A: acceptor)

The topology of the HOMO shows a delocalized distribution with a substantial wavefunction amplitude at the donor group (%D = 34.8 for **1iia**, %D = 31.7 for **2iia**) and that combines with the  $\pi$  orbitals of the adjacent aromatic ring of the bridge (%B = 61.7 for **1iia**, %B = 66.2 for **2iia**), and with a minimal delocalization towards the acceptor fragment (%A = 3.5 for

**1iia**, %A = 2.1 for **2iia**). On the contrary, exhibiting a  $\pi^*$  character, the LUMO is confined primarily to the acceptor fragment (%A = 66.9 for **1iia**, %A = 65.2 for **2iia**), also with some delocalization to the adjacent aromatic ring of the bridge, in addition to a negligible amplitude at the donor fragment (%D = 1 for **1iia**, %D = 0.3 for **2iia**). A consistent pattern was observed across all families showing that the electron promotion from HOMO to LUMO during the  $S_0 \rightarrow S_1$  transition results in a significant shift of electron density from the donor to the acceptor fragments of the molecule, indicating a characteristic charge transfer excitation.

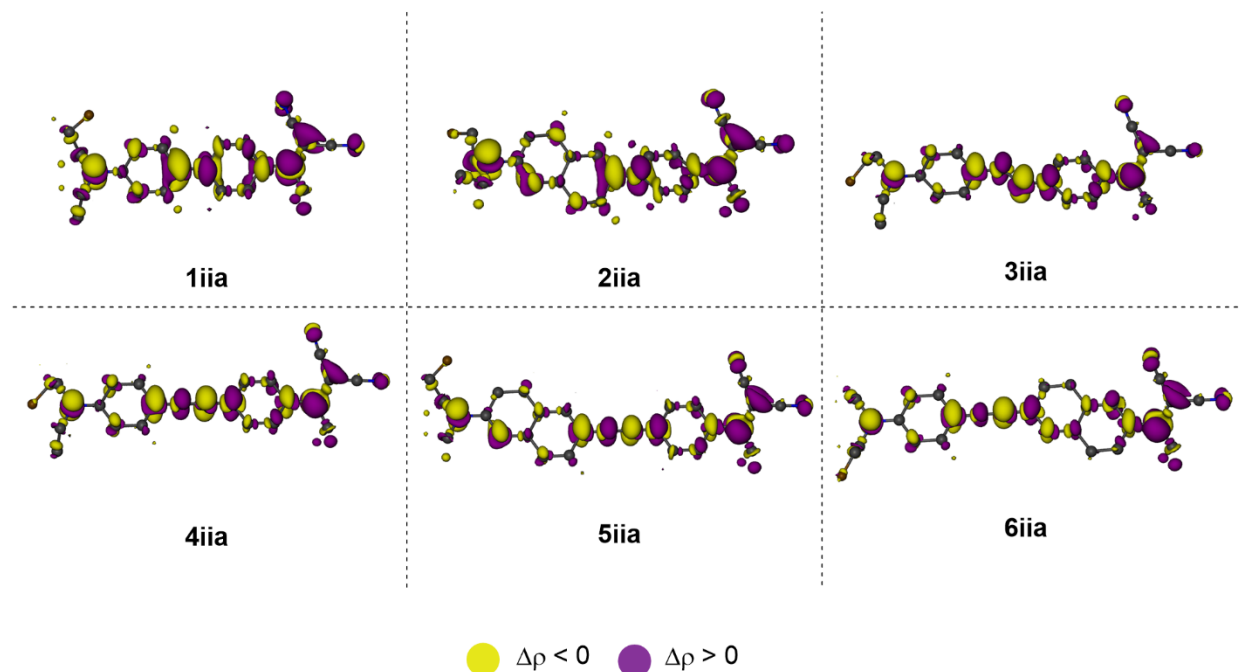


Figure 4.10: Electron density difference distributions ( $\Delta\rho$ ) for the  $S_0 \rightarrow S_1$  transition of the parent molecules of families **1-6**.

TD-DFT calculations were carried out at the ground state geometry to corroborate the nature of these charge transfer excitations, providing the electron densities of both  $S_0$  and  $S_1$  states at a fixed nuclear position. Given these data, electron density difference distributions ( $\Delta\rho$ ) were constructed and plotted for the  $S_0 \rightarrow S_1$  transition (Figure 4.10) to further evidence the charge

transfer processes upon excitation. The accumulation of electron density (purple regions) in the  $\pi$ -subspace of the acceptor group and depletion (yellow areas) from the  $\pi$ -subspace of the donor moiety is a general feature characteristic of all the studied systems, signaling the expected ICT process for these D-B-A type probes. These findings are in good accord with earlier findings on the photophysics of other push-pull fluorophores.<sup>82,115,116</sup>

Considering the characteristic structural and electronic changes, these simulations demonstrate a twisted intramolecular charge transfer (TICT) process upon photoexcitation. While much forgotten in the last decades, TICT has earned attention for its potential application in fluorescent spectroscopy. Namely, TICT is one of the essential elements of dual fluorescence, which involves the participation of two different excited electronic states, and in most cases, dual emission was attributed to the lowest excited state according to the empirical Kasha's rule.<sup>117</sup> In particular, thorough investigations were carried out in this regard by Grabowski<sup>93</sup> during the 80s, that revealed, amongst others, that although radiative decay from the TICT state to the ground state is quantum mechanically forbidden, some weak fluorescence is manifested due to low-energy asymmetric vibrations in the TICT excited state. Also, the absence of fluorescence in water was attributed to H $\cdots$ lone pair interactions, which effectively quench the TICT excited state, leading to extremely fast non-radiative de-excitations. Based on these concepts, further experimental studies give valuable insight into the relationship between structure and optical property, providing a rationale for the environment-dependent Stokes shift and solvatochromism.<sup>118</sup>

In summary, the TICT is characterized by a planar or quasi-planar ground state to a twisted or distortion in the molecule when reaching the excited state. The electron-donating group loses an electron, and the acceptor side gains it, leading to a change in charge distribution in the molecule, thus defining an intramolecular charge transfer excitation that is very sensitive to the local

environment<sup>82,119</sup> Some studies have mentioned that the molecular probes face a PICT inside the plaques and a TICT excited state in solution-state.<sup>25,119</sup>

### 4.3.3 Effect of donor, acceptor, and linker groups on the absorption energies

Understanding the effect of the strength, structure, and functionalization of the donor, acceptor, and bridge groups on the photophysical properties of these probes is vital to develop structure – property relationships for the engineering of potential molecular fluorophores for the early detection of Alzheimer’s disease.<sup>115,120,121</sup> Accordingly, the effect of donor, acceptor, and linker on the absorption energies was systematically studied considering families **1** – **6**, with donors **i-iv** and acceptors **a-d**, as shown in Figure 4.2a.

Figure 4.11 shows the corresponding heat maps intuitively demonstrating the influence of the different structural groups on the absorption energies. While it may be challenging to establish trends in certain cases due to specific changes caused by various D–B–A combinations, some patterns can be identified from the data.

When comparing Families **1** and **2** vs. **3** – **6**, introducing double and triple bonds within the linker structure leads to an overall decrease in absorption energies. Namely, using *trans*-stilbene (**3**) as the linker of the molecular probes decreases the absorption energy by 0.50 eV on average when compared to biphenyl (**1**) and 0.60 eV to 2-phenylnaphthalene (**2**). Diphenylacetylene (**4**) and 2-(phenylethynyl)naphthalene (**5, 6**) (i.e., featuring a triple bond) cause a decrease of 0.27 eV – 0.30 eV in the absorption energy vs. The observed behavior aligns with the theory as introducing a triple bond enhances the  $\pi$ -spacer. This  $S_0 - S_1$  energy gap decrease can be attributed to the increased overlap of p-orbitals through the triple bond, leading to a more efficient delocalization of electrons along the  $\pi$ -system. Consequently, the energy levels associated with the electronic

transitions are lowered, translating into a redshift of the absorption spectrum.<sup>122</sup> Double bonds also lead to efficient p-orbital overlaps. Additionally, the electronegativity of a triple bond, higher than that of a double bond, can cause a counteracting effect, weakening the electron-withdrawing ability of the acceptor group and causing less red-shifted absorption energies. The extension of the aromatic ring system in **4** vs. **5** and **6** seems to have a minor effect on the absorption energies and the position of the acceptor and donor moieties as in **5** vs. **6**.

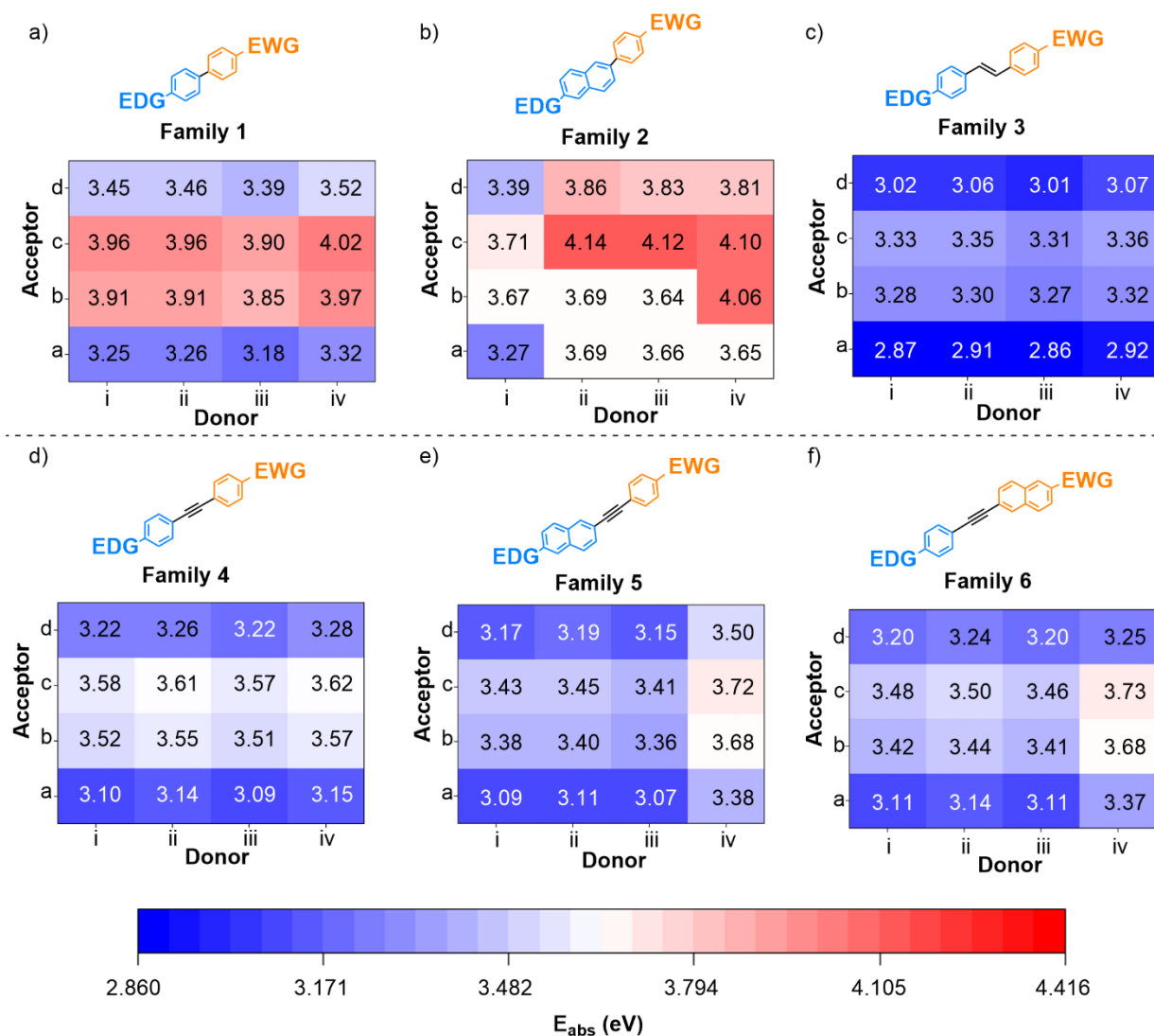


Figure 4.11: Heat maps demonstrating the influence of donor, acceptor, and linker groups on absorption energies (reported in eV).



The heatmaps reveal that whether incorporating different donor species such as dimethylamine (**i**), N-ethyl-N-(2-fluoroethyl)amino (**ii**), N-ethyl-N-(2-hydroxyethyl)amino (**iii**), and N-methyl-N-(2-fluoroethyl)amino (**iv**) does not lead to significant changes in absorption energies across the investigated families (less than  $\pm 0.1$  eV in most of cases). Family **2** deviates from the general trend when using dimethylamine (**i**), where the absorption energies are redshifted by 0.41 eV compared to the other donors (except for **2bi** – **2biii**). Additional exceptions are observed in families **5** and **6** when using N-methyl-N-(2-fluoroethyl)amino (**iv**), which increases the absorption energy of around 0.30 eV compared to the other donor species.

Acceptor moieties also influence the  $S_0 - S_1$  energy gap. In general, ethylenemalononitrile (**a**) registers the lowest absorption energy values, followed by nitro, **d** ( $\sim 0.15$  eV blueshift vs. **a**), nitrile, **b** ( $\sim 0.41$  eV blueshift vs. **a**), and methoxycarbonyl, **c** ( $\sim 0.46$  eV blueshift vs. **a**). This trend can be observed in all the families across all donating species except for **2bii**, **2biii**, and **6div**. This order, **a** < **d** < **b** < **c**, indicates that stronger electron-withdrawing species (e.g., ethylenemalononitrile group) will shift the absorption energies to longer wavelengths.

#### 4.3.4 Pyridine, pyrimidine, and pyranone derivatives as acceptors

With the effects of simple donor and acceptor functionalization quantified, we studied the impact of more complex structural modifications. Given the different behavior of families **1**, **2**, and **3-6**, we performed this subsequent systematic study for groups **1**, **2**, and **5** utilizing N-ethyl-N-(2-fluoroethyl)amino (**ii**) as the donor and 4-cyanophenyl (**b**) and 4-nitrophenyl (**d**) as the acceptor fragments in which one or two CH groups of the benzene ring were substituted with nitrogen (see Figure 2). The general idea behind the introduction of a more electronegative atom into the benzene ring (i.e., nitrogen) is that it increases electron affinity of the acceptor group and

its electron-withdrawing capability and also contributes to having a more efficient delocalization of the electrons along the  $\pi$ -system, lowering the energy levels associated with electronic transitions which will ultimately be reflected in the redshift in the absorption spectra.<sup>123</sup> Also, the difference in electronegativities of nitrogen and carbon introduces a degree of asymmetry which affects the nature of conjugation, making the  $\pi$ -electron system non-uniform and that either enhances or downplays the mesomeric effect of the EWG group attached to the ring.

The heatmaps in Figure 4.12 show the effect of these structural modifications on the absorption energies.

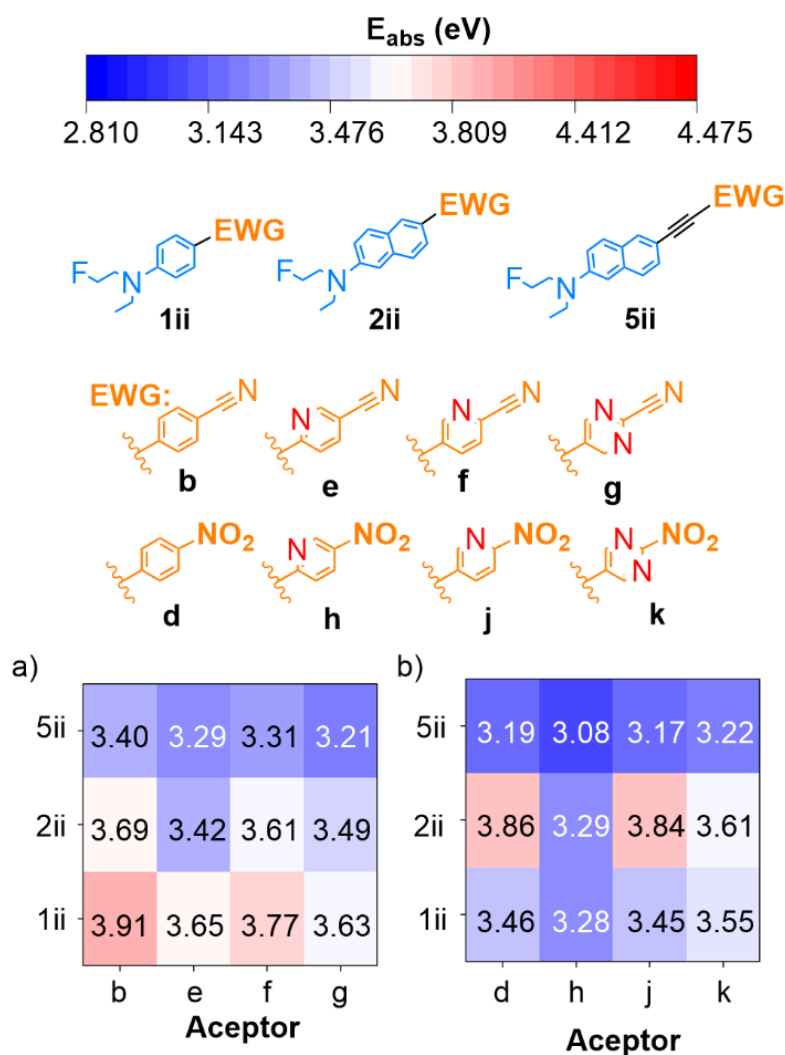


Figure 4.12: Impact of additional structural modifications on absorption energies.

For the 4-cyanophenyl type acceptor groups (**b** – **g**, Fig. 4.12a), the substitution of carbon for nitrogen in the backbone of the aromatic ring of the acceptor site redshifts the absorption energies by about 0.1 to 0.3 eV. This lowering of the  $S_0 - S_1$  energy gap appears to be independent of the functionalization site (5-cyanopyridin-2-yl (**e**) vs. 6-cyanopyridin-3-yl (**f**) vs.) for the 2-(phenylethynyl)naphthalene bridge (**5**) and is in the range of 0.1 eV, whereas clear position-dependent redshift is witnessed for families **1** and **2**, i.e., with shorter biphenyl and 2-phenylnaphthalene linkers; the shift is about 0.25 eV for CH/N substitution at the vicinal to the bridge position and about 0.1 eV at the more distant position. Similarly, substituting a second CH group by nitrogen in the aromatic ring, 2-cyanopyrimidin-5-yl (**g**), has little effect on the absorption energy for **5**, whereas its contribution appears to be additive for **1** and **2**.

However, similar trends, with different magnitudes, can be observed for nitrobenzene type acceptor groups (**d** – **k**) in Figure 4.12b. Namely, the substitution of the CH group with nitrogen in **d** at the vicinal to the bridge position, 5-nitropyridin-2-yl (**h**), decreases the absorption energy by 0.18 eV, 0.57 eV, and 0.11 eV for **1iih**, **2iih**, and **5iih**, respectively, again having the least pronounced effect in the case of **5**. In contrast, the incorporation of nitrogen has a negligible effect if it takes place in a more distant position (i.e., **1iij** – **5iij**). The effect is somewhat more visible when both CH groups in the more distant position are replaced with nitrogen, 2-nitropyrimidin-5-yl (**k**), which leads to a decrease of 0.25 eV only for **2iik**, while its effect remains negligible for **1iik** and **5iik**. The position-dependent effect of CH/N substitution reveals that not only are electrostatics at play, but resonance effects also have a crucial contribution to stabilizing the charge-separated excited state. Namely, simple electrostatics, given the larger electronegativity of nitrogen to carbon, would stabilize the negative charge at the acceptor site in the excited state independently from the position of CH/N replacement, and the more CH/N exchange, the larger

the effect would be. Resonance (i.e., mesomeric) stabilization, on the other hand, is position-dependent, as manifested, for example, in the characteristic orientation rules in electrophilic aromatic substitutions. Accordingly, the observed trends imply a resonance-type delocalization between the cationic donor and anionic acceptor in the excited state. This rationale also explains the strong dependence of the manifestation of the CH/N substitution in the absorption energies on the bridge functionality, especially the acetylene group, which seems to limit the resonance effect between donor and acceptor, leading to a minor contribution from CH/N substitution.

To explore these ideas further, we extended this systematic analysis also to study the effect of pyranone derivatives using the same families mentioned above (**1**, **2**, and **5**) and utilizing N-ethyl-N-(2-fluoroethyl)amino (**ii**) as the donor. Especially, pyran-4-one (**I**) and pyran-2-one (**o**) as acceptors were studied. Also, the influence of a methyl group at both the vicinal to the bridge (**m**, **p**) and more distant (**n**, **q**) positions was scrutinized in each case. Figure 4.13 shows the corresponding heatmap with the effect of pyranone derivatives and their methyl functionalization on the absorption energies.

Similarly to the above-discussed trends, the effect of these oxygenated groups is significantly affected by the bridging group. For example, the isomer pyran-4-one (**I**) leads to a blueshift of the absorption energy for **2ii** in 0.25 eV; meanwhile, it has a marginal effect in **1ii** and **5ii**. In contrast, isomer pyran-2-one (**o**) induces a redshift of an average of 0.70 eV, mostly independent of the nature of the linkers. The fact that the relative position of the oxygen with respect to the other functional groups, including the bridging moiety, plays such a key role in determining the absorption energy indicates that mesomeric effects are a crucial stabilizing factor in the charge-separated excited state.

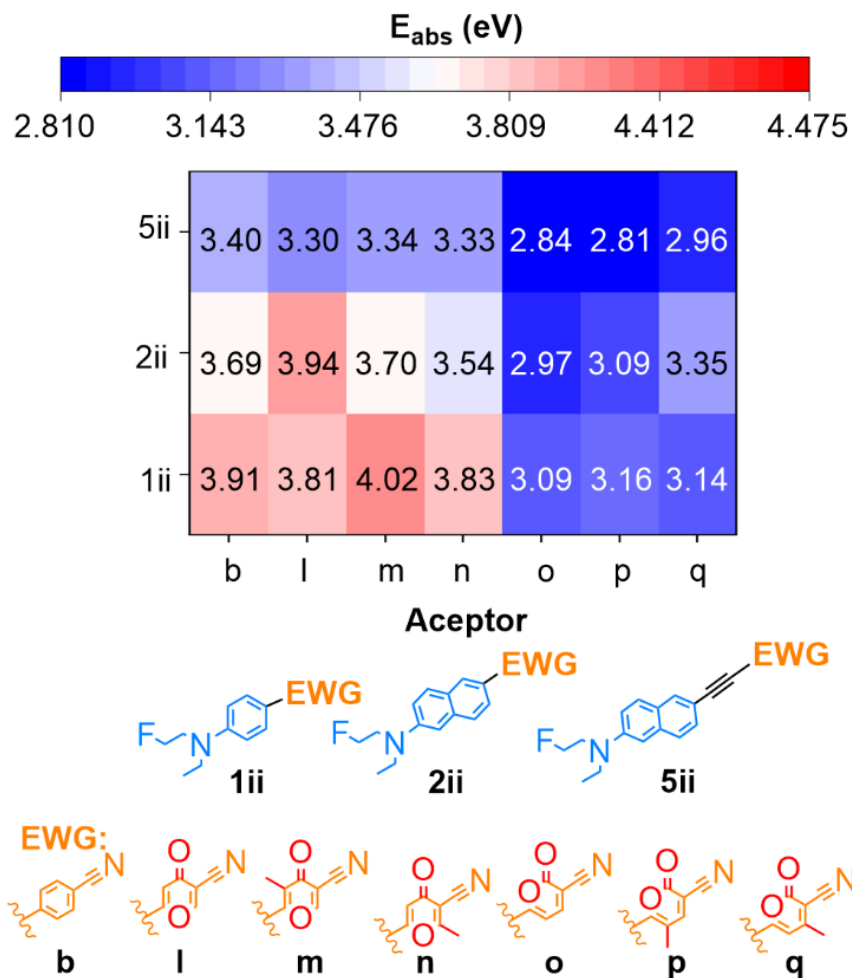


Figure 4.13: Impact of pyranone derivatives and their functionalization at the acceptor site on absorption energies

The addition of the methyl group in the vicinal to the bridge position (**m**, **p**) in pyranone derivative groups does not have an additional significant effect on the absorption energy ( $<0.15$  eV), which is expected given that these are groups with moderate +I effect (inductive effect). Interestingly, however, adding the methyl groups in the more distant positions (**q**, **n**), while it does not cause a significant effect in **1ii** and **5ii**, it eventuates in a redshift or blueshift of  $\sim 0.4$  eV in **2ii**, with respect to the unsubstituted **l** or **o** isomers, respectively. The origin of this effect is currently unknown.

#### 4.3.5 Training a machine learning (ML) model based on the calculated absorption energies

As showcased above, quantum mechanical calculations can determine functionally important properties of molecular probes, such as absorption or emission energies and quantum yields. The *in silico* examination and design of these properties could be significantly accelerated for new molecular probes if a machine learning model could be trained to predict these properties accurately. To determine whether a predictive machine learning model can be obtained based on the results of the quantum chemistry calculations performed in this study, we assembled a dataset of the calculated absorption energies for 324 molecular probes. This set of molecules comprises the 138 molecular probes studied here, alongside an additional 22 molecules considered for the validation (see Table 4.1) and a supplementary set of 164 molecules computed to enhance the capacity of the ML model. The latter subset of 164 molecules corresponds to combinations derived from families **1**, **2**, and **5** incorporating acceptors **i** – **iv** and donors **a** – **u**.

After training regression ML models based on the support vector machine algorithm on 259 probes (80% of the dataset), the performance of these models was evaluated on the testing dataset, comprising the remaining 65 probes (20% of the dataset). The performance of two types of the SVM models, where molecular probe structures were represented with Morgan fingerprints, is shown in Figure 4.14. The correlations between the absorption energies acquired from quantum chemical calculations and those predicted by one of our representative RBF SVR models on the test part of the dataset are depicted in Figure 4.14a. The correlation is reasonable and significant based on the  $r^2$  value of 0.941.

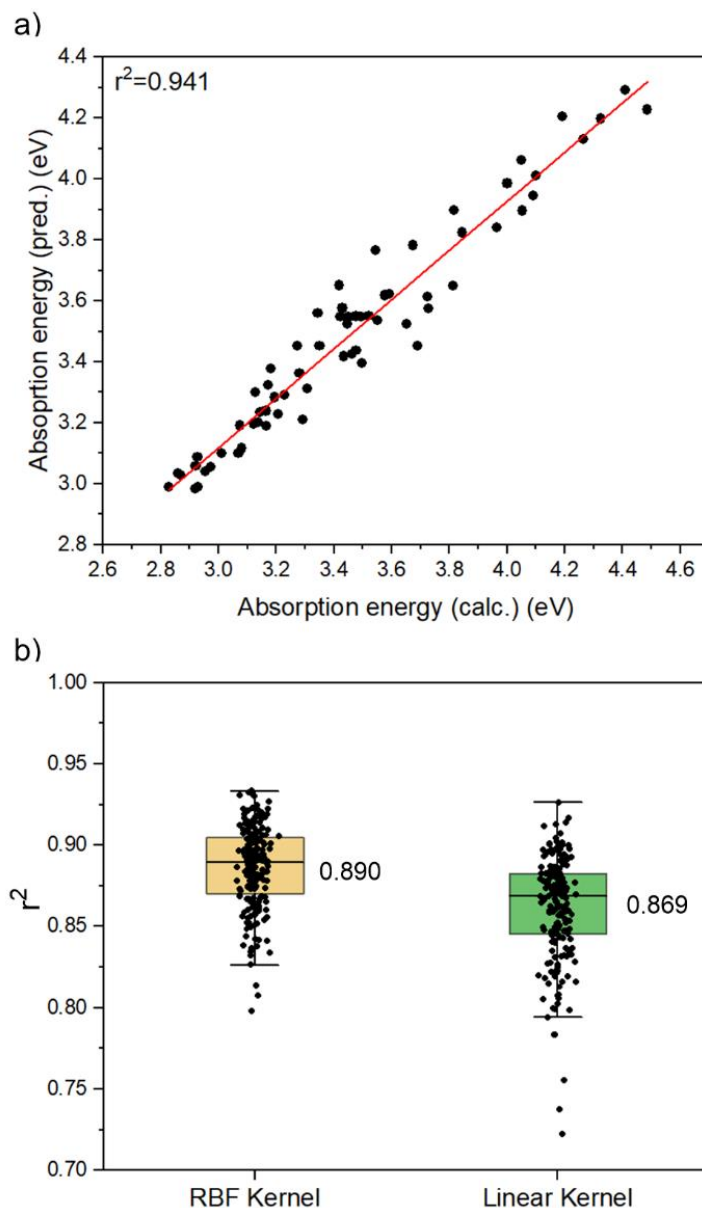


Figure 4.1: a) Correlation between predicted and calculated absorption energies, where the predicted energies were obtained from the SVM model with RBF kernel that had the best value of  $r^2$ , b) Box plots showing a distribution of the  $r^2$  values for 200 distinct machine learning models trained with RBF and linear SVM kernel models. The median values of the  $r^2$  distribution are noted in each case.

To investigate if the performance of the model is dependent on the molecules that are included in the testing and training parts of the dataset and to test the dependence of the model on SVR kernels, 200 random SVR models were trained, each with RBF kernel or linear kernel. The

distribution of  $r^2$  values for all these models for each kernel is shown in Figure 4.14b. The median  $r^2$  values of 0.890 and 0.869 are obtained for RBF and linear kernels, respectively. These values indicate that despite the relatively small size of the dataset of 324 molecules in total, all the models are significantly accurate with an  $r^2$  of about 0.9, and the model performance varies only slightly with the choice of SVR kernels.

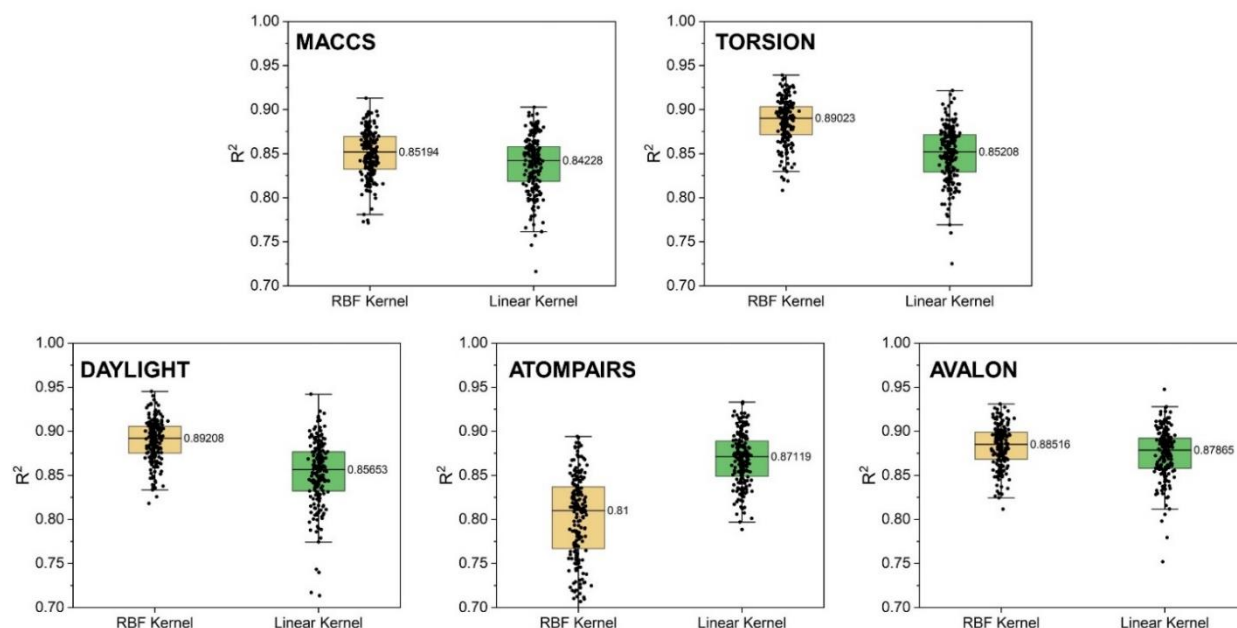


Figure 4.15: Dependency of trained ML models quality on molecular fingerprint type. Box plots showing distributions of the  $r^2$  values for the 200 machine learning models, each trained with RBF and linear kernels using five different fingerprints from RDKit. The median values of the  $r^2$  distributions are noted in each case.

We also examined if using different molecular fingerprints to represent the molecular structures can lead to a significant difference in model performance (performed with the assistance of my colleague Ms. Sayantani Chakraborty). Figure 4.15 shows similar boxplot distributions as Figure 10 b) for five types of molecular fingerprints tested. Based on the median  $r^2$  values for each kernel and fingerprint type, it can be concluded that models with Morgan and Topological Torsion fingerprints perform best. However, models with all the other fingerprint types also perform similarly well, with prediction accuracy mostly greater than 80%.



## 4.4 CONCLUSIONS

In this study, we investigated the electronic structure of the ground and excited state of a total of 138 D-B-A-like fluorescent molecular probes grouped in six families (based on the linker used). The push-pull electron effect was generated in these probes through a rod-like geometry and extended  $\pi$ -conjugated framework comprising naphthalene, benzene, ethyne, and ethene building blocks. Our DFT and TD-DFT protocols were validated using a subset of the molecular probes for which experimental data was available, and X-ray structures were reproduced by our calculations with deviations smaller than 0.02 Å. Furthermore, although overestimated notably by 0.23 eV on average, a direct correlation ( $r^2 > 0.9$ ) was found between the experimental and calculated absorption energies in different solvents, namely, DCM, hexane, acetonitrile, and methanol, which substantiating the selected level of theory, in terms of adequately identifying the excitation and capture the main changes in the electronic structure.

Calculations revealed a TICT first singlet excited state for most of the families after photon absorption, and the  $S_0 \rightarrow S_1$  excitation is predominantly of HOMO-LUMO character, accounting for approximately 65% of the overall electronic structure.

Furthermore, our calculations of 96 molecular probes from 6 different families showed that introducing double bonds in the linker leads to a redshift in the absorption energies in around 0.5 eV (i.e., 0.50 eV for trans-stilbene (**3**) vs. phenyl (**1**)), meanwhile introducing triple bonds cause a decrease of 0.29 eV on average (i.e., 0.27 eV for diphenylacetylene (**4**) vs. **1**). Donors, with groups of varying inductive effects, were found to have a small influence on the absorption energies across most of the investigated families. In contrast, acceptor fragments were found to influence the absorption energies of the molecular probes, where generally, the stronger the electron-withdrawing species are associated with a larger redshift of the absorption energies.

Additionally, in the 4-cyanophenyl type acceptor groups (**b-g**), the substitution of carbon with nitrogen in the backbone of the aromatic ring consistently led to a redshift in the absorption energies (0.18 eV on average), regardless of the functionalization site (i.e., vicinal to the bridge vs. more distant positions) or the number of nitrogen atoms that replaced CH in the aromatic ring. On the other hand, when having nitrobenzene-type acceptor groups (**d – k**), family 2 deviated from the general trend. Substituting one CH group with nitrogen in the vicinal to the bridge position leads to the redshift of the absorption energy by 0.57 eV for **2iih**. Substituting two CH groups (i.e., having 2-nitropyrimidin-5-yl, **k**) produced a redshift of the energy by 0.25 eV for **2iik**. Negligible effects were found for the other families of molecules and molecules having substitutions in the more distant position of the acceptor groups.

Introducing pyranone derivatives caused a redshift in the absorption energies that depend on the position of the oxygen and carbonyl groups. The pyran-2-one (**o**) induced a decrease in the absorption energy of around 0.70 eV independently of the bridge, whereas the 4-pyrone (**l**) induced the blueshift of ~0.25 eV in probe **2ii**. A non-significant effect was observed for the probe species from the other families. The addition of the methyl group in the vicinal to the bridge positions in pyranone derivative groups did not have an additional significant effect on the absorption energy, but adding methyl groups in the more distant positions produced a blueshift or redshift of 0.4 eV for probes **2ii** depending on the pyranone employed. We are currently unsure whether or not the latter shifts are artifacts of simulations.

Machine learning models trained on the dataset obtained from our quantum calculations demonstrate promising capabilities in predicting absorption energies for the fluorescent molecular probes investigated in this study. Among various machine learning approaches tested, employing the SVM model with the RBF kernel and Morgan fingerprints to represent molecular structures

proved to be the most effective method. The trained models achieved a median  $r^2$  value of 0.89, indicating high predictive accuracy. Our results highlight the potential of machine learning methodologies trained on quantum chemistry data for predicting the absorption energies of new probes, even those that have not yet been synthesized. This finding corroborates previous studies on other types of molecules<sup>124</sup>. We envision extending this approach to predict emission energies and quantum yields, crucial characteristics in designing fluorescent molecular probes for early detection of Alzheimer's disease. In summary, our study underscores the utility of machine learning techniques in predictive modeling for molecular properties, offering promising avenues for advancing the development of fluorescent probes with enhanced performance. These computational studies, together with the experimental results provided by my collaborators (Košmrlj group), have been submitted for publication in a peer-reviewed journal.

## Chapter 5: Conclusion and Recommendations for future work

### 5.1 CONCLUSIONS

In this dissertation, we studied the relationship between molecular structure and optical properties of donor-bridge-acceptor fluorescent probes for detecting Amyloid- $\beta$  and p-Tau aggregates characteristic of Alzheimer's disease. Through computational studies using density functional theory (DFT) and time-dependent density functional theory (TD-DFT), we gained key insights into the behavior of excited states and the absorption properties of these molecular probes.

Chapter 3 of this dissertation focuses on understanding the relationship between the structure of the molecular probes and their optical properties. By using TD-DFT with implicit solvation methods, we described the nature of the excited states in these fluorescent probes, revealing important phenomena such as charge transfer excitations within molecules. Furthermore, the close agreement between experimental and calculated absorption energies confirmed the effectiveness of our computational approach in accurately capturing electronic structural changes and optical photophysical properties.

Expanding on these findings, Chapter 4 expanded our investigations to a wider range of molecular probes, systematically analyzing the influence of various structural modifications on their electronic structure and optical properties. The computational analysis of 138 fluorescent molecular probes allowed the identification of design principles governing absorption energies, such as the effects of different linkers and electron-withdrawing/donating groups. Our study revealed interesting trends, such as the impact of acceptor fragments on absorption energies and the shift induced by certain structural features like introducing more electronegative atoms in the backbone of the electron-withdrawing group. Moreover, our exploration of machine learning techniques showed promising capabilities in predicting absorption energies for new probes,

highlighting the potential of computational approaches in speeding up the design of next-generation fluorescent probes.

As mentioned before, these probes need to have specific characteristics in order to be able to detect the amyloid  $\beta$  aggregates and NFT in blood, where the concentration of these biomarkers is in the range of picomolar (pM) depending on the stage of the disease. Fluorescent molecular probes need to have absorption near 400 nm and emission in the near-infrared region (NIR), a big Stokes shift within this range, and high quantum yields. Also, their interaction with biomarkers through molecular docking and dynamic simulations will be necessary to gain a better understanding of their behavior. With the information we have after this study, it is unclear which molecular probes perform the best. Nevertheless, this research did provide insights into the influence of the donor, linker, and acceptor on the absorption of energy. Scientists can use the computational approach used herein to gain insights into the structural relationship over the emission energies, quantum yields, docking process, and dynamic simulations to modify the probes' structure accordingly. Once the relationship with all the important properties mentioned above is understood, we will be able to generate an in-silico database with molecular probes that comply with the best modifications derived from these studies. We will also be able to include ML to predict not only absorption energies but also emission energies, quantum yield, and docking scores of new molecular probes without synthesizing them. After that, scientists will be able to select the best candidates that will go through synthesis and experimental characterization, saving resources in the stage of theoretical pre-screening.

In summary, this dissertation contributes to advancing molecular design strategies for Alzheimer's disease detection by elucidating fundamental principles governing the optical properties of fluorescent probes, specifically absorption energies. By integrating computational

methods with experimental insights, our findings offer valuable guidance for the rational design of novel probes with improved performance characteristics. The application of machine learning techniques holds great promise in facilitating the rapid screening and optimization of fluorescent probes, ultimately advancing efforts toward early diagnosis and treatment of Alzheimer's disease.

## 5.2 RECOMMENDATIONS FOR FUTURE WORK

DBA molecular probes for AD detection should have specific characteristics for their application in blood (ex-vivo analysis). Although this work addressed some of these characteristics, further work is needed to accomplish our goal of developing sensitive, specific, safe, cheap, and accessible early detection tests for AD. Herein, we provide some recommendations for future directions of this work:

**1. Exploration of the emission properties using TD-DFT protocols:** while in this study, structure activity relationships for absorption energies were provided, the study of the emission properties is also needed to ensure that the molecular probes will have the targeted absorption and emission profiles.

**2. Exploration of additional structural modifications:** Including other structural effects could help derive additional design rules for tuning the optical properties of these molecular probes. The new structural modifications could include variations in the linker groups and introducing different functional groups to tune the absorption energies further and improve detection sensitivity.

**3. Elucidation of excited state dynamics and docking mechanisms:** Further study of the dynamics of the excited states of these fluorescent probes, including their relaxation pathways and emission properties, could yield more insights for enhancing the photostability and emission

characteristics of these molecular probes. Besides, understanding the specific interaction mechanisms of the molecular probes and the target proteins would be important for practical application in biological samples.

**4. Exploration of alternative machine learning approaches:** Investigate alternative machine learning approaches for predicting absorption energies and other optical properties of fluorescent probes, such as emission and quantum yields. Comparing different models and techniques could help identify the most effective methodologies for accelerating the design and optimization of molecular probes.

**5. Experimental validation:** Validate the computational predictions through experimental studies on a wider range of fluorescent probes would provide feedback on the accuracy of the computational models and enable refinement of the design principles proposed.

## References

- (1) Zvěřová, M. Clinical Aspects of Alzheimer's Disease. *Clin. Biochem.* **2019**, 72, 3–6. <https://doi.org/10.1016/j.clinbiochem.2019.04.015>.
- (2) Albert, M. S.; DeKosky, S. T.; Dickson, D.; Dubois, B.; Feldman, H. H.; Fox, N. C.; Gamst, A.; Holtzman, D. M.; Jagust, W. J.; Petersen, R. C.; Snyder, P. J.; Carrillo, M. C.; Thies, B.; Phelps, C. H. The Diagnosis of Mild Cognitive Impairment Due to Alzheimer's Disease: Recommendations from the National Institute on Aging-Alzheimer's Association Workgroups on Diagnostic Guidelines for Alzheimer's Disease. *Alzheimers Dement.* **2011**, 7 (3), 270–279. <https://doi.org/10.1016/j.jalz.2011.03.008>.
- (3) Alzheimer's Disease International. *Dementia Statistics*. <https://www.alzint.org/about/dementia-facts-figures/dementia-statistics/> (accessed 2024-03-23).
- (4) Alzheimer's Association. 2023 Alzheimer's Disease Facts and Figures. *Alzheimers Dement.* **2023**, 19 (4), 1598–1695. <https://doi.org/10.1002/alz.13016>.
- (5) Hippus, H.; Neundörfer, G. The Discovery of Alzheimer's Disease. *Dialogues Clin. Neurosci.* **2003**, 5 (1), 101–108. <https://doi.org/10.31887/DCNS.2003.5.1/hhippus>.
- (6) Korolev, I. O. Alzheimer's Disease: A Clinical and Basic Science Review. **2014**, 04.
- (7) National Institute on Aging. *Alzheimer's Disease Fact Sheet*. <https://www.nia.nih.gov/health/alzheimers-and-dementia/alzheimers-disease-fact-sheet> (accessed 2024-03-23).
- (8) Alzheimer's Association. 2016 Alzheimer's Disease Facts and Figures. *Alzheimers Dement.* **2016**, 12 (4), 459–509. <https://doi.org/10.1016/j.jalz.2016.03.001>.



- (9) Dickerson, B. C.; Eichenbaum, H. The Episodic Memory System: Neurocircuitry and Disorders. *Neuropsychopharmacology* **2010**, *35* (1), 86–104. <https://doi.org/10.1038/npp.2009.126>.
- (10) Moscoso, M. A.; Marques, R. de C. G.; Ribeiz, S. R. I.; Santos, L. dos; Bezerra, D. M.; Jacob Filho, W.; Nitrini, R.; Bottino, C. M. de C. Profile of Caregivers of Alzheimer's Disease Patients Attended at a Reference Center for Cognitive Disorders. *Dement. Neuropsychol.* **2007**, *1*, 412–417. <https://doi.org/10.1590/S1980-57642008DN10400015>.
- (11) National Institute on Aging. *Memory Problems, Forgetfulness, and Aging*. <https://www.nia.nih.gov/health/memory-loss-and-forgetfulness/memory-problems-forgetfulness-and-aging> (accessed 2024-03-23).
- (12) Hampel, H.; Frank, R.; Broich, K.; Teipel, S. J.; Katz, R. G.; Hardy, J.; Herholz, K.; Bokde, A. L. W.; Jessen, F.; Hoessler, Y. C.; Sanhai, W. R.; Zetterberg, H.; Woodcock, J.; Blennow, K. Biomarkers for Alzheimer's Disease: Academic, Industry and Regulatory Perspectives. *Nat. Rev. Drug Discov.* **2010**, *9* (7), 560–574. <https://doi.org/10.1038/nrd3115>.
- (13) Tiwari, V.; Solanki, V.; Tiwari, M. *In-Vivo* and *in-Vitro* Techniques Used to Investigate Alzheimer's Disease. *Front. Life Sci.* **2015**, *8* (4), 332–347. <https://doi.org/10.1080/21553769.2015.1044129>.
- (14) Minoshima, S.; Giordani, B.; Berent, S.; Frey, K. A.; Foster, N. L.; Kuhl, D. E. Metabolic Reduction in the Posterior Cingulate Cortex in Very Early Alzheimer's Disease. *Ann. Neurol.* **1997**, *42* (1), 85–94. <https://doi.org/10.1002/ana.410420114>.
- (15) Mosconi, L.; Tsui, W. H.; Herholz, K.; Pupi, A.; Drzezga, A.; Lucignani, G.; Reiman, E. M.; Holthoff, V.; Kalbe, E.; Sorbi, S.; Diehl-Schmid, J.; Perneczky, R.; Clerici, F.; Caselli, R.; Beuthien-Baumann, B.; Kurz, A.; Minoshima, S.; de Leon, M. J. Multicenter Standardized

- 18F-FDG PET Diagnosis of Mild Cognitive Impairment, Alzheimer's Disease, and Other Dementias. *J. Nucl. Med. Off. Publ. Soc. Nucl. Med.* **2008**, *49* (3), 390–398. <https://doi.org/10.2967/jnumed.107.045385>.
- (16) Pearson, S. D.; Ollendorf, D. A.; Colby, J. A. Amyloid- $\beta$  Positron Emission Tomography in the Diagnostic Evaluation of Alzheimer Disease: Summary of Primary Findings and Conclusions. *JAMA Intern. Med.* **2014**, *174* (1), 133–134. <https://doi.org/10.1001/jamainternmed.2013.11711>.
- (17) Ferrando, R.; Damian, A. Brain SPECT as a Biomarker of Neurodegeneration in Dementia in the Era of Molecular Imaging: Still a Valid Option? *Front. Neurol.* **2021**, *12* (May), 1–16. <https://doi.org/10.3389/fneur.2021.629442>.
- (18) Telano, L. N.; Baker, S. Physiology, Cerebral Spinal Fluid. In *StatPearls*; StatPearls Publishing: Treasure Island (FL), 2024.
- (19) Hrishi, A. P.; Sethuraman, M. Cerebrospinal Fluid (CSF) Analysis and Interpretation in Neurocritical Care for Acute Neurological Conditions. *Indian J. Crit. Care Med. Peer-Rev. Off. Publ. Indian Soc. Crit. Care Med.* **2019**, *23* (Suppl 2), S115–S119. <https://doi.org/10.5005/jp-journals-10071-23187>.
- (20) Bouwman, F. H.; Frisoni, G. B.; Johnson, S. C.; Chen, X.; Engelborghs, S.; Ikeuchi, T.; Paquet, C.; Ritchie, C.; Bozeat, S.; Quevenco, F.; Teunissen, C. Clinical Application of CSF Biomarkers for Alzheimer's Disease: From Rationale to Ratios. *Alzheimers Dement. Diagn. Assess. Dis. Monit.* **2022**, *14* (1), e12314. <https://doi.org/10.1002/dad2.12314>.
- (21) Pais, M. V.; Forlenza, O. V.; Diniz, B. S. Plasma Biomarkers of Alzheimer's Disease: A Review of Available Assays, Recent Developments, and Implications for Clinical Practice. *J. Alzheimers Dis. Rep.* **2023**, *7* (1), 355–380. <https://doi.org/10.3233/ADR-230029>.

- (22) Slot, R. E. R.; Sikkes, S. A. M.; Berkhof, J.; Brodaty, H.; Buckley, R.; Cavedo, E.; Dardiotis, E.; Guillo-Benarous, F.; Hampel, H.; Kochan, N. A.; Lista, S.; Luck, T.; Maruff, P.; Molinuevo, J. L.; Kornhuber, J.; Reisberg, B.; Riedel-Heller, S. G.; Risacher, S. L.; Roehr, S.; Sachdev, P. S.; Scarmeas, N.; Scheltens, P.; Shulman, M. B.; Saykin, A. J.; Verfaillie, S. C. J.; Visser, P. J.; Vos, S. J. B.; Wagner, M.; Wolfgruber, S.; Jessen, F.; the Alzheimer's Disease Neuroimaging Initiative; the DESCRIPA working group; the INSIGHT-preAD study group; SCD-I working group; Van Der Flier, W. M. Subjective Cognitive Decline and Rates of Incident Alzheimer's Disease and Non-Alzheimer's Disease Dementia. *Alzheimers Dement.* **2019**, *15* (3), 465–476. <https://doi.org/10.1016/j.jalz.2018.10.003>.
- (23) Altuna-Azkargorta, M.; Mendioroz-Iriarte, M. Blood Biomarkers in Alzheimer's Disease. *Neurol. Engl. Ed.* **2021**, *36* (9), 704–710. <https://doi.org/10.1016/j.nrleng.2018.03.006>.
- (24) Coyle, J. D. *Introduction to Organic Photochemistry*; Wiley, 1991.
- (25) Jun, Y. W.; Cho, S. W.; Jung, J.; Huh, Y.; Kim, Y.; Kim, D.; Ahn, K. H. Frontiers in Probing Alzheimer's Disease Biomarkers with Fluorescent Small Molecules. *ACS Cent. Sci.* **2019**, *5* (2), 209–217. <https://doi.org/10.1021/acscentsci.8b00951>.
- (26) Cui, M.; Ono, M.; Watanabe, H.; Kimura, H.; Liu, B.; Saji, H. Smart Near-Infrared Fluorescence Probes with Donor–Acceptor Structure for in Vivo Detection of  $\beta$ -Amyloid Deposits. *J. Am. Chem. Soc.* **2014**, *136* (9), 3388–3394. <https://doi.org/10.1021/ja4052922>.
- (27) Rejc, L.; Šmid, L.; Kepe, V.; Podlipnik, Č.; Golobič, A.; Bresjanac, M.; Barrio, J. R.; Petrič, A.; Košmrlj, J. Design, Syntheses, and in Vitro Evaluation of New Fluorine-18 Radiolabeled Tau-Labeling Molecular Probes. *J. Med. Chem.* **2017**, *60* (21), 8741–8757. <https://doi.org/10.1021/acs.jmedchem.7b00764>.

- (28) Liu, Y.; Zhuang, D.; Wang, J.; Huang, H.; Li, R.; Wu, C.; Deng, Y.; Hu, G.; Guo, B. Recent Advances in Small Molecular Near-Infrared Fluorescence Probes for a Targeted Diagnosis of the Alzheimer Disease. *Analyst* **2022**, *147* (21), 4701–4723. <https://doi.org/10.1039/D2AN01327D>.
- (29) Su, D.; Diao, W.; Li, J.; Pan, L.; Zhang, X.; Wu, X.; Mao, W. Strategic Design of Amyloid- $\beta$  Species Fluorescent Probes for Alzheimer's Disease. *ACS Chem. Neurosci.* **2022**, *13* (5), 540–551. <https://doi.org/10.1021/acscchemneuro.1c00810>.
- (30) Salzman, P. J. *Investigation of the Time Dependent Schrödinger-Newton Equation*; University of California, Davis, 2005.
- (31) Foresman, J. B.; Frisch, Ae. *Exploring Chemistry with Electronic Structure Methods*, Third edition.; Gaussian, Inc: Wallingford, CT, 2015.
- (32) Hartree, D. R. The Wave Mechanics of an Atom with a Non-Coulomb Central Field. Part I. Theory and Methods. *Math. Proc. Camb. Philos. Soc.* **1928**, *24* (1), 89–110. <https://doi.org/10.1017/S0305004100011919>.
- (33) Levine, I. N. *Química cuántica*; Pearson Educación, 2001.
- (34) Jäger, M.; Freitag, L.; González, L. Using Computational Chemistry to Design Ru Photosensitizers with Directional Charge Transfer. *Coord. Chem. Rev.* **2015**, *304–305*, 146–165. <https://doi.org/10.1016/j.ccr.2015.03.019>.
- (35) Hartree, D. R. The Wave Mechanics of an Atom with a Non-Coulomb Central Field. Part III. Term Values and Intensities in Series in Optical Spectra. *Math. Proc. Camb. Philos. Soc.* **1928**, *24* (3), 426–437. <https://doi.org/10.1017/S0305004100015954>.
- (36) Jensen, F. *Introduction to Computational Chemistry*; John Wiley & Sons, 2017.

- (37) Rindt, C. C. M.; Gaastra-Nedea, S. V. 15 - Modeling Thermochemical Reactions in Thermal Energy Storage Systems. In *Advances in Thermal Energy Storage Systems*; Cabeza, L. F., Ed.; Woodhead Publishing Series in Energy; Woodhead Publishing, 2015; pp 375–415. <https://doi.org/10.1533/9781782420965.3.375>.
- (38) Zhang, R.; Zhao, C.; Huo, Y.; Han, Y.; Hong, J.; Liu, Y.; Zhang, A.; Guo, R.; Ai, Y. Chapter 7 - Theoretical Calculation of Toxic/Radioactive Metal Ion Capture by Novel Nanomaterials. In *Emerging Nanomaterials for Recovery of Toxic and Radioactive Metal Ions from Environmental Media*; Wang, X., Ed.; Elsevier, 2022; pp 313–379. <https://doi.org/10.1016/B978-0-323-85484-9.00004-2>.
- (39) Hasnip, P. J.; Refson, K.; Probert, M. I. J.; Yates, J. R.; Clark, S. J.; Pickard, C. J. Density Functional Theory in the Solid State. *Philos. Transact. A Math. Phys. Eng. Sci.* **2014**, 372 (2011), 20130270. <https://doi.org/10.1098/rsta.2013.0270>.
- (40) Koch, W.; Holthausen, M. C. *A Chemist's Guide to Density Functional Theory*; Wiley, 2001. <https://doi.org/10.1002/3527600043>.
- (41) Morgan, B. J.; Madden, P. A. Lithium Intercalation into TiO<sub>2</sub>(B): A Comparison of LDA, GGA, and GGA+U Density Functional Calculations. *Phys. Rev. B* **2012**, 86 (3), 035147. <https://doi.org/10.1103/PhysRevB.86.035147>.
- (42) Lininger, C. N.; Gauthier, J. A.; Li, W.-L.; Rossomme, E.; Welborn, V. V.; Lin, Z.; Head-Gordon, T.; Head-Gordon, M.; Bell, A. T. Challenges for Density Functional Theory: Calculation of CO Adsorption on Electrocatalytically Relevant Metals. *Phys. Chem. Chem. Phys.* **2021**, 23 (15), 9394–9406. <https://doi.org/10.1039/D0CP03821K>.

- (43) Staroverov, V. N.; Scuseria, G. E.; Tao, J.; Perdew, J. P. Comparative Assessment of a New Nonempirical Density Functional: Molecules and Hydrogen-Bonded Complexes. *J. Chem. Phys.* **2003**, *119* (23), 12129–12137. <https://doi.org/10.1063/1.1626543>.
- (44) Kepp, K. P. Consistent Descriptions of Metal–Ligand Bonds and Spin-Crossover in Inorganic Chemistry. *Coord. Chem. Rev.* **2013**, *257* (1), 196–209. <https://doi.org/10.1016/j.ccr.2012.04.020>.
- (45) Rayne, S.; Forest, K. Performance of the Major Semiempirical, Ab Initio, and DFT Methods for Isomerization Enthalpies of Linear to Branched Heptanes. *J. Environ. Sci. Health Part A* **2016**, *51* (7), 583–587. <https://doi.org/10.1080/10934529.2016.1141626>.
- (46) Sandoval-Pauker, C.; Yin, S.; Castillo, A.; Ocuane, N.; Puerto-Diaz, D.; Villagrán, D. Computational Chemistry as Applied in Environmental Research: Opportunities and Challenges. *ACS EST Eng.* **2024**, *4* (1), 66–95. <https://doi.org/10.1021/acsestengg.3c00227>.
- (47) Boys, S. F.; Egerton, A. C. Electronic Wave Functions - I. A General Method of Calculation for the Stationary States of Any Molecular System. *Proc. R. Soc. Lond. Ser. Math. Phys. Sci.* **1997**, *200* (1063), 542–554. <https://doi.org/10.1098/rspa.1950.0036>.
- (48) Adamo, C.; Jacquemin, D. The Calculations of Excited-State Properties with Time-Dependent Density Functional Theory. *Chem Soc Rev* **2013**, *42* (3), 845–856. <https://doi.org/10.1039/C2CS35394F>.
- (49) Dreuw, A.; Head-Gordon, M. Single-Reference Ab Initio Methods for the Calculation of Excited States of Large Molecules. *Chem. Rev.* **2005**, *105* (11), 4009–4037. <https://doi.org/10.1021/cr0505627>.
- (50) Savasta, S.; Stefano, O. D.; Nori, F. Thomas–Reiche–Kuhn (TRK) Sum Rule for Interacting Photons. *Nanophotonics* **2021**, *10* (1), 465–476. <https://doi.org/10.1515/nanoph-2020-0433>.

- (51) Müller, C.; Sharma, M.; Sierka, M. Real-Time Time-Dependent Density Functional Theory Using Density Fitting and the Continuous Fast Multipole Method. *J. Comput. Chem.* **2020**, *41* (30), 2573–2582. <https://doi.org/10.1002/jcc.26412>.
- (52) Frisch, M. J.; Trucks, G. W.; Schlegel, H. B.; Scuseria, G. E.; Robb, M. A.; Cheeseman, J. R.; Scalmani, G.; Barone, V.; Petersson, G. A.; Nakatsuji, H.; Li, X.; Caricato, M.; Marenich, A. V.; Bloino, J.; Janesko, B. G.; Gomperts, R.; Mennucci, B.; Hratchian, H. P.; Ortiz, J. V.; Izmaylov, A. F.; Sonnenberg, J. L.; Williams-Young, D.; Ding, F.; Lipparini, F.; Egidi, F.; Goings, J.; Peng, B.; Petrone, A.; Henderson, T.; Ranasinghe, D.; Zakrzewski, V. G.; Gao, J.; Rega, N.; Zheng, G.; Liang, W.; Hada, M.; Ehara, M.; Toyota, K.; Fukuda, R.; Hasegawa, J.; Ishida, M.; Nakajima, T.; Honda, Y.; Kitao, O.; Nakai, H.; Vreven, T.; Throssell, K.; Montgomery Jr., J. A.; Peralta, J. E.; Ogliaro, F.; Bearpark, M. J.; Heyd, J. J.; Brothers, E. N.; Kudin, K. N.; Staroverov, V. N.; Keith, T. A.; Kobayashi, R.; Normand, J.; Raghavachari, K.; Rendell, A. P.; Burant, J. C.; Iyengar, S. S.; Tomasi, J.; Cossi, M.; Millam, J. M.; Klene, M.; Adamo, C.; Cammi, R.; Ochterski, J. W.; Martin, R. L.; Morokuma, K.; Farkas, O.; Foresman, J. B.; Fox, D. J. Gaussian 16, Revision B.01, 2016.
- (53) Lee, C.; Yang, W.; Parr, R. G. Development of the Colle-Salvetti Correlation-Energy Formula into a Functional of the Electron Density. *Phys. Rev. B* **1988**, *37* (2), 785–789. <https://doi.org/10.1103/PhysRevB.37.785>.
- (54) Becke, A. D. Density-functional Thermochemistry. III. The Role of Exact Exchange. *J. Chem. Phys.* **1993**, *98* (7), 5648–5652. <https://doi.org/10.1063/1.464913>.
- (55) Stephens, P. J.; Devlin, F. J.; Chabalowski, C. F.; Frisch, M. J. Ab Initio Calculation of Vibrational Absorption and Circular Dichroism Spectra Using Density Functional Force Fields. *J. Phys. Chem.* **1994**, *98* (45), 11623–11627. <https://doi.org/10.1021/j100096a001>.

- (56) Kendall, R. A.; Dunning, T. H.; Harrison, R. J. Electron Affinities of the First-Row Atoms Revisited. Systematic Basis Sets and Wave Functions. *J Chem Phys* **1992**, *96* (9), 6796–6806. <https://doi.org/10.1063/1.462569>.
- (57) Lu, T.; Chen, F. Multiwfn: A Multifunctional Wavefunction Analyzer. *J Comp Chem* **2012**, *33* (5), 580–592. <https://doi.org/10.1002/jcc.22885>.
- (58) Humphrey, W.; Dalke, A.; Schulten, K. VMD: Visual Molecular Dynamics. *J. Mol. Graph.* **1996**, *14* (1), 33–38. [https://doi.org/10.1016/0263-7855\(96\)00018-5](https://doi.org/10.1016/0263-7855(96)00018-5).
- (59) Zhao, Y.; Truhlar, D. G. The M06 Suite of Density Functionals for Main Group Thermochemistry, Thermochemical Kinetics, Noncovalent Interactions, Excited States, and Transition Elements: Two New Functionals and Systematic Testing of Four M06-Class Functionals and 12 Other Functionals. *Theor. Chem. Acc.* **2008**, *120* (1–3), 215–241. <https://doi.org/10.1007/s00214-007-0310-x>.
- (60) Marenich, A. V.; Cramer, C. J.; Truhlar, D. G. Universal Solvation Model Based on Solute Electron Density and on a Continuum Model of the Solvent Defined by the Bulk Dielectric Constant and Atomic Surface Tensions. *J. Phys. Chem. B* **2009**, *113* (18), 6378–6396. <https://doi.org/10.1021/jp810292n>.
- (61) Lu, L.; Wu, Z.; Li, X.; Han, F. State-of-the-Art: Functional Fluorescent Probes for Bioimaging and Pharmacological Research. *Acta Pharmacol. Sin.* **2019**, *40* (6), 717–723. <https://doi.org/10.1038/s41401-018-0190-8>.
- (62) Hu, T.-M.; Chiu, S.-J.; Hsu, Y.-M. Nitroxidative Chemistry Interferes with Fluorescent Probe Chemistry: Implications for Nitric Oxide Detection Using 2,3-Diaminonaphthalene. *Biochem. Biophys. Res. Commun.* **2014**, *451* (2), 196–201. <https://doi.org/10.1016/j.bbrc.2014.07.097>.



- (63) Ferreira, R. B.; Fu, L.; Jung, Y.; Yang, J.; Carroll, K. S. Reaction-Based Fluorogenic Probes for Detecting Protein Cysteine Oxidation in Living Cells. *Nat. Commun.* **2022**, *13* (1), 5522. <https://doi.org/10.1038/s41467-022-33124-z>.
- (64) Jiang, G.; Ren, T.-B.; D'Este, E.; Xiong, M.; Xiong, B.; Johnsson, K.; Zhang, X.-B.; Wang, L.; Yuan, L. A Synergistic Strategy to Develop Photostable and Bright Dyes with Long Stokes Shift for Nanoscopy. *Nat. Commun.* **2022**, *13* (1), 2264. <https://doi.org/10.1038/s41467-022-29547-3>.
- (65) Zimmer, M. Green Fluorescent Protein (GFP): Applications, Structure, and Related Photophysical Behavior. *Chem. Rev.* **2002**, *102* (3), 759–782. <https://doi.org/10.1021/cr010142r>.
- (66) Yang, F.; Moss, L. G.; Phillips, G. N. The Molecular Structure of Green Fluorescent Protein. **1996**, *14*.
- (67) Flaiz, M.; Baur, T.; Gaibler, J.; Kröly, C.; Dürre, P. Establishment of Green- and Red-Fluorescent Reporter Proteins Based on the Fluorescence-Activating and Absorption-Shifting Tag for Use in Acetogenic and Solventogenic Anaerobes. *ACS Synth. Biol.* **2022**, *11* (2), 953–967. <https://doi.org/10.1021/acssynbio.1c00554>.
- (68) Pak, Y.; Swamy, K.; Yoon, J. Recent Progress in Fluorescent Imaging Probes. *Sensors* **2015**, *15* (9), 24374–24396. <https://doi.org/10.3390/s150924374>.
- (69) Guo, Z.; Cui, Z. Fluorescent Nanotechnology for in Vivo Imaging. *WIREs Nanomedicine Nanobiotechnology* **2021**, *13* (5), e1705. <https://doi.org/10.1002/wnan.1705>.
- (70) Li, S.; Huo, F.; Yin, C. Progress in the Past Five Years of Small Organic Molecule Dyes for Tumor Microenvironment Imaging. *Chem. Commun.* **2022**, *58* (91), 12642–12652. <https://doi.org/10.1039/D2CC04975A>.

- (71) Fu, Y.; Finney, N. S. Small-Molecule Fluorescent Probes and Their Design. *RSC Adv.* **2018**, 8 (51), 29051–29061. <https://doi.org/10.1039/C8RA02297F>.
- (72) Lee, H.; In, B.; Mehta, P. K.; Kishore, M. Y. L. N.; Lee, K.-H. Dual Role of a Fluorescent Peptidyl Probe Based on Self-Assembly for the Detection of Heparin and for the Inhibition of the Heparin-Digestive Enzyme Reaction. *ACS Appl. Mater. Interfaces* **2018**, 10 (3), 2282–2290. <https://doi.org/10.1021/acsami.7b15411>.
- (73) Zhao, Y.; Jiang, Y.; Wang, Q.; Sun, Y.; Huang, K.; Yao, Z. Rapid and Sensitive Detection of Dextran Sulfate Sodium Based on Supramolecular Self-Assembly of a Perylene Diimide Derivative in Aqueous Solution. *Spectrochim. Acta. A. Mol. Biomol. Spectrosc.* **2022**, 270, 120760. <https://doi.org/10.1016/j.saa.2021.120760>.
- (74) Law, A. S.-Y.; Lee, L. C.-C.; Yeung, M. C.-L.; Lo, K. K.-W.; Yam, V. W.-W. Amyloid Protein-Induced Supramolecular Self-Assembly of Water-Soluble Platinum(II) Complexes: A Luminescence Assay for Amyloid Fibrillation Detection and Inhibitor Screening. *J. Am. Chem. Soc.* **2019**, 141 (46), 18570–18577. <https://doi.org/10.1021/jacs.9b09515>.
- (75) Gade Malmos, K.; Blancas-Mejia, L. M.; Weber, B.; Buchner, J.; Ramirez-Alvarado, M.; Naiki, H.; Otzen, D. ThT 101: A Primer on the Use of Thioflavin T to Investigate Amyloid Formation. *Amyloid* **2017**, 24 (1), 1–16. <https://doi.org/10.1080/13506129.2017.1304905>.
- (76) Sulatskaya, A. I.; Lavysh, A. V.; Maskevich, A. A.; Kuznetsova, I. M.; Turoverov, K. K. Thioflavin T Fluoresces as Excimer in Highly Concentrated Aqueous Solutions and as Monomer Being Incorporated in Amyloid Fibrils. *Sci. Rep.* **2017**, 7 (1), 2146. <https://doi.org/10.1038/s41598-017-02237-7>.

- (77) Xue, C.; Lin, T. Y.; Chang, D.; Guo, Z. Thioflavin T as an Amyloid Dye: Fibril Quantification, Optimal Concentration and Effect on Aggregation. *R. Soc. Open Sci.* **2017**, *4* (1), 160696. <https://doi.org/10.1098/rsos.160696>.
- (78) Sabaté, R.; Saupe, S. J. Thioflavin T Fluorescence Anisotropy: An Alternative Technique for the Study of Amyloid Aggregation. *Biochem. Biophys. Res. Commun.* **2007**, *360* (1), 135–138. <https://doi.org/10.1016/j.bbrc.2007.06.063>.
- (79) Biancalana, M.; Koide, S. Molecular Mechanism of Thioflavin-T Binding to Amyloid Fibrils. *Biochim. Biophys. Acta BBA - Proteins Proteomics* **2010**, *1804* (7), 1405–1412. <https://doi.org/10.1016/j.bbapap.2010.04.001>.
- (80) Amdursky, N.; Erez, Y.; Huppert, D. Molecular Rotors: What Lies Behind the High Sensitivity of the Thioflavin-T Fluorescent Marker. *Acc. Chem. Res.* **2012**, *45* (9), 1548–1557. <https://doi.org/10.1021/ar300053p>.
- (81) Voropai, E. S.; Samtsov, M. P.; Kaplevskii, K. N.; Maskevich, A. A.; Stepuro, V. I.; Povarova, O. I.; Kuznetsova, I. M.; Turoverov, K. K.; Fink, A. L.; Uverskii, V. N. Spectral Properties of Thioflavin T and Its Complexes with Amyloid Fibrils. *J. Appl. Spectrosc.* **2003**, *70* (6), 868–874. <https://doi.org/10.1023/B:JAPS.0000016303.37573.7e>.
- (82) Xu, M.; Ren, W.; Tang, X.; Hu, Y.; Zhang, H. Advances in Development of Fluorescent Probes for Detecting Amyloid- $\beta$  Aggregates. *Acta Pharmacol. Sin.* **2016**, *37* (6), 719–730. <https://doi.org/10.1038/aps.2015.155>.
- (83) Freire, S.; De Araujo, M. H.; Al-Soufi, W.; Novo, M. Photophysical Study of Thioflavin T as Fluorescence Marker of Amyloid Fibrils. *Dyes Pigments* **2014**, *110*, 97–105. <https://doi.org/10.1016/j.dyepig.2014.05.004>.

- (84) Agdeppa, E. D.; Kepe, V.; Liu, J.; Flores-Torres, S.; Satyamurthy, N.; Petric, A.; Cole, G. M.; Small, G. W.; Huang, S.-C.; Barrio, J. R. Binding Characteristics of Radiofluorinated 6-Dialkylamino-2-Naphthylethylidene Derivatives as Positron Emission Tomography Imaging Probes for  $\beta$ -Amyloid Plaques in Alzheimer's Disease. *J. Neurosci.* **2001**, *21* (24), RC189–RC189. <https://doi.org/10.1523/JNEUROSCI.21-24-j0004.2001>.
- (85) Jacobson, A.; Petric, A.; Hogenkamp, D.; Sinur, A.; Barrio, J. R. 1,1-Dicyano-2-[6-(Dimethylamino)Naphthalen-2-Yl]Propene (DDNP): A Solvent Polarity and Viscosity Sensitive Fluorophore for Fluorescence Microscopy. *J. Am. Chem. Soc.* **1996**, *118* (24), 5572–5579. <https://doi.org/10.1021/ja9543356>.
- (86) Shin, J.; Kepe, V.; Barrio, J. R.; Small, G. W. The Merits of FDDNP-PET Imaging in Alzheimer's Disease. *J. Alzheimers Dis.* **2011**, *26* (s3), 135–145. <https://doi.org/10.3233/JAD-2011-0008>.
- (87) Šarlah, D.; Juranovič, A.; Kožar, B.; Rejc, L.; Golobič, A.; Petrič, A. Synthesis of Naphthalene-Based Push-Pull Molecules with a Heteroaromatic Electron Acceptor. *Molecules* **2016**, *21* (3), 267. <https://doi.org/10.3390/molecules21030267>.
- (88) Rejc, L.; Fabris, J.; Adrovič, A.; Kasunič, M.; Petrič, A. Elongation of the Molecular Probe DDNP with Phenylethynylidene or Phenyldiazenylidene Spacers. *Tetrahedron Lett.* **2014**, *55* (6), 1218–1221. <https://doi.org/10.1016/j.tetlet.2014.01.002>.
- (89) Petrič, A.; Johnson, S. A.; Pham, H. V.; Li, Y.; Čeh, S.; Golobič, A.; Agdeppa, E. D.; Timbol, G.; Liu, J.; Keum, G.; Satyamurthy, N.; Kepe, V.; Houk, K. N.; Barrio, J. R. Dicyanovinyl naphthalenes for Neuroimaging of Amyloids and Relationships of Electronic Structures and Geometries to Binding Affinities. *Proc. Natl. Acad. Sci.* **2012**, *109* (41), 16492–16497. <https://doi.org/10.1073/pnas.1214134109>.

- (90) Correction for Petrič et al., Dicyanovinyl naphthalenes for Neuroimaging of Amyloids and Relationships of Electronic Structures and Geometries to Binding Affinities. *Proc. Natl. Acad. Sci.* **2013**, *110* (13), 5269–5269. <https://doi.org/10.1073/pnas.1302644110>.
- (91) Dennington, R.; Todd, K.; John, M. GaussView V. 6.1.1, 2019. <https://gaussian.com/gv611rn/>.
- (92) Alkorta, I.; Elguero, J. Dissociation Energies and Rotational Barriers About CC Single, Double, and Triple Bonds: A Hybrid HF-DFT Approach (Becke3LYP/6-311++G\*\*).
- (93) Grabowski, Z. R.; Dobkowski, J. Twisted Intramolecular Charge Transfer (TICT) Excited States: Energy and Molecular Structure. **1983**, *55*, 245–252. <https://doi.org/10.1351/pac198855020245>.
- (94) Kochman, M. A.; Durbeej, B. Simulating the Nonadiabatic Relaxation Dynamics of 4-(N,N-Dimethylamino)Benzonitrile (DMABN) in Polar Solution. *J. Phys. Chem. A* **2020**, *124* (11), 2193–2206. <https://doi.org/10.1021/acs.jpca.9b10588>.
- (95) Mester, D.; Mihaly, K. A Simple Range-Separated Double-Hybrid Density Functional Theory for Excited States. *J. Chem. Theory Comput.* **2021**, *17* (2), 927–942. <https://doi.org/10.1021/acs.jctc.0c01135>.
- (96) NIH National Institute on Aging (NIA). *What Causes Alzheimer's Disease?* <https://www.nia.nih.gov/health/what-causes-alzheimers-disease>.
- (97) Agatonovic-Kustrin, S.; Kettle, C.; Morton, D. W. A Molecular Approach in Drug Development for Alzheimer's Disease. *Biomed. Pharmacother.* **2018**, *106* (May), 553–565. <https://doi.org/10.1016/j.biopha.2018.06.147>.
- (98) Lee, V. M.-Y.; Goedert, M.; Trojanowski, J. Q. Neurodegenerative Tauopathies. *Annu. Rev. Neurosci.* **2001**, *24* (1), 1121–1159. <https://doi.org/10.1146/annurev.neuro.24.1.1121>.

- (99) Sinha, S. The Role of Beta-Amyloid in Alzheimer's Disease. *Med. Clin. North Am.* **2002**, *86* (3), 629–639. [https://doi.org/10.1016/S0025-7125\(02\)00022-6](https://doi.org/10.1016/S0025-7125(02)00022-6).
- (100) Sperling, R. A.; Aisen, P. S.; Beckett, L. A.; Bennett, D. A.; Craft, S.; Fagan, A. M.; Iwatsubo, T.; Jack, C. R.; Kaye, J.; Montine, T. J.; Park, D. C.; Reiman, E. M.; Rowe, C. C.; Siemers, E.; Stern, Y.; Yaffe, K.; Carrillo, M. C.; Thies, B.; Morrison-Bogorad, M.; Wagster, M. V.; Phelps, C. H. Toward Defining the Preclinical Stages of Alzheimer's Disease: Recommendations from the National Institute on Aging-Alzheimer's Association Workgroups on Diagnostic Guidelines for Alzheimer's Disease. *Alzheimers Dement.* **2011**, *7* (3), 280–292. <https://doi.org/10.1016/j.jalz.2011.03.003>.
- (101) Blennow, K.; Hampel, H.; Weiner, M.; Zetterberg, H. Cerebrospinal Fluid and Plasma Biomarkers in Alzheimer Disease. *Nat. Publ. Group* **2010**, *6* (marCH), 131–144. <https://doi.org/10.1038/nrneurol.2010.4>.
- (102) Hampel, H.; O'Bryant, S. E.; Molinuevo, J. L.; Zetterberg, H.; Masters, C. L.; Lista, S.; Kiddle, S. J.; Batrla, R.; Blennow, K. Blood-Based Biomarkers for Alzheimer Disease: Mapping the Road to the Clinic. *Nat. Rev. Neurol.* **2018**, *14* (11), 639–652. <https://doi.org/10.1038/s41582-018-0079-7>.
- (103) Henriksen, K.; O'Bryant, S. E.; Hampel, H.; Trojanowski, J. Q.; Montine, T. J.; Jeromin, A.; Blennow, K.; Lönneborg, A.; Wyss-Coray, T.; Soares, H.; Bazenet, C.; Sjögren, M.; Hu, W.; Lovestone, S.; Karsdal, M. A.; Weiner, M. W. The Future of Blood-based Biomarkers for Alzheimer's Disease. *Alzheimers Dement.* **2014**, *10* (1), 115–131. <https://doi.org/10.1016/j.jalz.2013.01.013>.
- (104) Liu, W.; Lin, H.; He, X.; Chen, L.; Dai, Y.; Jia, W.; Xue, X.; Tao, J.; Chen, L. Neurogranin as a Cognitive Biomarker in Cerebrospinal Fluid and Blood Exosomes for Alzheimer's

- Disease and Mild Cognitive Impairment. *Transl. Psychiatry* **2020**, *10* (1), 125.  
<https://doi.org/10.1038/s41398-020-0801-2>.
- (105) Mattsson, N.; Cullen, N. C.; Andreasson, U.; Zetterberg, H.; Blennow, K. Association Between Longitudinal Plasma Neurofilament Light and Neurodegeneration in Patients With Alzheimer Disease. *JAMA Neurol.* **2019**, *76* (7), 791.  
<https://doi.org/10.1001/jamaneurol.2019.0765>.
- (106) Nabers, A.; Hafermann, H.; Wiltfang, J.; Gerwert, K. A $\beta$  and Tau Structure-based Biomarkers for a Blood- and CSF-based Two-step Recruitment Strategy to Identify Patients with Dementia Due to Alzheimer's Disease. *Alzheimers Dement. Diagn. Assess. Dis. Monit.* **2019**, *11* (1), 257–263. <https://doi.org/10.1016/j.dadm.2019.01.008>.
- (107) Hwang, S. S.; Chan, H.; Sorci, M.; Van Deventer, J.; Wittrup, D.; Belfort, G.; Walt, D. Detection of Amyloid  $\beta$  Oligomers toward Early Diagnosis of Alzheimer's Disease. *Anal. Biochem.* **2019**, *566*, 40–45. <https://doi.org/10.1016/j.ab.2018.09.011>.
- (108) Rissin, D. M.; Kan, C. W.; Campbell, T. G.; Howes, S. C.; Fournier, D. R.; Song, L.; Piech, T.; Patel, P. P.; Chang, L.; Rivnak, A. J.; Ferrell, E. P.; Randall, J. D.; Provuncher, G. K.; Walt, D. R.; Duffy, D. C. Single-Molecule Enzyme-Linked Immunosorbent Assay Detects Serum Proteins at Subfemtomolar Concentrations. *Nat. Biotechnol.* **2010**, *28* (6), 595–599.  
<https://doi.org/10.1038/nbt.1641>.
- (109) RDKit: Open-Source Cheminformatics Software. <https://www.rdkit.org> (accessed 2024-01-15).
- (110) Weininger, D. SMILES, a Chemical Language and Information System. 1. Introduction to Methodology and Encoding Rules. *J. Chem. Inf. Comput. Sci.* **1988**, *28* (1), 31–36.  
<https://doi.org/10.1021/ci00057a005>.

- (111) Hanwell, M. D.; Curtis, D. E.; Lonie, D. C.; Vandermeersch, T.; Zurek, E.; Hutchison, G. R. Avogadro: An Advanced Semantic Chemical Editor, Visualization, and Analysis Platform. *J. Cheminformatics* **2012**, *4* (1), 17. <https://doi.org/10.1186/1758-2946-4-17>.
- (112) Zagidullin, B.; Wang, Z.; Guan, Y.; Pitkänen, E.; Tang, J. Comparative Analysis of Molecular Fingerprints in Prediction of Drug Combination Effects. *Brief. Bioinform.* **2021**, *22* (6), bbab291. <https://doi.org/10.1093/bib/bbab291>.
- (113) Pedregosa, F.; Varoquaux, G.; Gramfort, A.; Michel, V.; Thirion, B.; Grisel, O.; Blondel, M.; Prettenhofer, P.; Weiss, R.; Dubourg, V.; Vanderplas, J.; Passos, A.; Cournapeau, D.; Brucher, M.; Perrot, M.; Duchesnay, E. Scikit-Learn: Machine Learning in Python. *J. Mach. Learn. Res.* **2011**, *12*, 2825–2830.
- (114) Hashemi, A.; Peljo, P.; Laasonen, K. Understanding Electron Transfer Reactions Using Constrained Density Functional Theory: Complications Due to Surface Interactions. *J. Phys. Chem. C* **2023**, *127* (7), 3398–3407. <https://doi.org/10.1021/acs.jpcc.2c06537>.
- (115) Ono, M.; Hayashi, S.; Kimura, H.; Kawashima, H.; Nakayama, M.; Saji, H. Push–Pull Benzothiazole Derivatives as Probes for Detecting  $\beta$ -Amyloid Plaques in Alzheimer’s Brains. *Bioorg. Med. Chem.* **2009**, *17* (19), 7002–7007. <https://doi.org/10.1016/j.bmc.2009.08.032>.
- (116) Hong, M. C.; Kim, Y. K.; Choi, J. Y.; Yang, S. Q.; Rhee, H.; Ryu, Y. H.; Choi, T. H.; Cheon, G. J.; An, G. I.; Kim, H. Y. Synthesis and Evaluation of Stilbene Derivatives as a Potential Imaging Agent of Amyloid Plaques. *Bioorg. Med. Chem.* **2010**, *18* (22), 7724–7730. <https://doi.org/10.1016/j.bmc.2010.06.044>.
- (117) Brancato, G.; Signore, G.; Neyroz, P.; Polli, D.; Cerullo, G.; Abbandonato, G.; Nucara, L.; Barone, V.; Beltram, F.; Bizzarri, R. Dual Fluorescence through Kasha’s Rule Breaking: An



- Unconventional Photomechanism for Intracellular Probe Design. *J. Phys. Chem. B* **2015**, *119* (20), 6144–6154. <https://doi.org/10.1021/acs.jpcb.5b01119>.
- (118) Sasaki, S.; Drummen, G. P. C.; Konishi, G. Recent Advances in Twisted Intramolecular Charge Transfer (TICT) Fluorescence and Related Phenomena in Materials Chemistry. *J. Mater. Chem. C* **2016**, *4* (14), 2731–2743. <https://doi.org/10.1039/C5TC03933A>.
- (119) Grabowski, Z. R.; Rotkiewicz, K.; Rettig, W. Structural Changes Accompanying Intramolecular Electron Transfer: Focus on Twisted Intramolecular Charge-Transfer States and Structures. *Chem. Rev.* **2003**, *103* (10), 3899–4032. <https://doi.org/10.1021/cr940745l>.
- (120) Essam, Z. M.; Ozmen, G. E.; Setiawan, D.; Hamid, R. R.; Abd El-Aal, R. M.; Aneja, R.; Hamelberg, D.; Henary, M. Donor Acceptor Fluorophores: Synthesis, Optical Properties, TD-DFT and Cytotoxicity Studies. *Org. Biomol. Chem.* **2021**, *19* (8), 1835–1846. <https://doi.org/10.1039/D0OB02313B>.
- (121) Dunn, B.; Hanafi, M.; Hummel, J.; Cressman, J.; Veneziano, R.; Chitnis, P. NIR-II Nanoprobes: A Review of Components-Based Approaches to Next-Generation Bioimaging Probes. *Bioengineering* **2023**, *10* (8), 954. <https://doi.org/10.3390/bioengineering10080954>.
- (122) Li, Y.; Liu, J.; Liu, D.; Li, X.; Xu, Y. D-A- $\pi$ -A Based Organic Dyes for Efficient DSSCs: A Theoretical Study on the Role of  $\pi$ -Spacer. *Comput. Mater. Sci.* **2019**, *161*, 163–176. <https://doi.org/10.1016/j.commatsci.2019.01.033>.
- (123) Hussain Tahir, M.; Mubashir, T.; Tanveer-Ul-Hassan, S.; Mahmood, A. Impact of Electron-withdrawing and Electron-donating Substituents on the Electrochemical and Charge Transport Properties of Indacenodithiophene-based Small Molecule Acceptors for Organic Solar Cells. *J. Phys. Org. Chem.* **2019**, *32* (3), 44–49. <https://doi.org/10.1002/poc.3909>.

- (124) Ju, C.-W.; Bai, H.; Li, B.; Liu, R. Machine Learning Enables Highly Accurate Predictions of Photophysical Properties of Organic Fluorescent Materials: Emission Wavelengths and Quantum Yields. *J. Chem. Inf. Model.* **2021**, *61* (3), 1053–1065. <https://doi.org/10.1021/acs.jcim.0c01203>.

## Vita

Gabriela Elizabeth Molina Aguirre (<https://www.linkedin.com/in/gabrielaemolina/>) completed her undergraduate studies at Escuela Politécnica Nacional, in Quito - Ecuador, in April 2016. After that, she completed her Master's degree in Integrated Management Systems: Environment, Quality, and Control in April 2017 at Universidad Internacional de la Rioja in Quito - Ecuador. In 2016, Gabriela joined the oil and gas industry as a Technical and Commercial Coordinator at the China Petroleum Technology and Development Corporation branch in Ecuador where she received a prestigious work excellence award from the headquarters in China, recognizing her contributions. In 2020, she started her journey as a Ph.D. student in Chile in the Chemistry Program under the supervision of Dr. Balazs Pinter, and in 2021, she transferred her studies to the Department of Chemistry and Biochemistry at The University of Texas at El Paso. During her Ph.D. studies, she dedicated her research to different fields, including photoredox catalysis boron- aluminum- halides, with a primary focus on exploring molecular probes for Alzheimer's disease detection. Currently, her academic contributions cover 3 published papers: Status report on copper (I) complexes in photoredox catalysis photophysical and electrochemical properties and future prospects (<https://doi.org/10.1016/j.poly.2021.115105>). Resonance and electrostatics making the difference in boron- and aluminum-halide structures and exchange reactivity (<https://doi.org/10.1063/5.0094286>). Fusion Position-Dependent Aromatic Transitions of Ligand Backbone Rings for Controlling the Redox Energetics of Photoredox Catalysts (<https://doi.org/10.1021/acs.inorgchem.3c03831>). In February 2024, Gabriela got approval for her patent “development of a parallel plate reactor for the photocatalytic degradation of azo dyes using TiO<sub>2</sub> immobilized on polymeric plates” with the Ecuadorian Patent and Trademark Office as a result of her undergraduate work at Escuela Politécnica Nacional in Quito, Ecuador.